Alma Mater Studiorum - Università Di Bologna
Aalborg Universitet – Department of Civil Engineering

PhD in CIVIL and ENVIROMENTAL ENGINEERING

Cycle XXVI
Affiliation sector: 08/A1
Scientific sector: ICAR/01

Hydrodynamic induced by an array of wave energy converters. Experimental and numerical analysis

Elisa Angelelli

PhD Coordinator:
Alberto Lamberti
Full Professor
DICAM - University of Bologna
Viale Risorgimento, 40136 Bologna (IT)

Supervisor:
Barbara Zanuttigh
Assistant Professor, M. Sc., Ph. D.
DICAM - University of Bologna
Viale Risorgimento, 40136 Bologna (IT)

Co-supervisor:
Jens Peter Kofoed
Associate Professor, M. Sc., Ph. D.
Department of Civil Engineering
Sohngaardsholmsvej 57, DK-9000 Aalborg
Denmark

To be defended in public at the University of Bologna
19th May 2014

CONTENTS

1. NOMENCLATURE

l	device length
b	device width
PTO	Power Take-Off system
P_{PTO}	produced mechanical power
F	Force acting on the mooring lines
$F_{1/50}$	mean value of the 2% of the highest points of the force on the mooring line
L_C	length of the chain lying on the seabed
η	device efficiency
l/L_p	Ratio device-wave length
s_f	sample frequency
t	time
h	water depth
WS	wave state
P_W	incident wave power
WG	wave gauge
T_p	peak period
T_s	significant period
s_p	peak wave steepness
L_p	peak wave length
H_s	significant wave height (time domain)
H_{m0}	significant wave height (frequency domain)
BDM	Bayesian Directional Method
H_I	incident wave height
H_T	transmitted wave height
H_R	reflected wave height
K_T	transmission coefficient
K_{T1}	transmission coefficient for the front device in the staggered farm layout
K_{T2}	transmission coefficient for the first line in the staggered farm layout
K_{T3}	transmission coefficient for the back device in the staggered farm layout
K_{T4}	transmission coefficient for the farm in the staggered farm layout
K_R	reflection coefficient
K_{R1}	reflection coefficient for the front device in the staggered farm layout
K_{R2}	reflection coefficient for the back device in the staggered farm layout
K_D	dissipation coefficient
c_I	ratio between H_I at different scales
c_T	ratio between H_T at different scales
c_R	ratio between H_R at different scales
β	wave obliquity
θ_I	incident wave direction at the WG-castle
$\Delta\theta$	change of the main incident wave direction

2. ABSTRACT

Wave energy Converters (WECs) can be considered an innovative solution able to contribute to the green energy supply and –at the same time– to protect the rear coastal area under marine spatial planning considerations. This research activity essentially rises due to this combined concept.

The WEC under exam is a floating device belonging to the Wave Activated Bodies (WAB) class. The small dimension of this device does not limit the installation site, and since it is floating, it will be able to adapt to climate change situations, i.e. sea level rise. The device floating aspect also leads to avoid fixed foundation and geotechnical aspects due to soil bottom conditions, the arising parts are limited, therefore the environmental impact should be pretty low. Furthermore its power take-off system has the same principle of operation of the Pelamis (http://www.pelamiswave.com), which is the only WEC at a commercialization phase. Additionally the WAB devices are less investigated for example with respect of point absorbers. All these reasons explain the choice of the research on this device.

As reported in the title, this thesis has a double methodology. It mainly focuses on the hydrodynamics around a WAB device considered a single device or placed in a farms (e.g. a farm line and a staggered basic module), based on wave basin experiments carried out at Aalborg University and on numerical simulations performed with the codes MIKE 21 BW and ANSYS-AQWA. The final aim of this work is to provide guidelines relating to a wave farm installation of these WECs mainly in terms of hydrodynamic effects induced by them.
Experimental data were performed in 1:60 scale for the farm layouts and in 1:30 scale in case of single device, and the performance of the models was analysed under a variety of irregular wave attacks. A second experimental phase was necessary because some aspects (such as the mutual distance between the devices, long-shore wake effects, device motions, forces acting on the mooring lines with different mooring pre-tension levels and effects due to the presence of a more realist PTO in a farm configuration) were not completely investigated in the first physical tests. Experimental results were also used to calibrate the numerical parameters and/or to directly been compared to numerical results, in order to extend the experimental database.

Currently, in the literature, most of the studies deal with the efficiency of single WECs, however even for single WEC there is very limited research dedicated to verify to which extent the mooring layouts are affecting the hydrodynamic loading on the structure, as well as the power extraction capabilities (Vicente et. al., 2009). In addition, the contribution related to installations of wave farms is rather limited. Even if the primary focus of this thesis is the hydrodynamics around single or multiple devices, this research also includes aspect of power production (and Power Take-Off, PTO, optimisation) and mooring system.

The PTO system is a delicate feature which involves many different kinds of expertise, e.g. the converter itself (e.g. the turbine), the electrical generator, the automatic and remote control, the cabling and the energy transfer mechanism. Often the optimization of the PTO has a huge influence on power production (up to a factor 3), as demonstrated by Frigaard and Lykke Andersen (2009) for the Wave Star device.

The mooring system should be an active mooring, where its stiffness is important for the dynamic response (as for other WECs such as WaveBob, PowerBob http://www.westwave.ie) and may react to extreme conditions and/or sea level rise.

Specific objectives of this research activity are:

- to fully describe the hydrodynamic field around the devices, in terms of wave disturbance, wave reflection and wave transmission;
- to assess the effects of different water depths at installations;
- to examine the effects of wave obliquity and wave steepness;
- to investigate the power performance and scale effects;
- to estimate mooring effects and loads in terms of different typologies and pre-tension levels;
- to highlight the device key parameters and provide guidelines for a wave farm installation.

This contribution first introduces a summary of the State of the Art related to WECs. Since most of the studies carried out on them mainly following numerical approach, chapter 5 involves a short summary of the different available approach and/or software applied in coastal issues for WECs installations. Chapter 6, instead, deals with the floating device under exam, and then the thesis presents two parts dealing with the experimental and numerical activities respectively, with the relative set-up, results and preliminary conclusions.

In particular the experimental section (chapters 7 and 8) includes the laboratory facilities, i.e. the models, the mooring systems, the wave attacks (mainly representative of the ordinary and extreme climate of the Danish part of the North Sea) and the overall measurement equipments. Main outcomes are summarised, focusing on wave transmission and reflection, through the estimation of the wave heights in time and frequency domains. Changes of wave direction and wake effects are also investigated. Power production results, forces acting on mooring lines and overall device motions are also provided.

The numerical section (chapters 9 and 10) encloses the details of the numerical set-up for the two codes. Regarding MIKE 21 BW the calibration of the numerical parameters was based on experimental results, and mainly focused on the representation of the floating bodies by means of fixed porous layers. The most relevant results, such as incident wave energy, wave heights in the basin, wave reflection and transmission induced by the devices both in the numerical and experimental configuration, are then compared. Other two farm layouts (varying the device alignment and reducing the gap width keeping constant the staggered layout) were investigated with this code to find the best farm layout for coastal protection and energy production.

Finally in chapter 11 the main results of the overall activity are summarised. Last section of the thesis is instead dedicated to the list of publications in which the PhD student has been involved.

3. ITALIAN ABSTRACT

I convertitori di energia da onda sono comunemente conosciuti con il loro nome inglese "*Wave Energy Converters*" (WECs). I WECs possono essere considerati una soluzione innovativa in grado di generare energia pulita e, allo stesso tempo, di proteggere la zona costiera retrostante in un'ottica di ottimizzazione della pianificazione dello spazio marino occupato. Tale attività di ricerca nasce essenzialmente da questo concetto di scopi combinati.

Il WEC investigato è un dispositivo galleggiante appartenente alla classe delle zattere articolate, conosciute come *Wave Activated Bodies* (WAB). Le ridotte dimensioni di questo dispositivo permettono l'installazione in molteplici siti, e poiché è galleggiante, è prevedibile che sarà facilmente in grado di adattarsi a cambiamenti climatici, come ad esempio l'innalzamento del livello del mare. Il fatto che il dispositivo sia galleggiante evita dispendiosi studi geotecnici legati alle condizioni meccaniche e granulometriche del fondale, oltre ad evitare la realizzazione di costose opere di fondazione fissa, inoltre le parti emerse sono limitate, quindi l'impatto ambientale dovuto ad una installazione di tali WECs dovrebbe essere abbastanza basso. Inoltre il suo sistema di estrazione di energia ha lo stesso principio di funzionamento del Pelamis (http://www.pelamiswave.com) che, al momento, è l'unico WEC ad una fase di commercializzazione. Infine, i dispositivi di tipologia WAB sono tuttora poco studiati ad esempio rispetto ai dispositivi definiti *point absorber*. La scelta di effettuare un'approfondita ricerca sul dispositivo investigato è appunto principalmente legata a queste ragioni.

Come riportato nel titolo, questa tesi ha una doppia metodologia. La tesi si concentra principalmente sull'idrodinamica intorno a un dispositivo WAB installato come singolo dispositivo o collocato in un parco (ad esempio è stata analizzata una linea del parco e un modulo base a dispositivi sfalsati), sulla base di esperimenti in vasca effettuati presso l'Università di Aalborg e simulazioni numeriche effettuate con i codici MIKE 21 BW e ANSYS - AQWA. Lo scopo finale di questo lavoro è quello di fornire linee guida relative ad un'installazione di un parco di questi dispositivi, soprattutto in termini di effetti idrodinamici indotti dal parco stesso.

Le prove sperimentali sono state eseguite in scala 1:60 per il parco e in scala 1:30 per il singolo dispositivo, e tali configurazioni sono state sottoposte ad una ampia varietà di attacchi ondosi irregolari. Alcuni aspetti (come la distanza reciproca tra i dispositivi, effetti scia lungo riva, movimenti del dispositivo, forze che agiscono sui cavi di ancoraggio considerando anche differenti livelli di pretensione dell'ancoraggio e effetti dovuti alla presenza di un più realistico sistema di estrazione di energia nei dispositivi disposti in parco) non sono stati del tutto indagati nella prima tranche sperimentale, perciò è risultata indispensabile una seconda fase sperimentale. I risultati sperimentali sono stati utilizzati anche per calibrare i parametri numerici e/o sono stati direttamente comparati ai risultati numerici, al fine di ampliare il database sperimentale.

Attualmente, in letteratura, la maggior parte degli studi sui WECs è focalizzata sull'efficienza del singolo dispositivo, tuttavia anche per singolo WEC, poche ricerche includono la verifica di quanto la progettazione dell'ancoraggio influisca sul carico idrodinamico, nonché sulle capacità di estrazione di energia (Vicente et . al., 2009). Inoltre, anche contributi relativi ad installazioni di WECs in parchi sono piuttosto limitati. Anche se l'obiettivo primario di questa tesi è l'idrodinamica intorno ad uno o più dispositivi, questa ricerca comprende anche aspetti come il sistema di estrazione di energia (e sua ottimizzazione) e l'analisi degli effetti legati al sistema di ancoraggio scelto.

In particolare, il sistema di estrazione di energia coinvolge diversi campi di competenza, a partire dal convertitore stesso (ad esempio una turbina), al generatore elettrico, al controllo automatico e remoto, al cablaggio e al meccanismo di trasferimento di energia. Spesso l'ottimizzazione di tale sistema ha una grande influenza sulla produzione di energia (fino a un fattore 3), come dimostrato da Frigaard e Lykke Andersen (2009) per il dispositivo *WaveStar*.

Il sistema di ancoraggio dovrebbe essere un sistema attivo, dove la rigidità del sistema è parte integrante della dinamica del dispositivo stesso (come per altri WEC, quali ad esempio il Wavebob, PowerBob http://www.westwave.ie) e deve sostenere carichi legati a condizioni estreme e/o a variazioni del livello del mare.

Gli obiettivi specifici di questa attività di ricerca sono:

- descrivere completamente il campo idrodinamico attorno ai dispositivi, in termini di variazioni di superficie libera, riflessione e trasmissione dell'onda incidente;
- valutare gli effetti di diverse profondità di installazione del parco;
- esaminare gli effetti di obliquità e ripidità dell'onda;
- analizzare le prestazioni del dispositivo e gli effetti scala;
- stimare gli effetti dovuti alla scelta della tipologia di ancoraggio e i carichi agenti su diverse tipologie e/o sulla stessa tipologia al variare dei livelli di pretensionamento dei cavi;
- evidenziare i parametri chiave del dispositivo e fornire le linee guida per l'installazione in parco.

Questa tesi prima introduce una sintesi dello stato dell'arte relativamente ai convertitori di energia. Poiché la maggior parte degli studi disponibili in letteratura si basa su approcci numerici, il capitolo 5 include una breve sintesi della diverse teorie/software disponibili applicati in ambito costiero per le installazioni dei WECs. Nel capitolo 6, invece, viene descritto il dispositivo galleggiante in esame, successivamente la tesi presenta due parti relative rispettivamente alle attività sperimentali e a quelle numeriche, includendo il relativo set-up, i risultati e le conclusioni preliminari.

In particolare, la sezione sperimentale (capitoli 7 e 8) comprende la descrizione delle strutture di laboratorio, dei modelli, dei sistemi di ancoraggio, degli attacchi ondosi (prevalentemente rappresentativi del clima ordinario ed estremo della parte Danese del Mare del Nord) e degli strumenti di misura. I principali risultati sono riassunti, concentrandosi sulla trasmissione e riflessione delle onde incidenti, attraverso la stima delle altezze d'onda derivate sia nel dominio del tempo che della frequenza. Anche cambiamenti di direzione di propagazione delle onde e effetti scia sono stati indagati. Infine sono stati forniti anche risultati di produzione di energia, di forze agenti sulle linee di ancoraggio e movimenti globali del dispositivo.

La sezione numerica (capitoli 9 e 10) comprende la descrizione del set-up creato con i due software. Riguardo MIKE 21 BW, i parametri numerici sono stati calibrati sulla base dei risultati sperimentali. Particolare importanza è stata data alla rappresentazione dei corpi galleggianti mediante strati porosi fissi. I risultati numerici più rilevanti, come l'energia dell'onda incidente, l’altezza d’onde nel bacino, la riflessione e trasmissione d’onda indotta dai dispositivi, sono stati poi confrontati con i relativi dati sperimentali. Tramite MIKE 21 BW sono stati creati altri due layout del parco, variando l'allineamento dei dispositivi e/o riducendo la larghezza del varco tra dispositivi di una stessa linea con configurazione sfalsata. Tali layout aggiuntivi permettono di investigare quale configurazione sia più adatta al fine di combinare una buona produzione energetica e una sufficiente protezione della zona retrostante.

Infine nel capitolo 11, i principali risultati dell'intera attività di ricerca sono stati riassunti. L’ultima sezione della tesi contiene la lista delle pubblicazioni in cui la dottoranda è stata coinvolta.

4. INTRODUCTION

Coastal defence in a changing climate poses new challenges (Nicholls and de la Vega-Leinert, 2008). In fact, at present, erosion and flood are serious threats for coastal areas and actual defence technologies are often unsuited to cope with sea level rise and increased storminess. Defence solutions should be climate-proof and at the same time economically feasible while preserving the coastal ecosystem (Zanuttigh, 2011). Due to their adaptability to sea level changes and to the absence of piling-up, near-shore floating structures can be a smart defence solution. An innovative and sustainable way to combine coastal protection and energy production is the installation of farms of floating Wave Energy Converters. These solutions could become even more economical feasible if are design in terms of multi-purpose installation.

A Wave Energy Converter (WEC) is a device able to capture the energy within waves and transform it into electricity.

First concepts of WECs are dated back to 1973, with the oil crisis, but nowadays they are still at a development stadium (excepted for few that reached a prototype level) and first protocols where device developers can refer to and follow first appeared in the early 2000.

A summary of first concepts can be found in the proceedings of the Wave Energy Conference 1978 in London and of the Conference “Power from Sea Waves” in Edinburgh in 1979 (Count, 1980).

Since then, extensive research on wave energy has become increasingly evident. Several books (Brooke, 2003; Charlier & Justus, 1993; Cruz, 2008; McCormick, 2007; Ross, 1995; Shaw, 1982, etc.), conference/journal papers (Bahaj, 2011; Clément et al., 2002; Drew et al., 2009; Falcão, 2006, 2010; Heller, 2012; Nielsen et al., 2006, etc.) and reports (Csiro, 2012; Czech & Bauer, 2012; IEA, 2011; Nielsen, 2012; Previsic et al., 2004; Vennetti, 2012, etc.) have been published to outline the basic principles and progress of WECs development around the world.

As declared there is a really large number of different WEC concepts being investigated by companies and academic research groups around the world at present. Hence, there are also several classifications of them. The principals are three, i.e. according to the device location, to its position related with the incoming wave direction or to conversion principle.

The ‘historical’ classification (based on the device location) distinguishes among three classes: shore-line, near-shore or off-shore (see Fig. 4.1). Each group has positive and negative aspects, e.g. shore-line devices do not need strong mooring systems or long submerged electrical cables, and they have easy installation and maintenance; however, on the other hand, these devices can exploit a milder wave climate with respect to the off-shore available wave power.

A second classification is based on the WEC ability to intercept and attenuate waves, i.e. WECs could be: point absorbers, attenuators and terminators (see Fig. 4.2). A point absorber is a device whose size is small compared to the wave length. It is able to capture energy –regardless the incoming wave direction– from a wave front greater than its physical dimension. Elongated devices are named “terminators”, if they are placed parallel to the wave crest and normal to the energy flux, or “attenuators”, if they are effectively placed in the same direction as the waves, thus reducing the energy from the waves as they travel along the device.

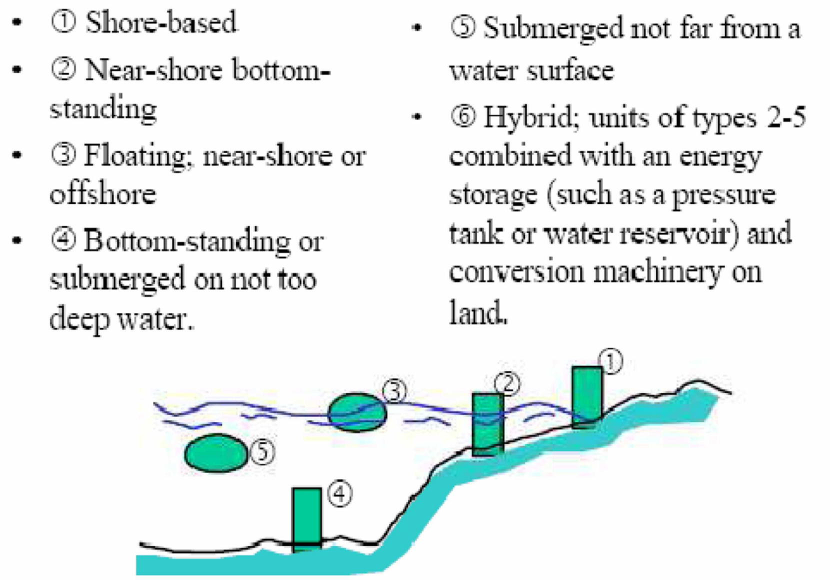

- ① Shore-based
- ② Near-shore bottom-standing
- ③ Floating; near-shore or offshore
- ④ Bottom-standing or submerged on not too deep water.
- ⑤ Submerged not far from a water surface
- ⑥ Hybrid; units of types 2-5 combined with an energy storage (such as a pressure tank or water reservoir) and conversion machinery on land.

Figure 4.1 *– First classification of WECs, as shore-line, near-shore or off-shore devices.*

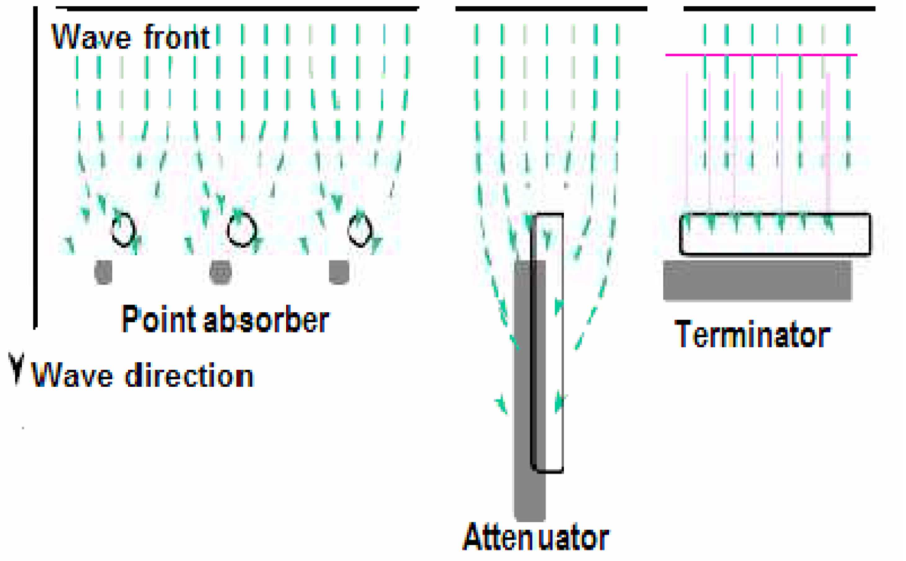

Figure 4.2 *– Second classification of WECs, as point absorbers, attenuators and terminators.*

The last classification here presented, is the most common kind of classification (proposed by Falcão and Rodrigues, 2002) and it is based on the conversion principle. The three categories are: Oscillating Water Columns (OWCs), Overtopping devices (OTDs) and Wave Activated Bodies (WABs).

OWCs are very common and studied. It usually consists of a partially submerged structure with a chamber below the sea water line from which waves enter the structure. Waves entrance changes the water level within the chamber and the rising and falling water level increases and decreases the air pressure, introducing a bidirectional air flow. By placing a turbine on top of this chamber air will pass in and out of it with the changing air pressure levels. There are two options to separate the bi-directional flow: a Wells turbine (e.g. Limpet concept) or valves to separate the flow into suction and pressure respectively (e.g. Leancon concept, Kofoed and Frigaard, 2008). OWC devices can be placed on the shoreline, where the waves break, or offshore, where the devices are moored to the ocean bottom.

In an OTD, waves run-up along a ramp, overtop in a storage reservoir above the sea level and the power is then obtained by exploiting the difference of water level between the reservoir and the sea. The overtopping WEC can be placed on the shoreline (first prototype based on this technology was the Tapchan concept http://taperedchannelwaveenergy.weebly.com/, and then SSG concept, http://www.waveenergy.no/) or off-shore (WaveDragon concept, http://www.wavedragon.net/).

WABs are usually composed by several parts, which interact due to the progressive wave action along the device. In fact waves activate the oscillatory relative motions of parts of the device or of one part with respect to a fixed reference. In order to exploit maximum energy, the moving elements need to be smaller than a wave length. The main disadvantage of these devices is the high cost of the power generator that needs to convert slow motion (at velocities of the order of wave celerity). The main advantage is that the structure is usually very compact and light. Indeed the first commercial WEC is of this type (www.pelamiswave.com). WABs can be further divided into sub-categories, based on the main solicited relative motion (heave, pitch and roll), for example: heaving buoys, pitch/surge devices, surge/heave/pitch devices and yaw/heave devices.

***Figure 4.3** – Third classification of WECs based on the conversion principle, i.e. from the left to the right: Limpet (fixed OWC, http://www.wavegen.co.uk/what_we_offer_limpet.htm), WaveDragon (floating OTD, http://www.wavedragon.net) and Pelamis (near-shore WAB, http://www.pelamiswave.com)*

Sometimes it is usual to describe a same WEC using more than one kind of classification (see Fig.s 4.4 and 4.5). The categories described above include most –but not all– of the technologies being developed today. A more detailed collection of the WEC concepts is summarized in Clément et al. (2002) as well as in Ingram et. al. (2011).

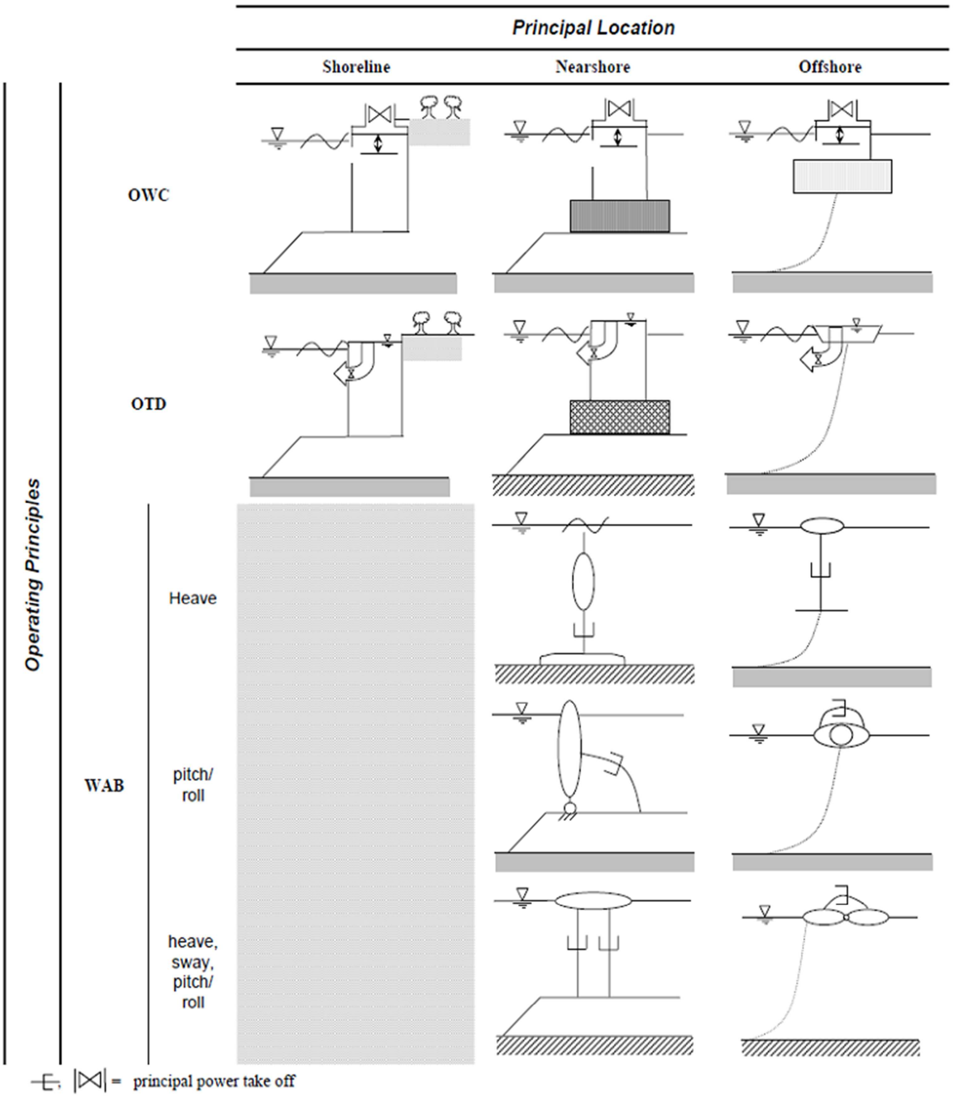

Figure 4.4 *– Schematic representation of the WECs taking into account the shoreline distance and their functional principle.*

		Directional Characteristic		
		Point Absorber	**Terminator**	**Attenuator**
Principal Location	**Shoreline**	▨	OWC, OTD	▨
	Nearshore	WAB	OWC, OTD, WAB	WAB
	Offshore	WAB	OWC, OTD, WAB	WAB

Figure 4.5 *– Combination of three WECs classifications proposed above, i.e. considering the distance from the shore-line, the direction with respect to the main incoming wave angle and the principle of working.*

Furthermore there are also several ways to categorize the development stages of emerging technologies. Since the early 2000s, many research groups (see Fig. 4.6) have shown significant progress in developing a series of standard, equitable approaches for both the development schedule and the test programmes of WECs from concept to demonstration. Nowadays, the main one is structured as a five-staged programme and born through the European FP7 EquiMar project (2010, http://www.equimar.org). Each stage may include several "Technology Readiness Levels" (TRLs), see Fig. 4.7. Conventional TRLs consist of nine development levels that enable the assessment of the technology maturity through its advancement.

Figure 4.6 *– Principal corporations engaged in drafting standards and protocols (after WavePlam Project, 2009).*

Figure 4.7 shows the five-staged approach progress from small scale model tests to intermediate tests and finally full scale sea demonstration. A WEC must fulfil clear stage gate criteria at the end of each stage before passing the latter stage of the development programme in order to mitigate technical and financial risk. Many failures occurred as the device developers have jumped directly to full scale after the initial investigations at small scales, e.g. Weber (2011, 2012) underlined the importance of improving performance and optimizing solutions by investing more at earlier stages. It is also worthy to remark that this procedure are in fully agreement with the standard design procedure established for the Danish conditions (Frigaard and Nielsen, 2008).

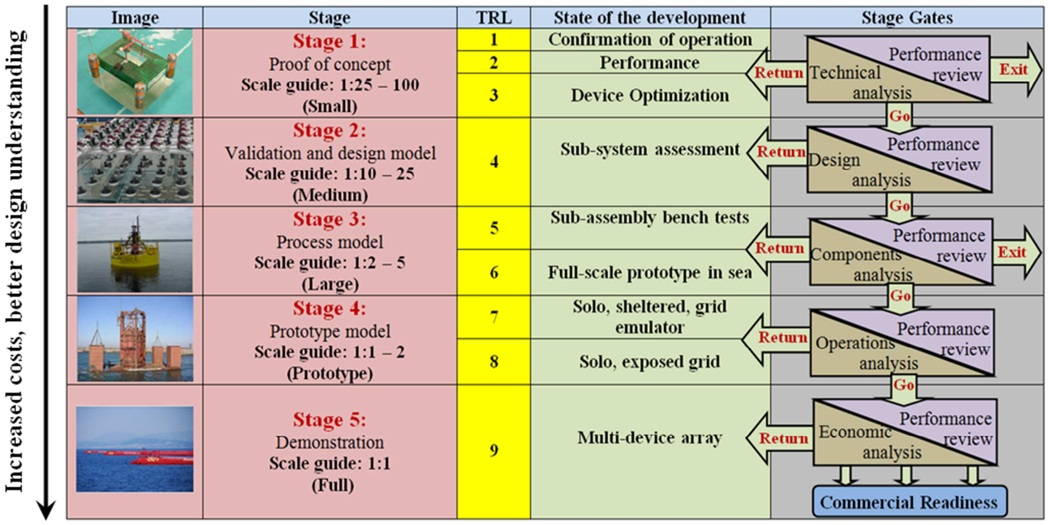

Figure 4.7 *– Structure of the five-stage development programme (after EquiMar, 2011).*

A lack of the internationally recognized standards leads to a negative influence on the credibility of the technology; on the whole, international guidelines not only offer greater technology mobility but also increase the potential of the device to benefit from the funding schemes.

Figure 4.8 shows the current development status of WECs based on five-staged approach. Although many working designs have been developed and numerical and laboratory tests have been performed on some concepts, only few have so far progressed to sea testing (more information are available leaf through WAVEPLAM project, 2009). Furthermore, from the figure it is possible to note that there are a relatively high number of WEC technologies emerging (i.e. at early stages), and also the total number of WECs are still growing, which indicates that the Research is still looking for an optimum design.

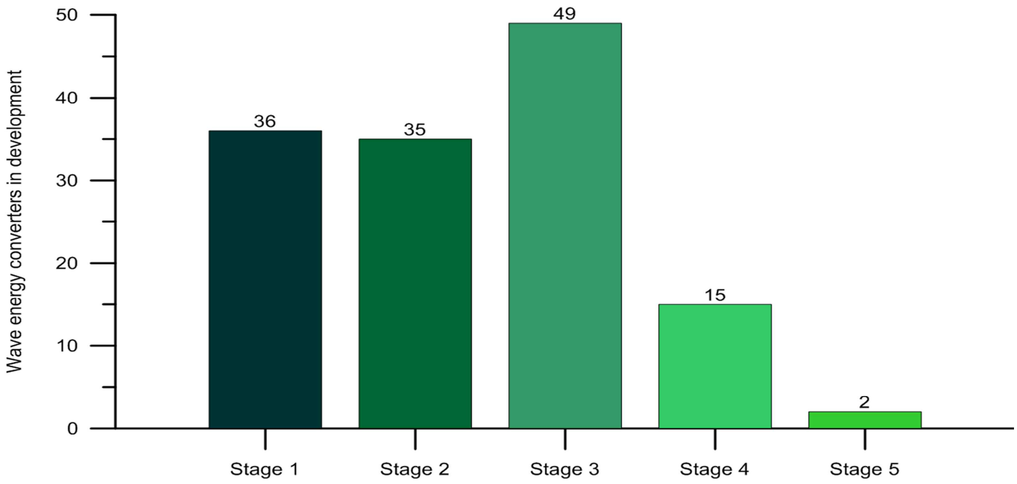

Figure 4.8 *– Current R&D on WECs based on five-staged approach (as of 03.02.2013).*

In addition to technical and financial issue, WEC deployments should also deal with environmental aspects –well known from other areas of marine technologies– such as corrosion, fatigue, stray current corrosion, marine growth, impact loading, etc. (Hudson et al, 1980).

To improve their installation it is necessary a further research, carried out under physical and numerical point of view, in order to better investigate wave farm aspects. In fact, so far in the literature there are several contributions related to single WECs, usually tested in a wave tank to jointly assess the power production and optimise the design, while investigation of WECs placed in farms –and on hydrodynamic induced by them or on the consequences for coastal defence– is rather limited. For this reason, the next chapter focus more in details on the WEC state of the art with particular interest on wave farm hypothesis.

5. LITERATURE REVIEW

As stated above, to facilitate the WECs commercialization a wave farm installation is required. However a wave farm installation leads to several challenges, such as the design and modelling of its layout, the occupied marine space and also its overall power production.

The area behind WECs is subject to lower wave intensity, since the WECs will partly reflect, partly absorb and partly dissipate the incident energy. When a single WEC is considered, at some distance behind it, wave energy is completely restored to its original levels by diffraction effects. However, this could be not the case for an array of devices. This aspect is linked with the "park effect", i.e. the interference on the WEC performance induced by the other WECs, concept known from the early '80s (Budal, 1977; Evans, 1979; Falnes, 1980), although there are not many indications about optimal layout and/or inter-distances among WECs.

Since wave-tank laboratories are few, expensive and often smaller to investigate wave farm effects, contributions on the WEC farm installation are essentially based on numerical simulations, and also mainly related to point absorbers (Evans, 1979; Ricci et. al., 2007; Millar et. al., 2006; Venugopal and Smith, 2007; Cruz et. al., 2009; Babarit, 2010; Borgarino et. al., 2011). In fact numerical models allow to tests more configurations at lower cost than physical models. Recently there were some exceptions, among them the experimental activities carried out in the Shallow Water Wave Basin of DHI (DK), on large arrays of up to 25 heaving point absorbers for a range of layout configurations and wave conditions (Troch et. al., 2013).

There are several numerical methods adopted so far to model the wave field around WECs based on different approaches, the common are: simplified modelling used for vessels, impact of wave farm as for the wind farm, 3D RANS-VOF Methods and 2DH models in shallow water.

A first approach is the traditional simplified modelling adopted for vessels and floating breakwaters, which is relative to the 2D case and based on the hypothesis of irrotational flow. Available commercial codes as WAMIT, AQWA, COMSOL, etc. are based on the Boundary Element Method. These models are typically implemented for uniform bottom, linear waves and do not account for viscous dissipation, hypotheses which become less accurate if referred to shallow water conditions (Cruz et. al., 2009). Furthermore these software analyse only the own motion of the bodies and not structure-waves interactions, and since they are usually apply in deep water, they almost neglect bottom effects. In several contributions (among them Kountandos, 2005) it is demonstrated that radiation effects from floating WECs on neighbouring devices are important, even if they are often neglected in most existing studies. Kountandos (2005) e.g. demonstrated that for an oscillating and floating breakwater the body-length to wavelength ratio has a strong effect on the response from a floating obstacle, and that reflection and transmission properties of floating obstacles are very dependent on the wave length.

A second approach consists of 2D or 3D models typically developed to assess the impact on the littoral of wind farms and then applied also to wave farms where the piles or devices are represented through an equivalent bottom friction or percentage of wave energy absorption respectively (Palha et. al., 2010). These simulations are usually done for environmental impact assessment purposes and do not consider model calibration.

A third approach uses 2DV and 3D RANS-VOF models to represent velocities and pressure around floating bodies. Simulations are usually always calibrated against experimental data in wave flume or tank. The first applications were performed on single and multiple floating breakwaters but fixed (Koftis and Prinos, 2005); more advanced research proposed 3D models combined with the external solution of the motion equation and iteratively solved. In this way it is possible to reproduce the presence of PTO or moorings by means of the external forces applied to the WEC (Agamloh et. al., 2008). Furthermore these kinds of software are applied also to shallow water situation, but they usually need huge processing time especially for 3D application.

A last approach uses 2DH models in order to reproduce the WEC wave transmission also suitable for shallow waters. This typology may include:

- 2DH mild slope models. Example of this approach is the study of Mendes et. al. (2008), where the depth integrated mild-slope REFDIF model (Kirby and Dalrymple, 1994) is adopted to simulate the energy extraction from WEC-farms off-shore the Portugal coast. Another example is related to the study performed by Beels et. al. (2010) used the MildWAVE model to reproduce the wave field around one or more Wave Dragons; the WECs are represented by a sponge layer with varying coefficients based on experimental data (Nørgaard and Poulsen, 2010). This study indicates that wake effect of the device is decreasing with increasing wave directional spreading.
- 2DH Boussinesq models. A first example of this approach can be found in Smith and Venugopal (2007). The authors examine the change in wave climate induced by an array of hypothetical WECs off the Orkney Islands. The study was carried out by using the MIKE 21 Boussinesq-model where the WECs were considered to be porous structures, with changing transmission/reflection-properties depending on wave conditions and porosity levels. The coefficient needs to be calibrated on experimental observations. The code MIKE 21 BW is able to represent reflection and diffraction at a reasonable computational time.

So far there is not a unique model able to predict the complete behaviour (hydrodynamic and dynamics) of a floating WEC with a realistic mooring and PTO, placed in a farm in shallow water.

The Boussinesq theory has been considered as an optimal compromise in order to obtain a preliminary attempt of the representation of the floating structure under exam tested in shallow water. Since with this code it is possible to reproduce only fixed bodies, a second numerical model was than performed to reproduce dynamic actions (device motions and mooring) with ANSYS-AQWA.

With MIKE 21 BW, the wave reflection and transmission from the WEC were modelled by using porous layers with calibrated coefficients around the device. The calibration was done considering the experimental results previously obtain during the first investigation phase.

6. THE DEVICE

The device under exam is a floating Wave Energy Converter (WEC) belonging to the Wave Activated Bodies (WAB) type. It consisted of two rigid pontoons with a hinge in between, which allowed each pontoon to pivot in relation to the other (see Fig. 6.1). The draft was such that at rest the free water surface passes in correspondence of the axis of the buoyant cylinders of the pontoons. This device is based on the DEXA concept (www.dexawave.com) which is in turn inspired to the Cockerell concept, optimizing it through a redistribution of buoyancy and force at the extremity of the pontoon (Wheeler, 2001).

Since it is floating, the arising parts and the fixed foundation are limited, therefore the environmental impact should be pretty low, furthermore its power take-off system has the same principle of operation of the Pelamis (http://www.pelamiswave.com), which is the only WEC at a commercialization phase. Additionally the WAB devices are less investigated for example with respect of point absorbers. All these reasons explain the choice on the study of this device.

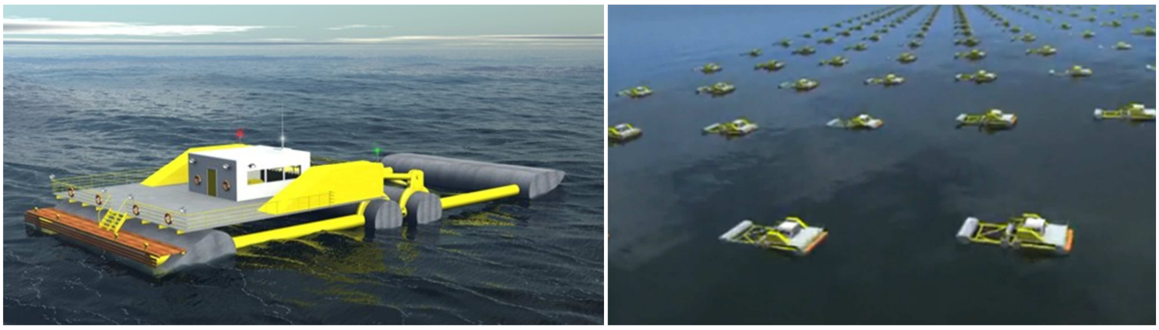

***Figure 6.1** – On the left, the DEXA concept. On the right, a rendering of a wave energy farm.*

As reported in the title the device was investigated under experimental and numerical point of view.

The experimental activities were performed in two basins of the Hydraulics and Coastal Engineering Laboratory at Aalborg University (DK). The models were reproduced in Froude similitude in scale 1:60 and 1:30, in order to represent near-shore conditions (water depths in the range 18-27m).

The numerical activities were carried out using two commercial codes: MIKE 21 BW, developed by DHI and ANSYS-AQWA, developed by ANSYS. Once the numerical parameters have been calibrated (based on the physical results), the numerical activities allow to confirm the laboratory results and at the same time to extend the result database.

PART A - EXPERIMENTAL MODELLING

The experimental modelling was performed in two phases, both at the Hydraulics Laboratory of Aalborg University (DK) in two different wave basins. Both the tanks have a constant depth and a bottom made in concrete. Furthermore, in both the basins, the wave generator is a paddle system controlled by the software AwaSys developed by the same laboratory (http://www.civil.aau.dk, Aalborg University, 2007) and it is able to generate regular and irregular long and short crest waves in the typical range: 0.03-0.20m as wave height, 0.8-2.0s as wave period in the deep basin and analogously 0.015-0.150m as wave height, 0.8-1.7s as wave period in the directional basin.

Another software –again developed by the same laboratory– named WaveLab, allow to simultaneously acquiring all the data at a chosen sample frequency (which was 20Hz for the first phase and 100 Hz for the second). This software supports also the Wave Gauges automatic calibration procedure, which was obtained by moving them up and down of 0.10 m with respect to the mean water level and saving the corresponding voltage values.

The main targets of the first phase were the analysis of the water depths, the wave obliquity, the device interactions, the scale effects and the mooring typology.

Whereas the second phase focused more on the effects of the wake extension, of a realistic power take-off (PTO) system on the devices of a wave farm module and of different mooring pre-tension levels.

The device was tested under regular and irregular waves, in the typical wave climate of future site installations, i.e. wave height, wave period in the range 2-5m, 5.6-11s respectively, and water depths 18-27m.

This chapter reports the main results for the whole experimental activities.

7. FIRST INVESTIGATION

7.1. LABORATORY SET-UP

The basin is 15.70 m long (in waves direction), 8.50 m wide and locally 1.50 m deep. The wave generator is a snake-front piston type composed of 10 actuators with stroke length of 0.50 m, enabling generation of short-crested waves. The wave absorption is assured by a 1:4 dissipative beach made of concrete and gravel with D_{50}=5 cm placed opposite to the wave-maker.

During the first investigation the device was reproduced in two Froude scale: 1:60 and 1:30. Three models in 1:60 scale were available, and each model was 0.95 m long and 0.38 m wide (perpendicularly to wave propagation), and each pontoon consisted of two cylindrical floaters (see Fig. 7.1). An elastic resistant strip is placed in between the pontoons in order to connect them. The total weight of each model is 3.30 kg. These models did not carry PTO systems or measurement instrumentations on board. The models were moored with four steel chains (0.25 kg/m), 1.5m long, with a “spread” system (Harris et al., 2004). Each chain is fixed to the bottom with heavy anchors (3.00 kg) and is linked to the device at the fairlead point in the middle of the legs by means of a resistant plastic strip. The anchor positions were determined in order to have the projection of the chain on the floor equal to 1/3 of the total chain length.

The three models were deployed in the basin in order to represent a module of a staggered wave farm. In particular the module was composed by a first line (towards the wave-maker) with two models (device nr. 1 and 2 in Fig. 7.2, with a 3.10 m wide central gap in between) and a second farm line with the third model (device nr.3) placed just behind the gap. Two water depths were used, h_1=0.30 m, h_2=0.35 m and only few test were performed with h_3=0.40 m (further information available in the Internal Deliverable ID 2.5 of the Theseus Project.

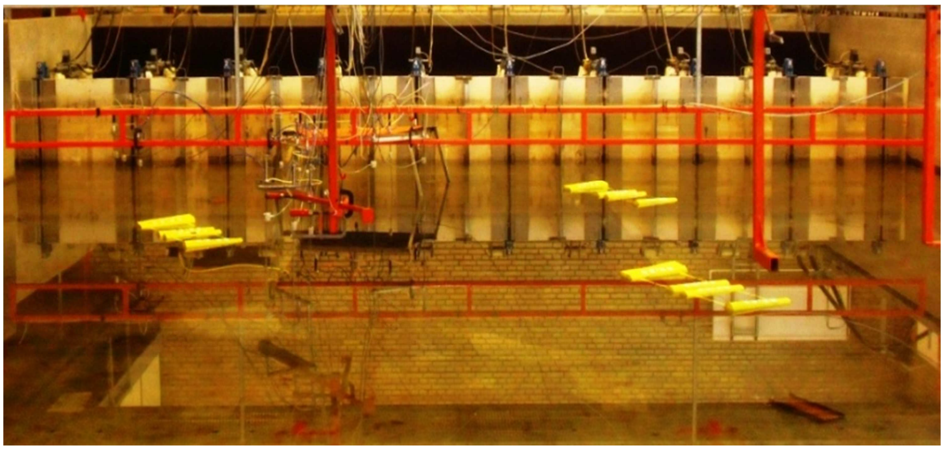

***Figure 7.1** – 1:60 scale models placed in the staggered configuration with spread moorings.*

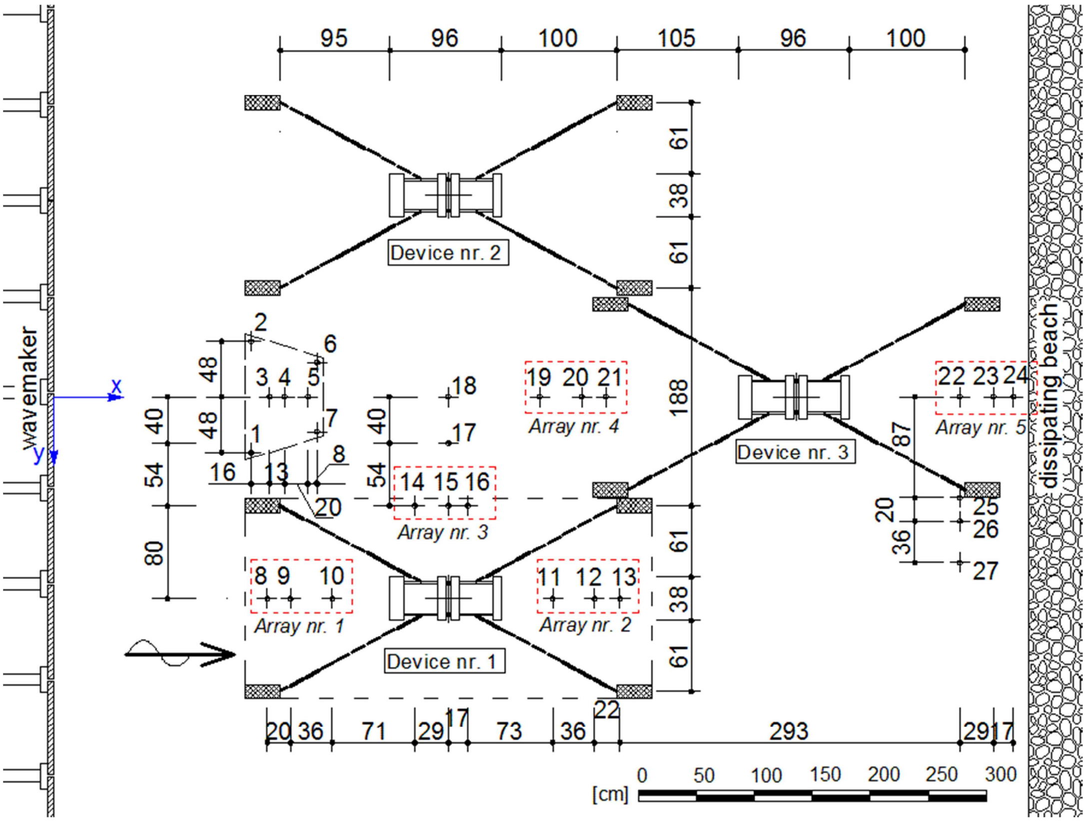

__Figure 7.2__ – Scheme of the wave farm module with its measurements. Distances are in cm.

The model in 1:30 scale, instead, was 2.10 m long and 0.81 m wide (perpendicularly to wave propagation, see Fig. 7.3), and totally weighs 33.00 kg including the PTO (i.e. the device singularly weighs 23 kg, whereas the PTO system weighs 10 kg). The PTO system consists of a metal bar with an elongate-shaped hole, a wire welded at the two ends of the hole and a small electric engine with a wheel. The bar is connected to one half of the device and the wheel to the other, via a load cell (strain gauge equipped “bone”). The wire is rolled up around the wheel that is forced to rotate while translating along the bar hole. The rigidity of the PTO is modified by varying the resistance of the wheel to rotation and therefore the current in the engine, so that the body rigidity is changed (totally it is possible to set up 17 rigidities). Two mooring system were investigated with this model. The first mooring system was analogous to the one used in 1:60 scale, i.e. a “spread” system with four steel chains, each 3.00m long and fixed to the bottom with heavy anchors (30 kg) and is linked to the device at the fairlead point in the middle of the legs by means of a resistant plastic strip (see Fig. 7.3). The second type of mooring system used is so-called “catenary anchor leg mooring” (CALM) system (Harris et al., 2004). In this case, the device is linked to a catenary moored buoy and it is able to rotate around it according to the prevailing wave direction (see Fig. 7.4). In the laboratory, the CALM system was reproduced through four 3.00 m long chains (1.00 kg/m), fixed to the bottom with heavy anchors (30 kg).

Their fairleads were together connected to a cylindrical polystyrene buoy, whose diameter was 0.28 m. The buoy was linked to the device through a 1.30 m long elastic cable. Both the mooring systems were tested at a water depth *h* equals 0.60 m.

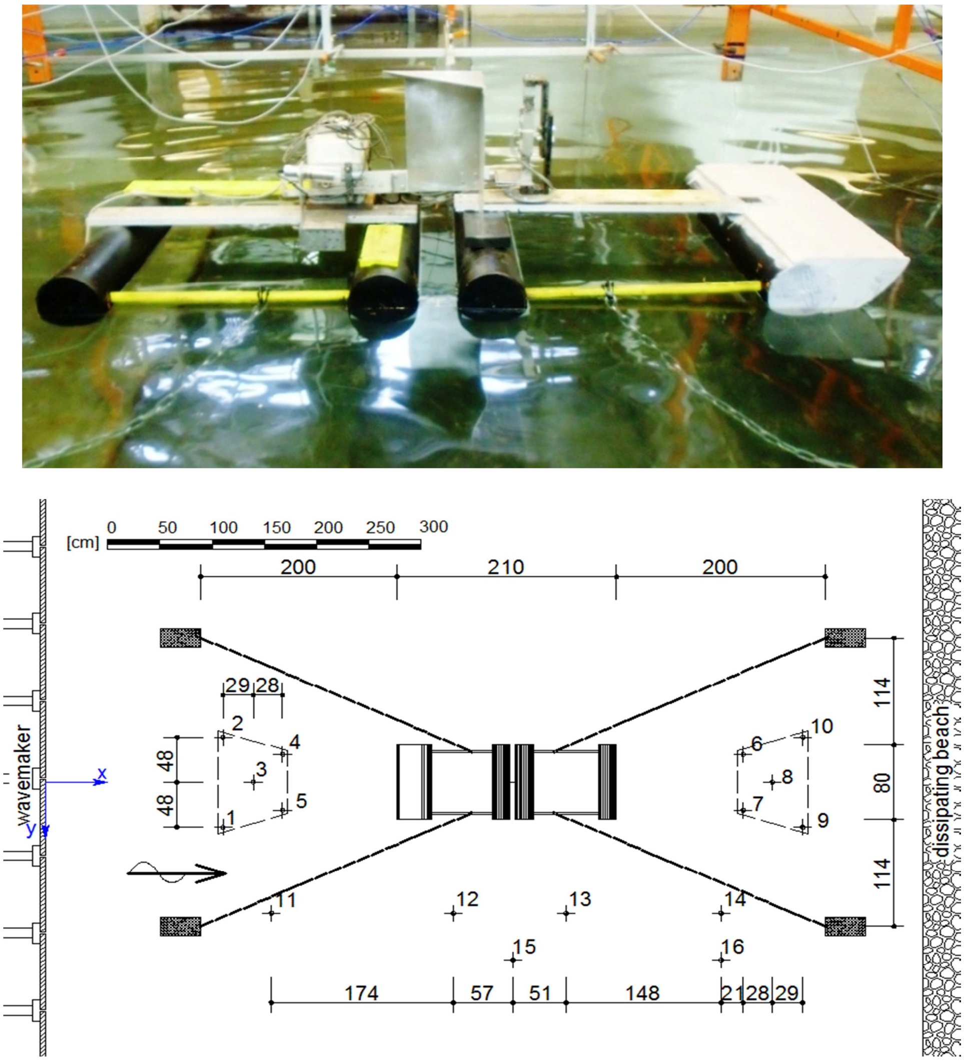

***Figure 7.3** – 1:30 model with the "spread" mooring system. On the top: picture of the laboratory configuration; on the bottom: scheme with the model and its measurements. Distances are in cm.*

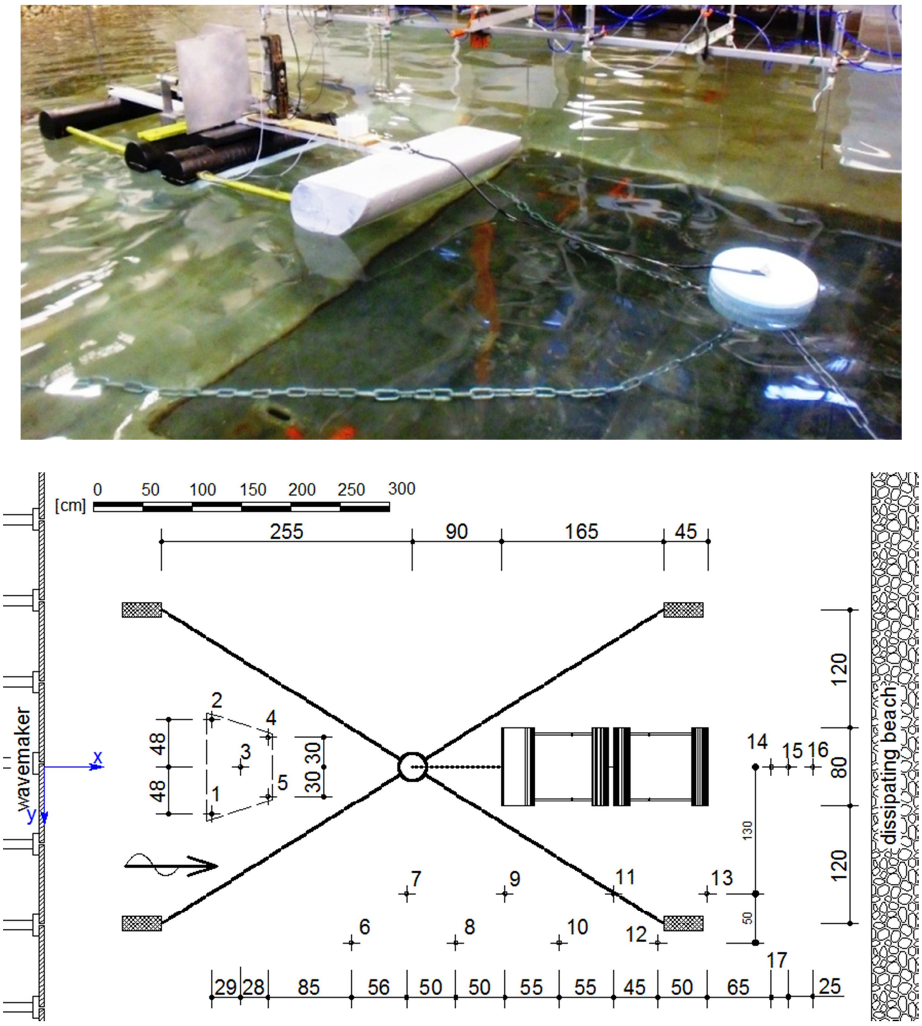

***Figure 7.4** – 1:30 model with the CALM mooring system. On the top: picture of the laboratory configuration; on the bottom: scheme with the model and its measurements. Distances are in cm.*

Both the configuration were subject to several wave states (WSs), reported in tables 7.1 and 7.2 (for 1:60 and 1:30 scale tests respectively), including also different wave obliquities (β=0-15-30°). The WSs represents a wave climate similar to the North Sea conditions and were reproduced as irregular 3D short-crested waves with Jonswap spectrum (directional spreading factor of 10).

WSs in table 7.1 are perfectly in scale with the ones given in table 7.2, with the exception of WSs nr. 1 and 2 in the table 7.2 that were not carried out in 1:60 scale due to wave-maker limitations in reproducing small waves. Three extreme WSs, corresponding to 10, 50 and 100 years return periods, were tested in 1:60 scale for both h_1 and h_2 (see Tab. 7.1). Such WSs were not performed in 1:30 scale due to limited depth of the wave basin.

h_1=0.30 m				*h_2=0.35 m*				*h_3=0.40 m*			
Ordinary waves											
WS	*H_s [m]*	*T_p [s]*	*L_p [m]*	***WS***	*H_s [m]*	*T_p [s]*	*L_p [m]*	***WS***	*H_s [m]*	*L_p [m]*	*T_p [s]*
1	0.050	0.74	0.80	**1**	0.050	0.73	0.80	**1**	0.033	0.85	0.74
2	0.050	0.84	1.04	**2**	0.050	0.83	1.04	**2**	0.033	1.05	0.83
3	0.050	1.01	1.42	**3**	0.050	1.00	1.42	**3**	0.050	1.39	0.97
4	0.050	1.37	2.12	**4**	0.050	1.31	2.12	**4**	0.050	2.09	1.27
5	0.067	1.01	1.38	**5**	0.067	1.00	1.38	**5**	0.067	1.39	0.97
6	0.067	1.37	2.05	**6**	0.067	1.31	2.05	**6**	0.067	2.00	1.23
7	0.083	1.01	1.38	**7**	0.083	1.00	1.38	**7**	0.083	1.39	0.97
8	0.083	1.37	2.12	**8**	0.083	1.31	2.12	**8**	0.083	2.09	1.27
Extreme waves											
9	0.130	1.67	2,66	**9**	0.130	1.67	2,84	**9**	0.130	1.67	2,99
10	0.147	1.77	2,84	**10**	0.147	1.77	3,04	**10**	0.147	1.77	3,21
11	0.164	1.86	3,01	**11**	0.164	1.86	3,211	**11**	0.164	1.86	3,40

Table 7.1 *– Irregular tested WSs in 1:60 scale.*

Irregular WSs					***Regular WSs***				
WS	*H_s [m]*	*T_p [s]*	*L_p [m]*	*P_w [W]*	***WS***	*H [m]*	*T_p [s]*	*L_p [m]*	*P_w [W]*
1	0.067	1.05	1.67	1.35	**1**	0.047	1.05	1.67	2.86
2	0.067	1.19	2.02	1.88	**2**	0.047	1.19	2.02	3.64
3	0.100	1.05	1.73	3.34	**3**	0.070	1.05	1.73	6.45
4	0.100	1.19	2.10	4.50	**4**	0.070	1.19	2.10	8.97
5	0.100	1.43	2.66	6.06	**5**	0.070	1.43	2.66	5.22
6	0.100	1.94	4.28	10.33	**6**	0.070	1.94	4.28	18.33
7	0.133	1.43	2.88	11.14	**7**	0.093	1.43	2.88	9.83
8	0.133	1.94	4.28	18.44	**8**	0.093	1.94	4.28	26.96
9	0.167	1.43	2.88	16.47	**9**	0.117	1.43	2.88	16.70
10	0.167	1.94	4.28	27.59	**10**	0.117	1.94	4.28	37.88

Table 7.2 *– Irregular and regular tested WSs in 1:30 scale.*

All these tests were performed under 0°, 15° and 30° wave obliquities with exception of WSs nr. 1, 4 and 7 in table 7.1 and nr. 3, 6, 9 in table 7.2, which were performed only under 0°. Oblique waves were obtained by rotating all the devices and measurement equipment around a fixed reference point in the basin (corresponding to the wave gauge nr.4 for the 1:60 scale, and to the wave gauge nr.3 for the 1:30 scale).

The main measurements were hydrodynamic measurements. Furthermore in the configuration 1:30, a force transducer (equipped bone) and an ultrasonic displacement sensor were used on board of the model (to evaluate its power performance), these measurements were opportunely calibrated.

The hydrodynamic measurements were performed by using in the basin a number of resistive Wave Gauges (WGs), which give the instantaneous value of the surface elevation.
In total, 27 WGs were deployed in the basin in 1:60 scale (see Fig. 7.2) and 16 WGs in 1:30 scale (see Fig.s 7.3 and 7.4).
In particular, in scale 1:60, the first seven WGs nr. 1-7 were deployed into a front WGs array, whereas the other WGs were mainly placed in groups of three WGs, i.e.:

- WGs nr 8-10 were placed in front of one of the devices along the first line of the wave farm; these WGs composed Array nr. 1;
- WGs nr 11-13 were placed behind one of the devices along the first line of the wave farm and composed Array nr. 2;
- WGs nr. 14-16 were placed on the side of one of the devices along the first line of the wave farm; these WGs composed Array nr. 3;
- WGs 19-21, just in front of the third device (i.e. the second line of the wave farm) composed to Array nr. 4;
- WGs 22-24 were placed in front of the beach and behind the second line of the wave farm; these WGs composed Array nr. 5.

In scale 1:30, two arrays of five WGs were placed in front of and behind the device and the remaining 6 WGs were placed on the left side of the device, in case of spread mooring. In case of CALM mooring system, the WGs were placed in one array of five WGs in front of and one array of three WGs behind the device and the remaining 8 WGs were placed on the left side of the device.

To separate the incident from the reflected waves, it is possible to use the Bayesian Directional Method (BDM) (Hashimoto and Kobune, 1988) to data of array of 5 or 7 WGs, whereas data from array of 3 WGs can be derived through the Mansard and Funke's method (Mansard and Funke, 1980).

7.2. RESULTS IN SCALE 1:60

The hydrodynamic data were elaborated in the time and frequency domains.

In the frequency domain, at each group of three WGs, the incident wave field has been divided from the reflected one. The loose of wave energy due to the device presence can be quantified using the transmission K_T and reflection K_R coefficients. K_T is defined as the ratio between the incident and the transmitted wave height, whereas K_R is the ratio between the reflected and incident wave height. Their definition is recalled for convenience below:

$$K_T = \frac{H_T}{H_I} \tag{1}$$

$$K_R = \frac{H_R}{H_I} \tag{2}$$

Based on equation (1), four values of K_T are used in the following:

- K_{T1} is calculated between Array nr. 1 and Array nr. 2. It represents the transmission coefficient of the device placed in the first farm line.
- K_{T2} represents the overall transmission of the first farm line. H_I is the H_{m0} derived from Array nr. 1, whereas H_T is H_{m0} calculated through a weighted average based on the values derived from Array nr. 1 and Array nr 2. By assuming the axial symmetry of the hydrodynamics, the weights assigned to Arrays nr. 1 and nr. 2 are respectively two times the width between the front device anchors (1.60 m each) and the width of the central gap plus two times the distance between the device and the basin wall (1.90 m + 3.01 m).
- K_{T3} represents the transmission coefficient induced by the device placed along the second farm line. H_I and H_T are derived respectively from the Arrays nr. 4 and nr. 5.
- K_{T4} is the transmission coefficient behind the second farm line. H_I is derived from the Array nr. 1 whereas H_T is calculated through a weighted average among Arrays nr. 1, nr. 2 and nr. 5. The weights are respectively: for Array nr. 2, two times the width between the front device anchors (1.60 m each); for Array nr. 5, the width of the central gap; for Array nr. 1, two times the distance between the device and the basin wall (3.40 m).

An attempt of evaluation of K_{T2} and K_{T4} has been proposed in order to provide a better description of the wave transmission, being K_{T1} and K_{T3} related to the single device, therefore not particularly representative of the amount of the resulting incident wave energy on the coast.

As regards the wave reflection, based on equation (2) two values of K_R can be defined, K_{R1} and K_{R3}, whose values are respectively evaluated at the Arrays nr. 1 and nr. 4.

Results of K_T and K_R, related to perpendicular shot-crested WSs, are reported in tables 7.3 and 7.4, further data are available in the Internal Deliverable ID 2.5 of the Theseus Project.

	WS	**1**	**2**	**3**	**4**	**5**	**6**	**7**	**8**		**9**	**10**	**11**
3D $\beta=0°$ h_1	K_{T1}	0.88	0.96	0.97	0.97	0.97	0.97	0.99	0.96	**Extreme Waves**	0.95	0.93	0.91
	K_{T2}	0.95	0.98	0.99	0.99	0.99	0.99	0.99	0.98		0.98	0.97	0.96
	K_{T3}	0.94	0.97	0.95	0.95	0.92	0.91	0.92	0.89		0.88	0.90	0.88
	K_{T4}	0.94	0.98	0.98	0.98	0.97	0.97	0.98	0.96		0.95	0.95	0.93
	K_{R1}	0.32	0.28	0.23	0.18	0.23	0.18	0.25	0.19		0.17	0.18	0.18
	K_{R2}	0.34	0.28	0.21	0.17	0.20	0.16	0.22	0.17		0.17	0.19	0.21

***Table 7.3** – Values of K_T and K_R under 3D perpendicular WSs with the water depth h_1.*

	WS	**1**	**2**	**3**	**4**	**5**	**6**	**7**	**8**		**9**	**10**	**11**
3D $\beta=0°$ h_2	K_{T1}	0.84	0.92	0.96	0.95	0.94	0.97	0.96	0.95	**Extreme Waves**	0.93	0.93	0.93
	K_{T2}	0.94	0.97	0.98	0.98	0.98	0.99	0.98	0.98		0.97	0.97	0.97
	K_{T3}	0.92	1.01	1.00	0.95	0.96	0.95	0.94	0.92		0.89	0.89	0.89
	K_{T4}	0.92	0.97	0.98	0.97	0.97	0.98	0.97	0.96		0.95	0.95	0.95
	K_{R1}	0.33	0.30	0.25	0.22	0.25	0.20	0.24	0.20		0.18	0.19	0.19
	K_{R2}	0.34	0.29	0.24	0.21	0.22	0.18	0.22	0.19		0.18	0.18	0.19

***Table 7.4** – Values of K_T and K_R under 3D perpendicular WSs with the water depth h_2.*

A great amount of wave motion is transmitted behind a single device and behind the farm since values of K_T are always greater than 0.75, the higher values correspond to the more energetic WSs. The trend of K_T for the same wave obliquity by changing the water depths, or for the same water depth by changing the wave obliquity is reported in figures 7.5-7.6 as function of l/L_P, where l is the device length and L_P is the incoming peak wave length. Preliminary tests on the model in 1:30 scale showed that K_T and efficiency η tend to decrease and increase respectively with increasing the dimensionless length l/L_P (Zanuttigh et al., 2010). These new tests confirmed this dependence of K_T on l/L_P.

Figure 7.5 reports the trend of K_{T1} and K_{T3} against l/L_P under perpendicular WSs for h_1 and h_2. It is possible to note that the values of K_{T1} are higher than the values of K_{T3}, and the reason is due to the higher sheltered area of the device of the second line with respect to the device of the first line. Furthermore the figure shows the water depth effects, there are slightly differences, however the higher the water depth the lower the K_T.

For both the water depths, K_{T1} shows lower values with increasing wave obliquity and an almost linear decrease with l/L_P, especially for h_2 (see Fig. 7.6). Unlike K_{T1}, K_{T3} instead, increases with increasing the wave obliquity, i.e. when the device tends to re-orient itself according to the incident wave direction. This phenomenon is also confirmed by the fact that K_{T3} is greater for β_3 rather than for β_2.

The wave transmission induced by the first line and the whole farm (K_{T2} and K_{T4}) seems to weakly depend on the l/L_P and on the wave obliquity, mainly due to the opposite trends of K_{T1} and K_{T3}. Furthermore it appears not particularly sensitive to changes in water depths and therefore to climate change, especially under oblique waves.

In addition, the K_T derived for the single device and for the line/s of the farm do not significantly depend on the wave steepness.

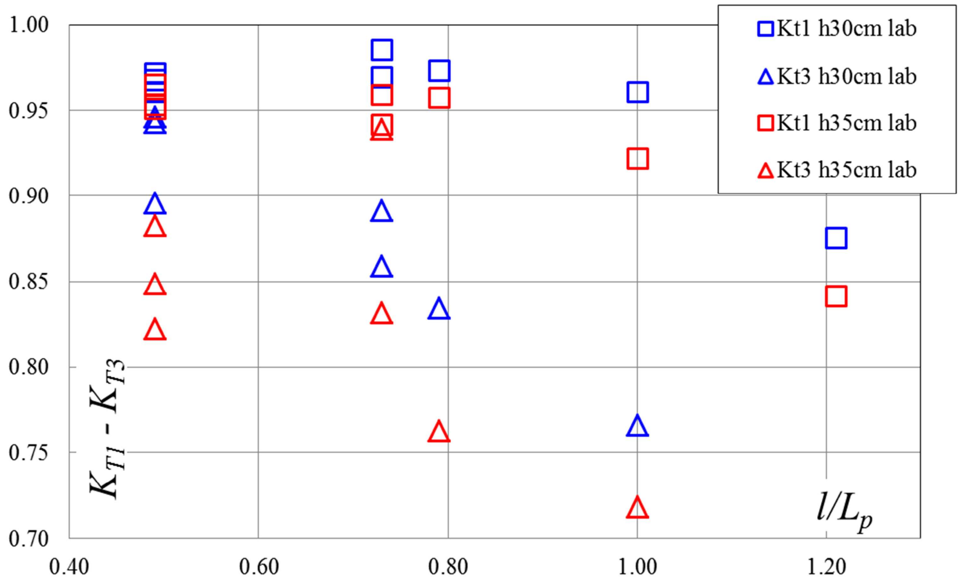

***Figure 7.5** – K_{T1} and K_{T3} against l/L_P under perpendicular WSs for h_1 and h_2*

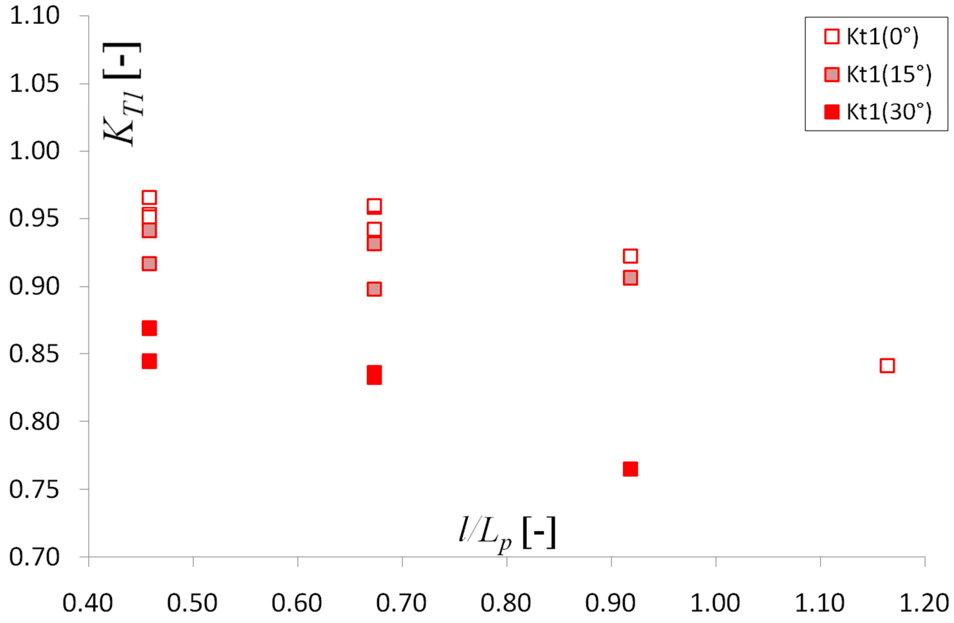

Figure 7.6 *– K_{T1} against l/L_P for h_2 and for different obliquities.*

The trend of K_R, instead, seems the opposite with respect to K_T, in fact it tends to almost linearly increase with increasing l/L_P. A modest fraction of the incident wave height is reflected by the device, being K_R often lower than 0.50, and the higher K_R values are reached under oblique WSs with β=15° (see Fig. 7.7).

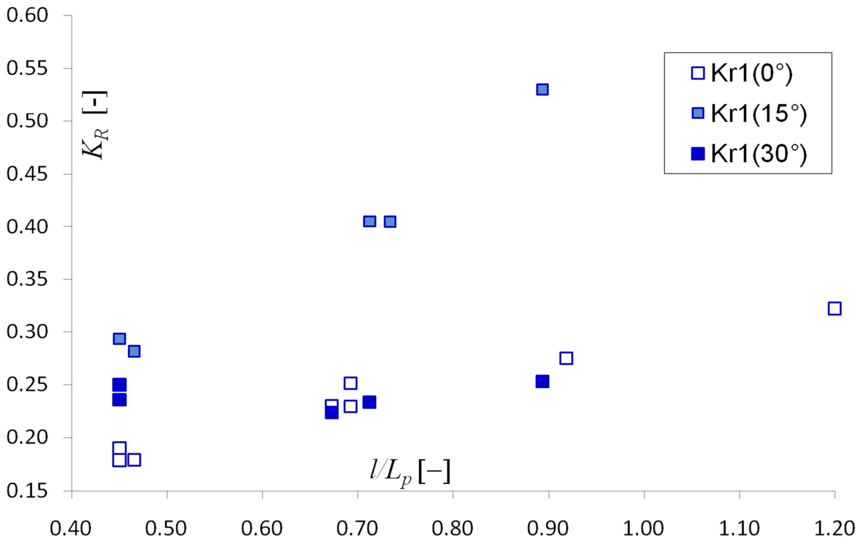

Figure 7.7 *– K_{R1} against l/L_P for h_1 and for different obliquities.*

In the time domain, the values of the significant wave height H_S, has been derived through the zero-down-crossing procedure for every WG. Examples of the results of this elaboration, for the perpendicular short-crested WSs, are reported in tables 7.5 and 7.6, further results are available in the Internal Deliverable ID 2.5 of the Theseus Project.

	WSs										
WG	**1**	**2**	**3**	**4**	**5**	**6**	**7**	**8**	**9**	**10**	**11**
1	1.08	1.22	1.62	2.13	2.55	2.93	3.10	3.82	6.66	7.54	8.65
2	1.13	1.29	1.56	2.17	2.38	2.92	2.96	3.72	6.37	7.16	8.37
3	1.02	1.20	1.55	2.25	2.51	3.04	3.05	3.92	6.61	7.54	8.73
4	1.09	1.27	1.65	2.36	2.62	3.17	3.19	4.09	6.89	7.69	8.99
5	1.08	1.27	1.64	2.28	2.58	3.08	3.14	4.00	6.69	7.61	8.74
6	1.14	1.32	1.65	2.28	2.54	3.06	3.08	3.93	6.68	7.54	8.55
7	1.10	1.29	1.63	2.18	2.58	3.03	3.14	3.91	6.45	7.37	8.54
8	1.90	1.82	1.90	2.19	2.62	2.72	3.20	3.66	6.58	7.09	8.43
9	1.92	1.86	1.99	2.26	2.72	2.81	3.34	3.78	6.75	7.37	8.62
10	1.90	1.92	1.97	2.27	2.69	2.88	3.37	3.75	6.63	6.96	8.28
11	1.67	1.91	2.03	2.26	2.75	2.85	3.46	3.73	6.27	6.41	7.39
12	1.65	1.80	1.90	2.14	2.63	2.72	3.26	3.52	5.82	6.13	6.98
13	1.65	1.80	1.88	2.11	2.57	2.68	3.23	3.46	5.87	6.16	6.95
14	1.56	1.75	1.87	2.20	2.44	2.67	3.15	3.68	6.28	6.91	7.85
15	1.55	1.74	1.80	2.11	2.36	2.59	3.04	3.55	6.13	6.68	7.61
16	1.55	1.67	1.76	2.06	2.30	2.55	2.99	3.44	5.81	6.28	7.24
17	1.41	1.66	1.91	2.16	2.38	2.78	3.24	3.72	6.30	6.82	7.56
18	1.43	1.77	1.97	2.33	2.54	2.98	3.41	3.87	6.69	7.35	8.03
19	1.40	1.55	1.84	2.23	2.80	3.05	3.31	3.91	6.13	7.00	7.66
20	1.37	1.49	1.70	2.10	2.61	2.82	3.10	3.65	5.69	6.38	7.01
21	1.37	1.51	1.70	2.07	2.56	2.82	3.09	3.63	5.66	6.33	6.91
22	1.30	1.46	1.69	2.13	2.43	2.80	2.90	3.48	5.25	5.95	6.10
23	1.25	1.41	1.67	2.04	2.43	2.67	2.87	3.35	5.19	5.80	6.03
24	1.26	1.40	1.61	1.95	2.33	2.57	2.79	3.22	5.05	5.56	5.80
25	1.34	1.52	1.69	1.96	2.43	2.63	2.90	3.22	5.24	5.75	6.10
26	1.43	1.62	1.72	1.97	2.50	2.63	3.02	3.28	5.42	5.92	6.35
27	1.47	1.64	1.74	1.92	2.56	2.57	3.08	3.24	5.41	5.92	6.41

Table 7.5 *– H_S values in full scale for the small models under 3D perpendicular WSs with h_1.*

	WSs										
WG	**1**	**2**	**3**	**4**	**5**	**6**	**7**	**8**	**9**	**10**	**11**
1	1.19	1.26	1.57	1.99	2.38	2.76	3.42	3.88	5.9	6.93	7.87
2	1.13	1.2	1.44	1.83	2.11	2.59	3.35	3.61	5.8	6.84	7.7
3	1.03	1.11	1.48	1.95	2.17	2.77	3.39	3.89	6.17	7.23	8.18
4	1.1	1.19	1.59	2.03	2.28	2.9	3.37	3.85	6.38	7.35	8.27
5	1.08	1.17	1.56	1.96	2.23	2.81	3.35	3.85	6.41	7.37	8.3
6	1.18	1.27	1.59	1.97	2.3	2.85	3.48	3.86	5.94	6.84	7.55
7	1.13	1.21	1.57	1.96	2.28	2.77	3.4	3.81	5.96	6.84	7.46
8	1.86	1.94	2	2.13	2.64	2.95	3.35	3.71	5.55	6.15	6.78
9	1.88	1.93	2.07	2.18	2.7	2.97	3.42	3.77	5.31	6.01	6.57
10	1.83	1.95	2.05	2.19	2.64	3.02	3.36	3.74	5.42	6.19	6.7
11	1.58	1.89	2.11	2.15	2.66	2.98	3.38	3.68	5.4	6.11	7.02
12	1.53	1.79	1.97	2.03	2.51	2.8	3.23	3.51	5.49	6.23	7.19
13	1.55	1.78	1.94	2.02	2.5	2.8	3.22	3.51	5.5	6.16	6.96
14	1.61	1.69	1.86	2.13	2.5	2.88	3.24	3.63	5.9	6.93	7.87
15	1.57	1.71	1.84	2.09	2.44	2.77	3.17	3.52	7.1	8.35	9.53
16	1.55	1.64	1.76	2.04	2.41	2.71	3.07	3.42	6.5	7.22	8
17	1.61	1.61	1.77	2.16	2.55	2.96	3.35	3.67	7.11	8.07	9.03
18	1.62	1.64	1.78	2.14	2.57	2.98	3.42	3.87	6.85	7.71	8.66
19	1.38	1.46	1.71	2.04	2.51	2.83	3.53	3.78	6.8	7.64	8.52
20	1.28	1.36	1.53	1.81	2.24	2.57	3.38	3.6	7.03	8.05	8.87
21	1.31	1.37	1.53	1.81	2.28	2.53	3.34	3.51	6.92	7.99	8.94
22	1.22	1.42	1.61	1.86	2.3	2.64	3.24	3.5	6.35	7.3	8.26
23	1.17	1.37	1.56	1.79	2.26	2.54	3.15	3.29	6.35	7.42	8.34
24	1.15	1.34	1.53	1.73	2.16	2.47	3.11	3.27	6.09	7.03	7.91
25	1.3	1.49	1.64	1.75	2.23	2.48	3.11	3.34	5.74	6.55	7.48
26	1.38	1.56	1.73	1.79	2.3	2.52	3.17	3.37	5.55	6.21	7.11
27	1.42	1.57	1.74	1.78	2.29	2.48	3.25	3.34	5.57	6.25	7.05

Table 7.6 *– H_S values in full scale for the small models under 3D perpendicular WSs with h_2.*

In order to confirm the aspect of a wave interaction among the devices, supposed by comparing K_{T1} and K_{T3}, the H_S data derived from the WGs n. 15, 17-21 were compared. In particular, the analyse the existence and the intensity of mutual interactions between the models has been carried out both in cross-shore direction (through WGs n. 18-21) and in long-shore (through WGs n. 15, 17, 18).

Figure 7.8 reports the H_S at the WGs n. 18-21 against the distance from the basin axes (all the values are in full scale). Along the x axis (i.e. cross-shore direction), H_S decays from the middle of the gap (WG nr. 18) to the device closer to the shore (WG nr. 21) both for h_1 and h_2. Such decrease is less pronounced (or absent) for oblique waves. Furthermore for perpendicular waves, by comparing $H_{m0,4}$, i.e. the H_{m0} at the Arrays nr. 4, and $H_{m0,1}$, i.e. the H_{m0} at the Array nr. 1, it follows that $H_{m0,4}$ is lower than $H_{m0,1}$, hence the superposition of the first line device wakes leads to a destructive wave interaction behind them, just in the zone facing the rear device. In case of oblique attacks instead, the zone in front of the device nr. 3 seems not affected by the device wake superposition.

Figure 7.9 reports the H_S at the WGs n. 15, 17-18, starting from the y axis origin (WG n. 18) to the device n.1 (see Fig. 7.2). Along the y axis (i.e. long-shore direction), the constructive wave interaction is more pronounced for orthogonal waves than for oblique attacks, where H_S decays from the WG n.18 to the WG n.15. The constructive wave interaction between the devices in the first farm line can be noticed also comparing *HS* at the WG n.8 ($H_{S,WG8}$) and H_S at the WG n.18 ($H_{S,WG18}$): the values of $H_{S,WG8}$ are lower than the values of $H_{S,WG18}$ for all the WSs, and for the extreme WSs this decay is more relevant.

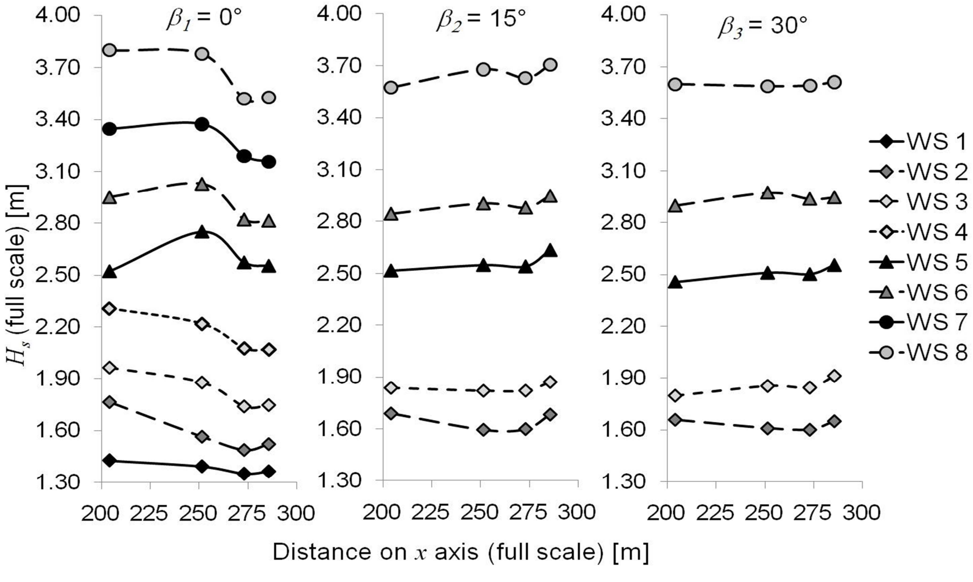

***Figure 7.8** – Wave field along x axis (cross-shore) in the gap for ordinary WSs and for* h_1

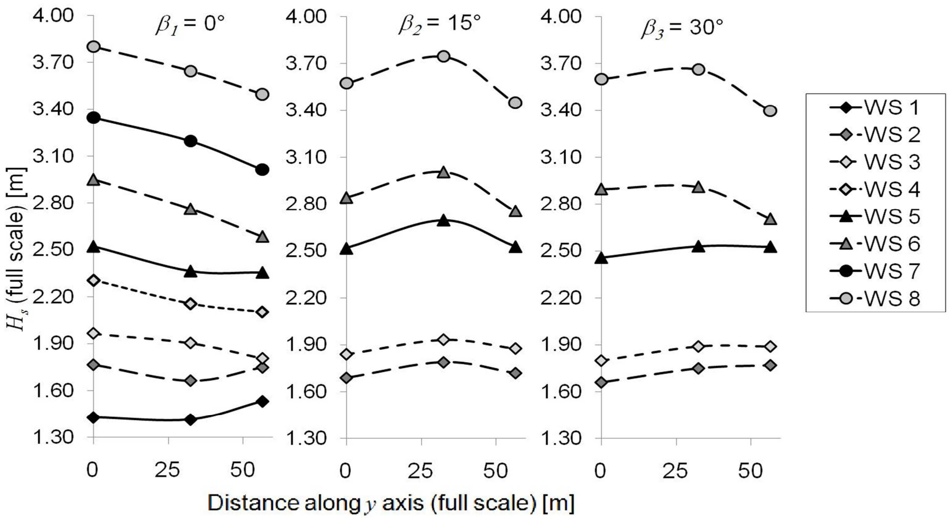

***Figure 7.9** – Wave field along y axis (long-shore) in the gap for ordinary WSs and for h_1.*

For a more complete assessment of the wave energy behind the wave farm, wake effects were investigated by analysing the H_S derived from the WGs n.22, 25, 26 and 27. The distribution of H_S in the wake of the device shows the same trend both for h_1 and for h_2.

Figure 7.10 reports the H_S values as function of the distance from the device axis (and basin axis), for every WS, obliquity and water depth h_2. It can be observed that Hs in the device wake strongly depend on β. In case of ordinary perpendicular WSs, the values of H_S are affected by scattered waves, which are generated by the model during its heaving motion. In some cases, H_S decays from WG nr. 22 to WG nr 27, especially for the higher WSs. For the ordinary oblique WSs, the variation of H_S in long shore direction is less marked compared to the perpendicular case. For the extreme WSs instead, there is a long-shore decay only for the oblique WSs.

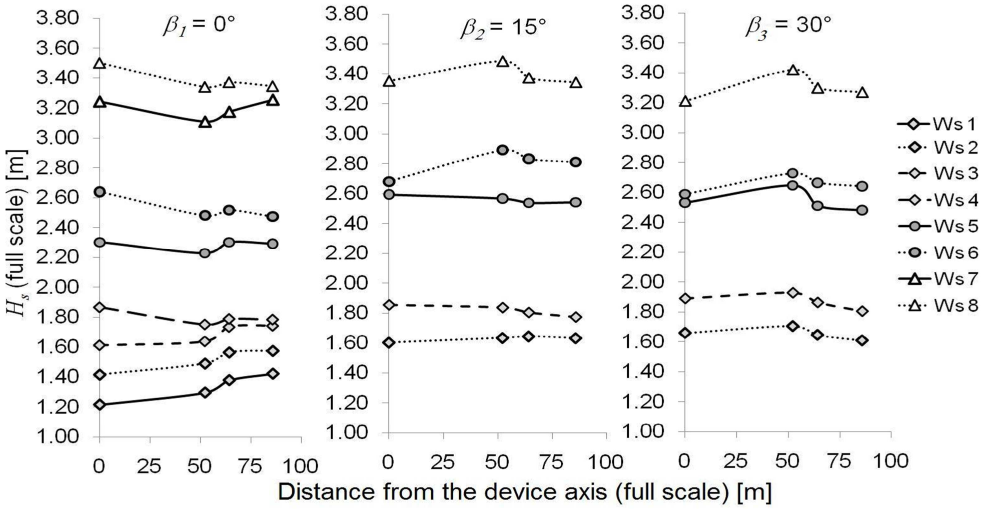

***Figure 7.10** – Wake effects behind the second line of the wave farm for the ordinary WSs with h_2. Values of H_S (full scale) are derived from the WGs 22, 25, 26, 27.*

7.3. RESULTS IN SCALE 1:30

For the configuration in 1:30 scale, both the hydrodynamic and power data were elaborated. Therefore, in this section, the data have been divided in topics.

7.3.1. HYDRODYNAMIC RESULTS

Following the procedure of the 1:60 data, the hydrodynamic data were elaborated in the time and frequency domains.

In table 7.7 the K_T and K_R induced by the single device are provided based on equations (1) and (2). H_I and H_R are derived from the BDM analysis of the front 5WGs array for spread and CALM system. H_T is derived from the back 5WGs array in case of spread mooring whereas for the CALM system it is derived from the 3 WGs back Array.

β_1=0°			β_2=15°			β_3=30°		
WS	K_T	K_R	**WS**	K_T	K_R	**WS**	K_T	K_R
Spread mooring system								
1	0.81	0.32	**1**	0.87	0.31	**1**	0.94	0.33
2	0.84	0.27	**2**	0.88	0.26	**2**	0.94	0.27
3	0.80	0.26	**3**			**3**		
4	0.82	0.26	**4**	0.87	0.27	**4**	0.94	0.26
5	0.85	0.20	**5**	0.83	0.20	**5**	0.87	0.21
6	0.82	0.28	**6**			**6**		
7	0.84	0.20	**7**	0.82	0.20	**7**	0.89	0.20
8	0.83	0.23	**8**	0.84	0.24	**8**	0.87	0.17
9	0.86	0.20	**9**			**9**		
10	0.82	0.24	**10**	0.84	0.24	**10**	0.87	0.20
CALM system								
1	0.69	0.24	**1**	0.86	0.25	**1**	0.91	0.26
2	0.75	0.23	**2**	0.85	0.23	**2**	0.84	0.23
3	0.68	0.23	**3**			**3**		
4	0.70	0.22	**4**	0.81	0.23	**4**	0.85	0.22
5	0.75	0.22	**5**	0.78	0.22	**5**	0.79	0.21
6	0.75	0.26	**6**			**6**		
7	0.74	0.22	**7**	0.79	0.21	**7**	0.79	0.20
8	0.75	0.24	**8**	0.74	0.21	**8**	0.73	0.19
9	0.75	0.22	**9**			**9**		
10	0.75	0.24	**10**	0.75	0.20	**10**	0.74	0.18

***Table 7.7** – Values of K_T and K_R for the model in 1:30 scale for the two mooring configurations.*

Figure 7.11 includes the trend of K_T for all the wave obliquity and mooring configurations.

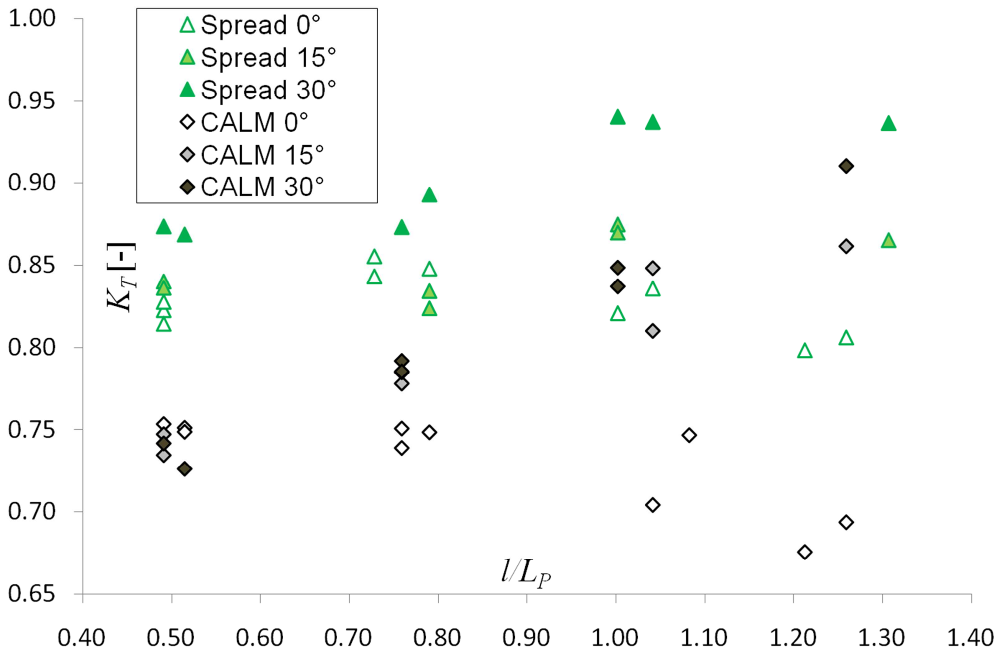

Figure 7.11 *– K_T against l/L_P for 1:30 model, for all β and mooring systems.*

For the spread mooring system, a great amount of the wave energy is transmitted behind the device, being K_T always in the range $0.80 < K_T < 0.94$. In addition, it can be observed that K_T increases with increasing β, and that differently from the small scale tests (related to K_{T1} and K_{T3}), it does not show a significant dependence on l/L_P.

The values of K_T are significantly lower with the CALM system than with the spread mooring. Lower K_T leads to a greater amount of available energy (at the PTO) thus to higher power performances (see next section). K_T data sets have different trends by increasing l/L_P; in particular, K_T increases in case of oblique WSs, whereas for perpendicular waves, K_T instead slowly decreases with increasing l/L_P. For long waves (i.e. $l/L_P<0.50$) K_T is not apparently affected by the obliquity, since all data provide mostly a same value.

Regardless the mooring typology –as for the 1:60 scale– the K_T does not depend on the wave steepness.

Based on the values reported in table 7.7, regardless the wave direction, K_R increases with increasing the dimensionless model length l/L_P, and decreases with a CALM mooring system.

For the data of the 1:30 configuration, a second analysis in the frequency domain was performed using the WGs placed in the two WG-castles, which were always aligned with the device axis (only for the spread mooring system), i.e. the analysis of the change of the main incident wave direction, $\Delta\theta$. $\Delta\theta$ was derived as the difference between the incident wave direction at the WG-castle in front of the device θ_I, and the incident transmitted wave direction at the WG-castle behind it, θ_T. The incident wave directions were derived through the BDM method, and an example of the results of this analysis is the 3D rose spectrum, reported in figure 7.12 for the WS n.10, perpendicular wave attack, and a device orientation of 30° with respect to the incident wave direction. Table 7.8 includes the results of θ_I, θ_T and $\Delta\theta$ for all the tests performed with the spread mooring system.

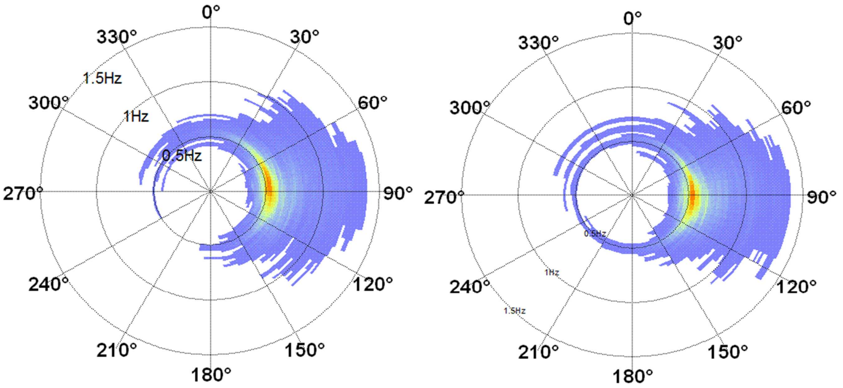

***Figure 7.12** – Incident (left) and transmitted (right) directional spectra for the WS n. 10 with 30° oblique waves.*

WS	$\beta_1=0°$			$\beta_2=15°$			$\beta_3=30°$		
	θ_I [°]	θ_T [°]	$\Delta\theta$ [°]	θ_I [°]	θ_T [°]	$\Delta\theta$ [°]	θ_I [°]	θ_T [°]	$\Delta\theta$ [°]
1	90.7	90.0	0.7	89.4	89.7	-0.3	89.5	85.2	4.3
2	92.6	89.7	2.9	91.3	90.6	0.7	89.6	84.6	5.0
3	90.9	89.6	1.3						
4	90.8	89.0	1.8	90.7	90.0	0.7	89.1	85.3	3.8
5	91.0	89.3	1.7	90.5	92.8	-2.3	90.1	89.0	1.1
6	88.6	89.2	-0.6						
7	89.5	90.9	-1.4	88.0	91.6	-3.6	90.3	88.6	1.7
8	91.9	90.7	1.2	89.8	92.3	-2.5	85.6	90.2	-4.6
9	90.9	90.8	0.1						
10	91.4	90.8	0.6	90.3	93.6	-3.3	85.3	91.0	-5.7

***Table 7.8** – θ_I, θ_T and $\Delta\theta$ for different obliquities (with β_1 the wave propagated perpendicular to the beach and parallel to the device axis).*

Figure 7.13 graphically reports $\Delta\theta$ as function of l/L_P. The maximum value of $\Delta\theta$ is around 6° when l/L_P=0.40. The difference in $\Delta\theta$ decreases with increasing l/L_P. When l/L_P is around or greater than 1.00, $\Delta\theta$ has the same sign for all the device obliquities.

Furthermore, the maximum value of $\Delta\theta$ corresponds to the configuration where K_T was maximum and to the greater difference device axis-wave direction (β_3=30°), which can be justified by the greater device motion and consequent delay in its re-orientation back to the initial position. Therefore to minimise the changes in sediment transport due to variation of the incoming wave direction it is suggested a configuration where the device is aligned with the main incident wave direction.

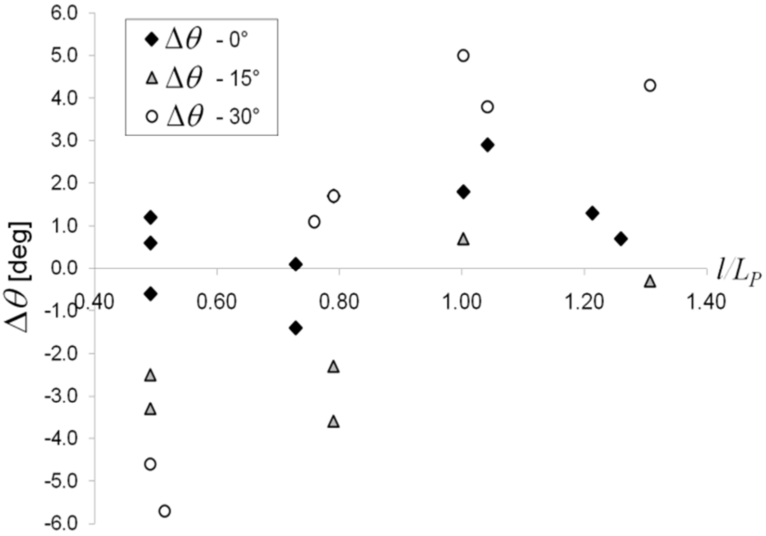

Figure 7.13 *– Variation of wave directions behind the model against l/L_P.*

In the time domain, the values of the significant wave height H_S, has been derived through the zero-down-crossing procedure for every WG. The results of this elaboration are reported in tables 7.9 and 7.10, for the two mooring systems.

As done for the small scale configuration, a last analysis was carried out in order to better investigate the wave energy behind the device, i.e. the wake effects behind the device, performed through the WGs n. 7, 8, 14 and 16 for the spread mooring system. The H_S recorded at these WGs were plotted against the distance from model axis, for each WS and for each obliquity (see Fig 7.14).

For the first four WSs, since the model motion is modest, the highest values of H_S are found at the farthest point of the wake. For oblique waves, the model tends to re-orient itself aligning its axis along the incoming wave, leading to higher values of H_S at WGs nr. 7 and 14.

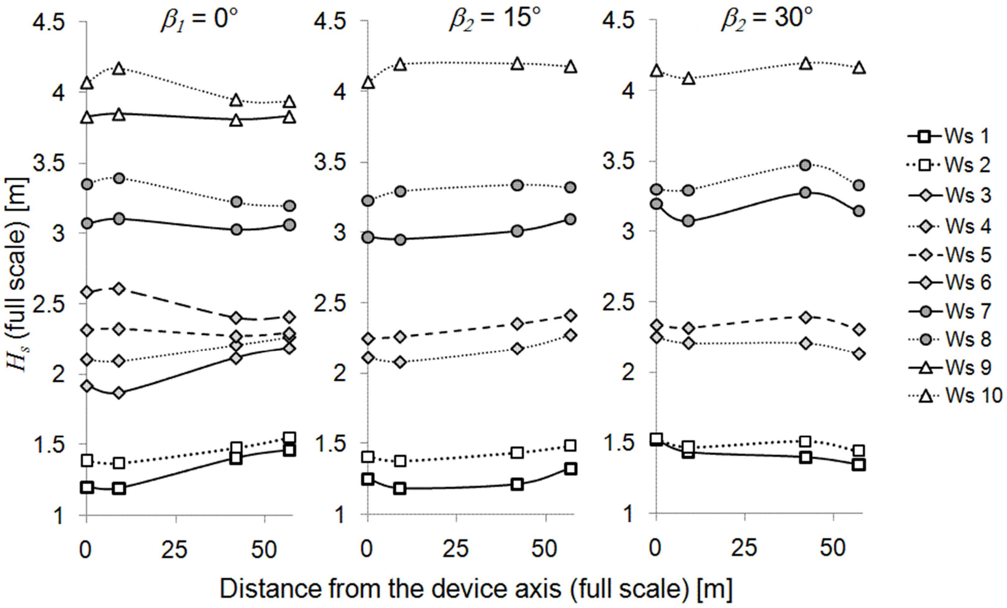

***Figure 7.14** – Wake effects behind the 1:30 scale model with the spread mooring system.*

WSs		**Nr. of WG**															
		1	**2**	**3**	**4**	**5**	**6**	**7**	**8**	**9**	**10**	**11**	**12**	**13**	**14**	**15**	**16**
β_1	**1**	1.52	1.60	1.53	1.55	1.56	1.19	1.19	1.20	1.26	1.19	1.58	1.71	1.56	1.40	1.51	1.46
	2	1.62	1.69	1.71	1.69	1.69	1.40	1.37	1.39	1.44	1.36	1.70	1.78	1.64	1.48	1.61	1.55
	3	2.33	2.47	2.37	2.41	2.42	1.91	1.87	1.92	1.99	1.87	2.37	2.58	2.35	2.12	2.24	2.19
	4	2.49	2.56	2.64	2.56	2.62	2.07	2.09	2.10	2.17	2.03	2.56	2.64	2.45	2.21	2.42	2.26
	5	2.59	2.69	2.67	2.69	2.73	2.27	2.32	2.32	2.36	2.15	2.62	2.78	2.46	2.27	2.46	2.29
	6	3.08	3.11	3.10	3.04	3.14	2.61	2.60	2.58	2.56	2.42	2.76	2.85	2.53	2.40	2.61	2.41
	7	3.50	3.62	3.53	3.61	3.68	3.05	3.11	3.07	3.15	2.89	3.51	3.68	3.32	3.03	3.36	3.06
	8	3.98	4.15	4.04	4.05	4.06	3.47	3.39	3.35	3.34	3.22	3.74	3.82	3.35	3.22	3.41	3.20
	9	4.36	4.44	4.37	4.42	4.52	3.83	3.85	3.83	3.94	3.70	4.43	4.57	4.13	3.81	4.21	3.83
	10	4.99	5.08	5.01	4.94	5.04	4.17	4.17	4.07	4.06	3.84	4.68	4.75	4.22	3.95	4.28	3.93
β_2	**1**	1.52	1.59	1.50	1.53	1.59	1.34	1.18	1.25	1.21	1.40	1.59	1.63	1.48	1.21	1.47	1.32
	2	1.62	1.67	1.68	1.61	1.63	1.47	1.38	1.41	1.41	1.44	1.68	1.76	1.61	1.43	1.60	1.48
	4	2.47	2.54	2.60	2.52	2.56	2.18	2.08	2.11	2.13	2.13	2.50	2.64	2.44	2.18	2.42	2.27
	5	2.58	2.73	2.67	2.67	2.73	2.31	2.26	2.25	2.29	2.30	2.67	2.84	2.60	2.35	2.51	2.41
	7	3.48	3.68	3.62	3.70	3.74	3.02	2.95	2.97	2.98	3.02	3.57	3.75	3.40	3.01	3.34	3.09
	8	3.91	4.19	4.01	4.05	4.03	3.35	3.29	3.23	3.22	3.26	3.74	3.79	3.47	3.34	3.38	3.32
	10	4.93	5.09	4.98	5.01	5.06	4.22	4.19	4.07	4.04	4.07	4.64	4.73	4.29	4.20	4.24	4.18
β_3	**1**	1.65	1.66	1.62	1.65	1.71	1.60	1.43	1.52	1.45	1.60	1.74	1.79	1.54	1.39	1.61	1.34
	2	1.67	1.68	1.64	1.61	1.65	1.60	1.47	1.52	1.49	1.56	1.73	1.78	1.58	1.51	1.56	1.44
	4	2.52	2.48	2.49	2.44	2.47	2.36	2.21	2.25	2.21	2.30	2.59	2.66	2.34	2.21	2.33	2.13
	5	2.64	2.65	2.62	2.66	2.66	2.39	2.31	2.33	2.29	2.33	2.60	2.80	2.52	2.39	2.43	2.30
	7	3.51	3.57	3.47	3.55	3.56	3.26	3.08	3.20	3.13	3.26	3.49	3.71	3.34	3.27	3.20	3.14
	8	3.66	3.96	3.75	3.87	3.77	3.34	3.29	3.30	3.28	3.30	3.57	3.81	3.44	3.47	3.32	3.32
	10	4.52	5.02	4.79	5.00	4.79	4.18	4.09	4.14	4.10	4.14	4.46	4.77	4.20	4.19	4.23	4.16

***Table 7.9** – Values of H_S in full scale for the 1:30 model with spread mooring system.*

WSs		**Nr. of WG**															
		1	**2**	**3**	**4**	**5**	**6**	**7**	**8**	**9**	**10**	**11**	**12**	**13**	**14**	**15**	**16**
β_1	**1**	1.48	1.55	1.52	1.53	1.55	1.60	1.70	1.60	1.58	1.60	1.55	1.48	1.50	1.05	1.06	1.10
	2	1.59	1.66	1.65	1.66	1.69	1.69	1.79	1.65	1.66	1.65	1.63	1.57	1.58	1.27	1.26	1.29
	3	2.26	2.42	2.38	2.38	2.42	2.38	2.50	2.34	2.34	2.39	2.26	2.26	2.23	1.59	1.61	1.68
	4	2.48	2.54	2.56	2.58	2.62	2.54	2.70	2.47	2.52	2.46	2.42	2.38	2.32	1.84	1.84	1.90
	5	2.65	2.75	2.83	2.78	2.83	2.58	2.75	2.46	2.50	2.47	2.42	2.36	2.37	2.08	2.10	2.12
	6	3.07	3.22	3.20	3.13	3.14	2.69	2.87	2.61	2.55	2.51	2.50	2.35	2.36	2.42	2.43	2.49
	7	3.59	3.68	3.71	3.62	3.77	3.45	3.66	3.35	3.32	3.29	3.22	3.11	3.11	2.75	2.79	2.86
	8	3.98	4.25	4.15	4.07	4.08	3.60	3.75	3.48	3.43	3.37	3.32	3.15	3.19	3.15	3.17	3.26
	9	4.44	4.56	4.60	4.57	4.67	4.28	4.56	4.19	4.20	4.17	4.10	3.92	3.91	3.46	3.49	3.62
	10	4.99	5.13	5.09	4.97	5.03	4.46	4.68	4.33	4.31	4.22	4.19	3.92	4.00	3.94	3.97	4.11
β_2	**1**	1.48	1.61	1.55	1.58	1.54	1.63	1.75	1.59	1.72	1.61	1.63	1.62	1.61	1.34	1.33	1.35
	2	1.57	1.69	1.59	1.64	1.67	1.69	1.85	1.66	1.73	1.62	1.58	1.60	1.61	1.41	1.41	1.40
	4	2.48	2.51	2.44	2.47	2.57	2.52	2.75	2.47	2.58	2.44	2.39	2.41	2.43	2.07	2.04	2.06
	5	2.62	2.79	2.73	2.71	2.77	2.71	2.80	2.49	2.66	2.48	2.47	2.53	2.54	2.17	2.14	2.16
	7	3.52	3.66	3.62	3.58	3.71	3.61	3.76	3.38	3.59	3.32	3.28	3.37	3.46	2.92	2.88	2.91
	8	4.06	3.95	3.98	3.83	4.05	3.68	3.93	3.58	3.70	3.52	3.38	3.50	3.48	3.04	3.02	3.06
	10	4.96	4.85	4.83	4.66	4.95	4.59	4.88	4.43	4.67	4.38	4.26	4.42	4.43	3.74	3.73	3.77
β_3	**1**	1.47	1.72	1.62	1.62	1.59	1.62	1.77	1.63	1.70	1.64	1.55	1.47	1.44	1.51	1.51	1.47
	2	1.58	1.77	1.67	1.70	1.67	1.67	1.83	1.65	1.69	1.66	1.56	1.53	1.47	1.45	1.43	1.40
	4	2.39	2.67	2.44	2.54	2.48	2.55	2.71	2.51	2.63	2.47	2.37	2.16	2.11	2.23	2.22	2.15
	5	2.56	2.79	2.69	2.69	2.74	2.70	2.84	2.55	2.60	2.45	2.34	2.28	2.23	2.23	2.21	2.19
	7	3.51	3.82	3.68	3.63	3.72	3.63	3.76	3.48	3.58	3.32	3.20	3.01	2.96	3.04	3.03	2.96
	8	3.93	3.83	3.83	3.70	3.94	3.68	3.91	3.57	3.60	3.56	3.38	3.30	3.18	2.97	2.96	2.94
	10	4.82	4.90	4.74	4.64	4.79	4.75	4.92	4.46	4.43	4.42	4.23	4.01	3.87	3.76	3.74	3.70

***Table 7.10** – Values of H_S in full scale for the 1:30 model with CALM system.*

7.3.2. POWER PERFORMANCE

From the force transducer (equipped bone) and the ultrasonic displacement sensor placed on board of the model, it was possible to evaluate its power performance. In particular the instantaneous values of the produced power were estimated by multiplying forces and velocities.

The power performance is in function of the PTO rigidity, therefore an assessment of the optimization of the PTO rigidity was performed under 10 equivalent regular waves (RW), before starting the tests with the irregular WSs. A total of 17 rigidities were available on the PTO system (10 of them used with the spread mooring system, and 5 of them with the CALM).

Figures 7.15 and 7.16 represent the efficiency η, derived as the ratio between the mean power production P_{PTO} and the available wave power P_W, by varying the PTO rigidity for each equivalent RW, for the spread and CALM mooring system respectively. The wave power has been derived as:

$$P_W = \rho \cdot g^2 \cdot \frac{H_S^2 \cdot T_p}{64 \cdot \pi} \qquad (3)$$

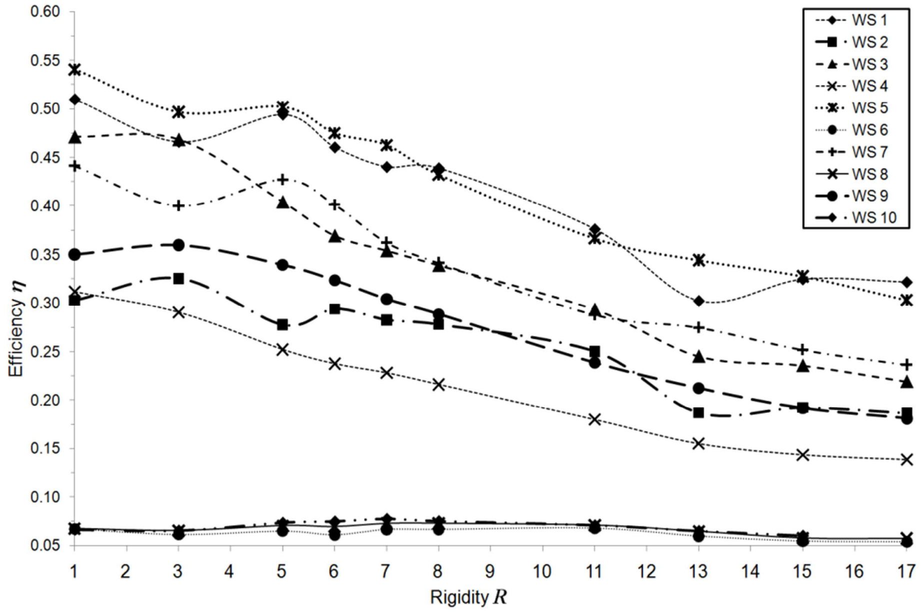

Figure 7.15 *– Efficiency against PTO rigidity for 1:30 scale model, with the spread mooring.*

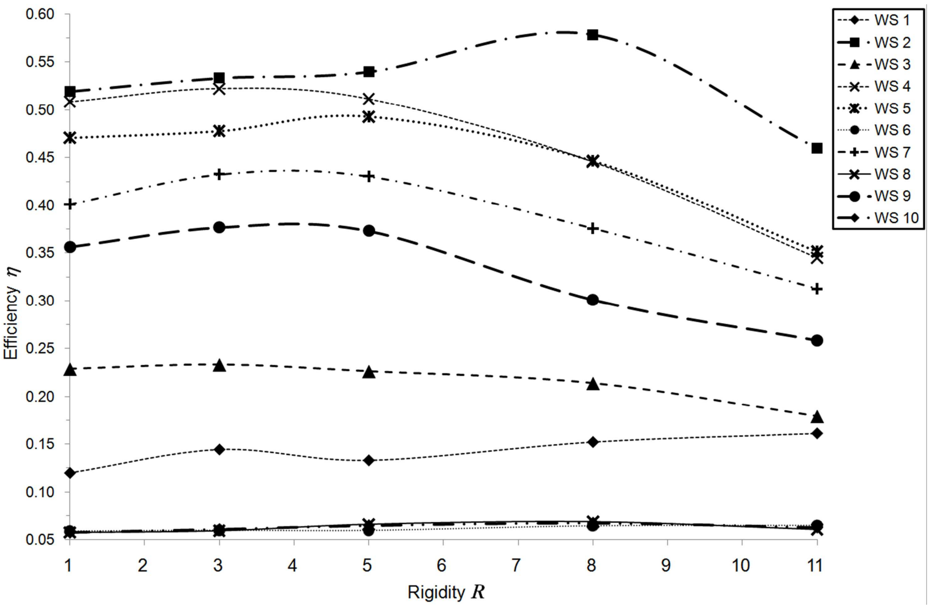

Figure 7.16 *– Efficiency against PTO rigidity for 1:30 scale model, with the CALM mooring.*

Analysing the trend of η and of P_{PTO}, the rigidity R=5 was selected has optimal compromise for both the mooring system. Further details on the equivalent RW and on the power produced under these RW are available in the Internal Deliverable ID 2.5 of the Theseus Project.

Once the best PTO rigidity has been assessed, it has than keep constant during the tests performed under irregular waves.

The results of η, P_{PTO} and P_W obtained under irregular waves are summarised in the table 7.11.

β_1				β_2				β_3			
WS	P_w [W]	P_m [W]	η [-]	**WS**	P_w [W]	P_m [W]	η [-]	**WS**	P_w [W]	P_m [W]	η [-]
Spread mooring system											
1	1.35	0.23	0.21	**1**	1.30	0.21	0.20	**1**	1.58	0.21	0.16
2	1.88	0.35	0.23	**2**	1.85	0.34	0.23	**2**	1.87	0.30	0.20
3	3.34	0.61	0.23	**3**				**3**			
4	4.50	0.84	0.23	**4**	4.26	0.85	0.25	**4**	4.05	0.83	0.26
5	6.06	0.98	0.20	**5**	6.39	0.96	0.19	**5**	6.06	0.87	0.18
6	10.33	0.59	0.07	**6**				**6**			
7	11.14	1.55	0.17	**7**	11.19	1.60	0.18	**7**	10.92	1.62	0.19
8	18.44	1.01	0.07	**8**	17.21	0.98	0.07	**8**	16.11	1.01	0.08
9	16.47	2.35	0.18	**9**				**9**			
10	27.59	1.51	0.07	**10**	27.20	1.50	0.07	**10**	25.19	1.56	0.08
CALM system											
1	1.34	0.27	0.25	**1**	1.39	0.25	0.22	**1**	1.50	0.26	0.22
2	1.83	0.39	0.26	**2**	1.80	0.39	0.27	**2**	1.91	0.29	0.19
3	3.31	0.71	0.27	**3**				**3**			
4	4.43	0.98	0.28	**4**	4.24	0.94	0.28	**4**	4.28	0.74	0.22
5	6.39	1.11	0.22	**5**	6.35	1.04	0.20	**5**	6.21	0.79	0.16
6	10.51	0.75	0.09	**6**				**6**			
7	11.51	2.10	0.23	**7**	11.01	1.67	0.19	**7**	11.57	1.38	0.15
8	18.24	1.42	0.10	**8**	17.16	1.09	0.08	**8**	16.48	0.81	0.06
9	17.88	2.79	0.20	**9**				**9**			
10	27.74	1.69	0.08	**10**	25.98	1.61	0.08	**10**	25.19	1.25	0.06

Table 7.11 *– P_{PTO}, P_W and η for all the wave obliquities and for the two mooring systems*

The data reported in the table showed that P_{PTO} and η in case of CALM system are significantly greater than in case of spread mooring, with the exception of wave attacks characterised by greater obliquity (β_3), where the spread mooring system seems to be more effective. Furthermore, P_{PTO} show their maxima when l/L_P is around 0.73 for orthogonal waves and 0.76 for oblique attacks, whereas η show well marked peaks when $1.0< l/L_P <1.2$ and more precisely, their maxima occur when l/L_P is around 1.05. For an easier comprehension, figure 7.17 show the trend of η against l/L_P, from which it is possible to assess that the mooring system is not a negligible aspect for the device power production.

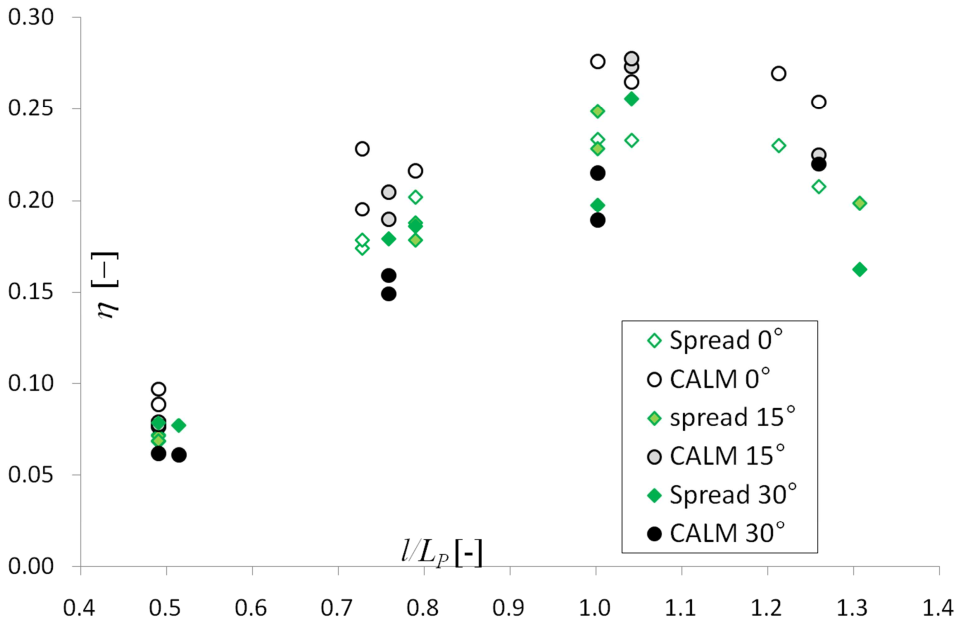

Figure 7.17 *– Trend of η against l/L_P by varying the mooring system, for all the wave obliquities.*

7.4. DISCUSSION

7.4.1. MOORING EFFECTS

For the two mooring typologies a comparison between η and K_T was appointed and reported in figure 7.18. This assessment should allow to evaluate the optimal ranges of l/L_P in which both the energy production and coastal protection may be maximised.

In figure 7.18 the sets of η and of K_T, together with their second order tendency curves, are plotted and compared. The curve coefficients are computed by means of the ordinary least squares method.

In case of perpendicular waves K_T decreases with increasing l/L_P, whereas under oblique waves it linearly increases. In all tested conditions, η has a peak around l/L_P=1, then it tends to decrease more markedly for oblique waves.

Since it is not possible to define a combine optimal range for β_2 and β_3 (due to the monotonic increase of K_T with increasing l/L_P) a reasonable choice is define the optimal value $l/L_P \approx 1.00$, based on the results for β_1.

Furthermore, the CALM system can provide better results in terms of coastal protection and energy production compared to the spread system, being closer the curves related to K_T and η (i.e. lower wave transmission, higher efficiency).

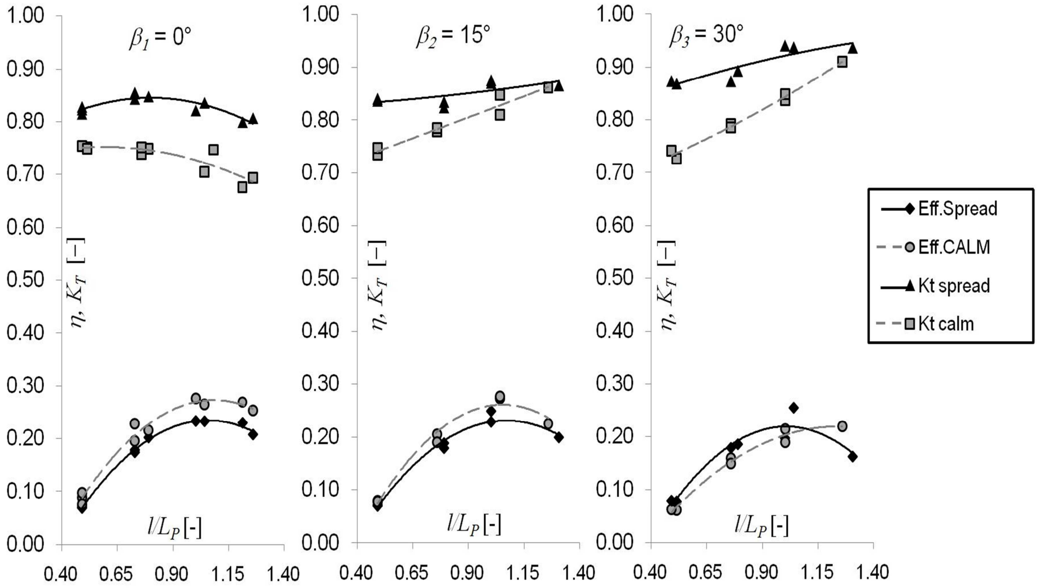

***Figure 7.18** – Comparison among η and K_T curves for the two mooring typologies and for different obliquities.*

7.4.2. SCALE EFFECT

The values of K_T from tests in 1:60, named $K_{T,1:60}$ hereafter, and from tests in 1:30 scales, similarly named $K_{T,1:30}$, were compared. The values of $K_{T,1:60}$ correspond to K_{T1}, being the transmission coefficient referred to a single device within the farm. The compared results are the ones derived for ordinary WSs for water depth h_1 in 1:60 scale and correspond to the WSs from the 3rd to the 10th in 1:30 scale (see Fig. 7.19).

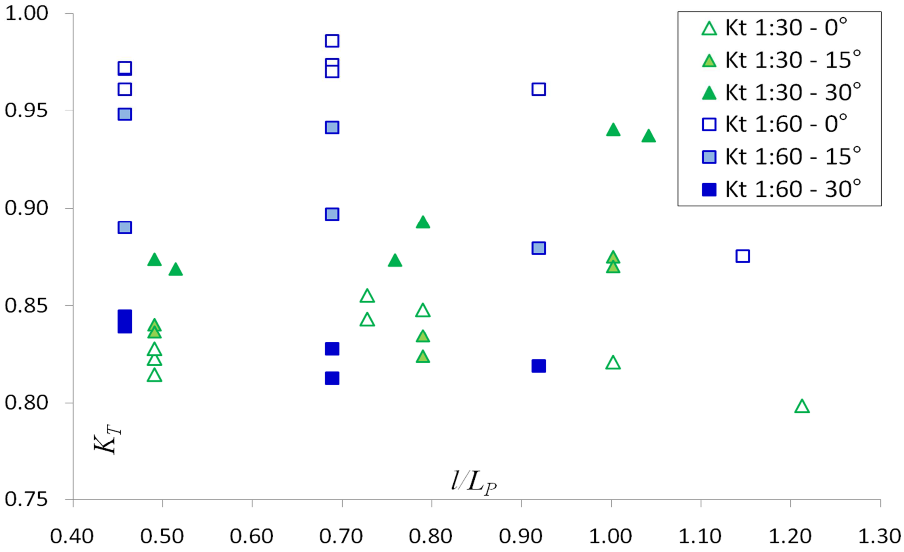

***Figure 7.19** – Comparison among K_T values at different scales.*

It can be noticed that:

- $K_{T,1:60}(\beta_1)$ is always higher than $K_{T,1:30}(\beta_1)$, although their trends are quite similar: they increase with increasing l/L_P, up to reach their maxima when l/L_P=0.72 ($K_{T,1:60}$=0.99 and $K_{T,1:30}$=0.86), then they decrease. $K_{T,1:60}$ seems to be simply shifted upwards compared to $K_{T,1:30}$
- for oblique waves, in case of β_2=15°, $K_{T,1:60}$ decreases with increasing l/L_P, whereas $K_{T,1:30}$ has a totally opposite tendency. In case of β_3=30°, both $K_{T,1:60}$ and $K_{T,1:30}$ increase with increasing l/L_P, although with different rates ($K_{T,1:60}$ grows slower).

The differences among sets of K_T in figure 7.19 may be explained through the parameter c_I and c_T, defined as the ratios between H_I and H_T for 1:30 and 1:60:

$$c_I = \frac{[H_I]_{1:30}}{[H_I]_{1:60}} \tag{4}$$

$$c_T = \frac{[H_T]_{1:30}}{[H_T]_{1:60}} \tag{5}$$

The values of c_I, c_T and c_R (i.e. the ratios between H_R at the two scales) are included in table 7.12.

	β_1			β_2			β_3		
WS	c_I	c_T	c_R	c_I	c_T	c_R	c_I	c_T	c_R
1	1.26	1.15	1.18						
2	1.36	1.16	1.48	1.21	1.25	0.82	1.21	1.39	1.31
3	1.31	1.15	1.34	1.31	1.18	0.81	1.26	1.32	1.19
4	1.35	1.14	2.24						
5	1.33	1.14	1.45	1.26	1.18	0.81	1.27	1.39	1.14
6	1.34	1.22	1.93	1.39	1.26	1.34	1.25	1.37	0.96
7	1.30	1.13	1.36						
8	1.33	1.13	2.06	1.35	1.33	1.39	1.32	1.38	1.15

***Table 7.12** – Ratio of H_I, H_T and H_R derived from tests at different scales.*

The K_T differences are essentially due to differences among c_I and c_T for each WS (c_I is always greater than c_T for β_1 and β_2, whereas $c_I < c_T$ for β_3). The variation between H_I and H_T in the two scales for the same test may be explained with several reasons, for example by the wave-maker typical range of wave generation (particularly water depth) and by the inertia of the two models.

The model inertia affects the device mobility and therefore its capability to re-orient itself, especially under oblique wave attacks (when the device motions are larger, aspect quantitatively confirmed with the second experimental investigation). The device weights for 1:30 and 1:60 scale tests were not perfectly scaled, as well as the weight per unit length of the mooring chains. In full scale, the 1:30 model is heavier than the small one: the total weight (device + mooring) in static conditions is $1.00 \cdot 10^6$ kg whereas for the small model it is $0.85 \cdot 10^6$ kg. The lighter the system (device + mooring) the faster the device motions, therefore a greater amount of wave motion is transmitted. For orthogonal waves instead, since the model does not move a lot, the inertia influence on the device mobility and consequently on wave transmission is less marked. Therefore, a heavier system leads to better wave reduction results keeping constant the other design parameters, such as mooring system, device geometry, etc.

Even comparing the values of K_R from tests in 1:60 and 1:30 scales, it is possible to note differences, which are however small compared to K_T in the two scales. For β_1, c_R is always higher than 1.00 (hence H_R is greater for the big model than for the small one) and it is also higher than c_I, leading to higher values of $K_{R,1:30}$ compared to the values of $K_{R,1:60}$.

7.5. PRELIMINARY CONCLUSIONS

7.5.1. ASSESSMENT OF THE INVESTIGATION

The experimental activity confirmed the importance of the device design based on the wave climate (i.e. the importance of the parameter l/L_P, which should be around 1) already found in preliminary tests carried out with the 1:30 scale (Zanuttigh et al., 2010). This parameter in fact effects the wave transmission and the device power production.

However the wave transmission is always high (greater than 0.75), therefore the examined module should be repeated along the cross-shore and long-shore directions. For instance, by repeating two times this module, the mean transmission coefficient $K_{T,m}$ can be roughly calculated as K_{T2}^2 in case of aligned farm lines and as K_{T4}^2 in case of staggered farm lines. The resulting wave transmission coefficients for these theoretical installations are reported in table 7.13 by increasing the number of lines.

	ALIGNED FARM LINES									
	h_1					h_2				
n. lines	**1**	**2**	**4**	**8**	**16**	**1**	**2**	**4**	**8**	**16**
β_1	0.98	0.97	0.94	0.88	0.77	0.98	0.95	0.90	0.82	0.67
β_2	0.97	0.93	0.87	0.75	0.57	0.97	0.94	0.88	0.77	0.60
β_3	0.93	0.87	0.76	0.57	0.33	0.93	0.87	0.76	0.58	0.33
	STAGGERED FARM LINES									
	h_1					h_2				
n. lines	**1**	**2**	**4**	**8**	**16**	**1**	**2**	**4**	**8**	**16**
β_1	0.97	0.94	0.88	0.77	0.60	0.97	0.93	0.87	0.75	0.57
β_2	0.96	0.91	0.83	0.69	0.48	0.96	0.92	0.85	0.72	0.51
β_3	0.93	0.86	0.74	0.55	0.31	0.93	0.86	0.75	0.56	0.31

***Table 7.13** – Hypothetical mean values of K_T in case of multiple lines based on a linear superposition assumption.*

Furthermore the mooring typology is an other relevant parameter for the device design. A CALM mooring configuration should lead to lower wave transmission and also higher power production than a spread mooring. The spread system can be optimised by changing its pre-tension and/or the chains length and so the log-shore gap width between devices in a same line.

A reduction of the log-shore gap width could leads to benefits from the interaction between the devices (i.e. destructive wave interaction with consequent reduction of the wave height in the gap). Visual observations of the first line models, under testing, suggested that maximum device displacements along y axis were not greater than 0.5*b* (on both sides), therefore the safe distance to be kept among the devices is around 3*b*. If such distance is adopted as the gap width –assuring that there are no problems for the correct functioning of the mooring systems– the effects due to the superposition of the device wakes can provide a greater reduction behind them. This phenomenon is surely useful for coastal protection purposes, but reduces at the same time the energy incident the rear device.

Finally, the water depth at installation does not significantly affect the results, leading to the conclusion that a farm of these devices would not be particularly sensitive to sea level rise induced by climate changes. It is also suggested to limit the wave angle between the farm and the main incoming wave direction up to 30°.

7.5.2. WHAT IS MISSING

The main target of the first experimental activity was focused on the investigation of the hydrodynamic interactions among devices in a module of a wave farm. Since these devices did not carry out a PTO system on board, the same device was also investigated in a bigger scale. With this second configuration it was possible to assess effects due to the laboratory scale and to the mooring typology.

However it was overlooked, and so not completely investigated aspects such as the mutual distance between the devices, wake effects (especially in long-shore direction), forces acting on the mooring lines and effects due to the presence of a more realist PTO in a farm configuration and due to different mooring pre-tension levels. Therefore a second experimental investigation was believed essential.

8. SECOND INVESTIGATION

The second experimental investigation was performed –as before– at Aalborg University, but in a different wave basin. Changing the basin entails to different reliable basin space, installation water depths and furthermore the devices were not available at the moment of the second investigation and so they were re-built following the same geometry adopted before.
It is worthy to remark that the basin depth affects the combination of the maximum feasible water depths and wave heights to be tested (i.e. the future place of installation). Furthermore the decision of the scale also affects the device behaviour, because some effects are not easily reproducible (for example friction effect, PTO system, mooring force). For the purpose of the tests, a scale of 1:60 was considered an adequate compromise.

The models were re-built based on Froude similitude, and were design to carry on board a more stable PTO system and measurements on the mooring lines, thus it has been possible to combine all the results.

8.1. LABORATORY SET-UP

The tests were performed in the directional wave basin (commonly called the shallow basin) 12.0 m long, 17.8 m wide, and 1.0 m deep. The waves are generated through a snake-front piston type paddle system with 25 actuators. A dissipative beach made of concrete and gravel with D_{50}=2 cm is placed opposite to the wave maker, whereas the sidewalls are made of crates full filled with stones (1.2x1.2 m, 0.70 m high).

According to the chosen 1:60 scale and following the device typical dimensions for the North Sea conditions, the model was 0.95m long (*l*) and 0.38m wide (*b*) perpendicularly to the direction of wave propagation. As the prototype, the laboratory model was composed by two parts, each consisting of three cylindrical floaters and two legs (see Fig.s 8.1 and 8.2). A rigid hinge was placed between the pontoons in order to connect them. In particular, the laboratory model was around 4kg, and was made of PVC pipes and polystyrene for the front floater.

Two similar devices were built and deployed in the basin. The two models were placed at the same distance from the wave-maker (3.60 m) in order to represent a wave farm module line (see Fig. 8.1). Their mutual long-shore distance was changed from the minimum value to let the moored devices free to move (i.e. 2.00 m, equals to 5*b*) to a maximum distance accounting for the optimisation of the marine space and the basin size (i.e. 3.10m, equals to 8*b*).

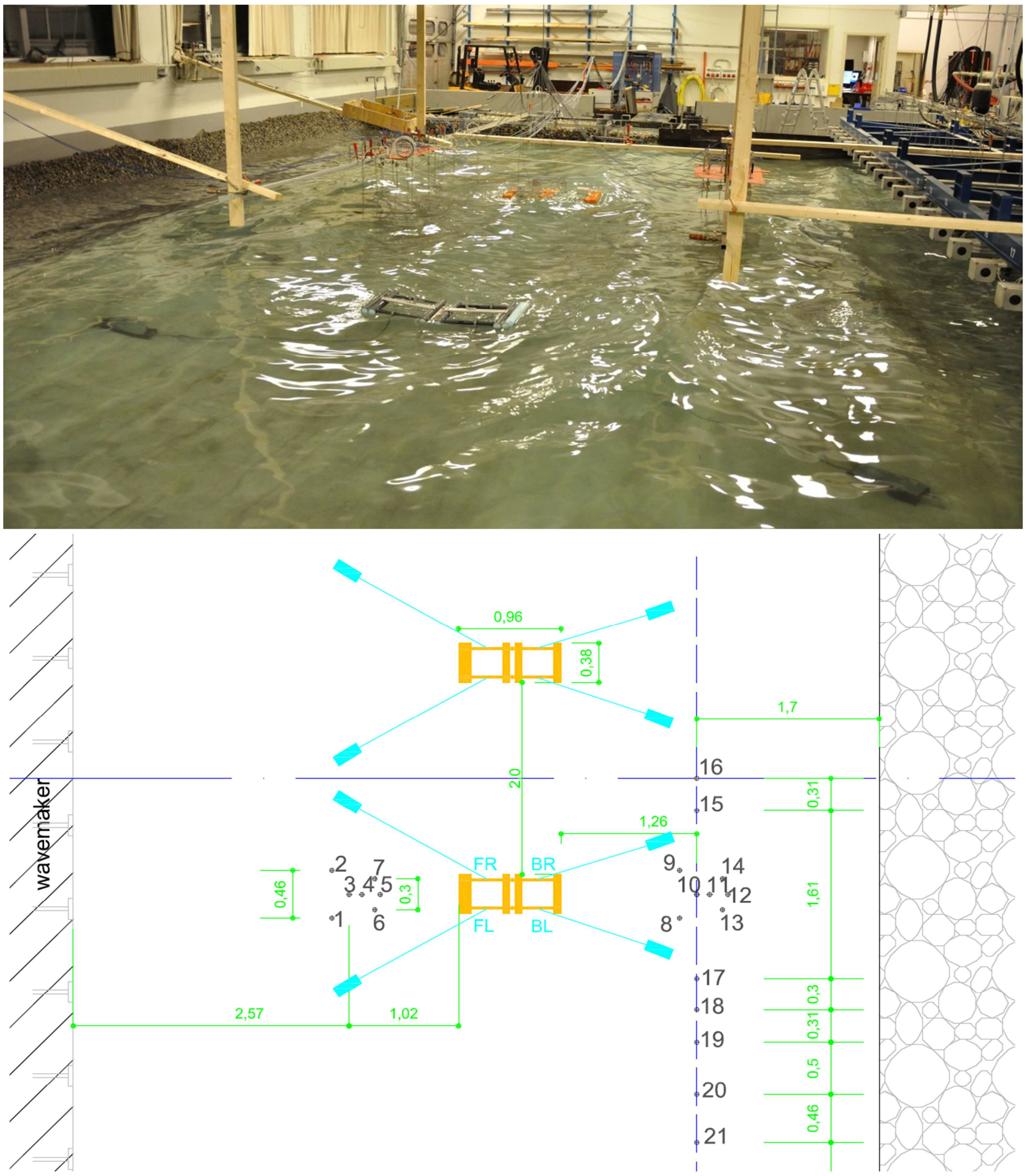

***Figure 8.1** – Devices at a long-shore distance equal to 5b, where b is the device width. On the top: picture of the laboratory configuration (incident waves come from right side); on the bottom: scheme of the wave farm line in scale 1:60 (incident waves come from left side). The distances are in meter.*

Both models carried the Power Take-Off (PTO) system on board, but in only one model –the top one in figure 8.2– the PTO system was instrumented. The PTO system was placed over the device hinge (at the middle of the device) at a known vertical distance from the model axis, and it was aligned with the device cross-shore axis. It was composed by an air piston and a displacement sensor both placed in a horizontal position (see Fig. 8.2). The PTO system is connected to the device through two rigid aluminium L-shape beams, and its end-stops limit the stroke to 0.10 m. The PTO rigidity was modified by varying its vertical distance from the model axis; a maximum of 6 rigidities were analysed. Further details are provided in the Results Section related to the Power production (section 8.2.2).

***Figure 8.2** – Models of the Wave Activated Bodies with spread mooring system, in scale 1:60.*
Top: Model with the PTO connected to the acquisition box.
Bottom: Model with the PTO not connected to the acquisition box.

The models were moored with a “spread” mooring system (Harris et al., 2004), with four steel chains (weight per length unit 0.1kg/m). The front chains were 2.50m long, whereas the back chains were 1.75m long. This specific asymmetric mooring configuration was selected in order to assure device keeping in sway direction (which was visually observed to be a relevant motion during the first experimental investigation) and to minimise the cost. Each chain was linked to the device at the fairlead point and fixed to the bottom with heavy anchors (3kg each). The position of the fairleads was taken approximately in correspondence of the centre of mass of

each pontoon. For the instrumented device, each chain was directly connected to a single in-line load-cell.
The initial pre-tension level of the chains was changed to evaluate the effect of the mooring system on the power production. In particular the length of the chain lying on the seabed (L_C) was progressively reduced from an initial condition equal to the 80% of the total chain length on the seabed (corresponding to an average pre-tension of 0.6 N), to the 65% (pre-tension of about 0.98 N) and finally to the 50% (with a pre-tension greater than 1.6 N). The evaluation of the best mooring pre-tension level, for power production purposes, was performed under perpendicular waves both under regular and irregular wave conditions.

To achieve the target of the experiments, different kind of measurements were required; in particular: load cells for the forces acting on the mooring lines, Motion Trackers for the device motions in the 6 canonical Degree of Freedom (DoF), a PTO system and WGs for the hydrodynamics around the devices.

To measure the forces acting on moorings, a set of 4 FUTEK load cells with a maximum load around 40 kg was used. Each load cell was placed between the device and one mooring chain (see Fig. 8.2). The load cell signal was low pass filtered, with cut-off frequency of 10 Hz. To increase the signal resolution in the working range, twenty-fold amplification was applied to the signal in order to fit the expected maximum load.

The motions of the device were measured by means of a miniature gyro-enhanced sensor, named Motion Tracker xsens (MTi). This instrument has an internal low-power signal processor to provide 3D attitude angles (roll, pitch and yaw), 3D acceleration (in surge, sway and heave direction), 3D rate of turn (rate gyro) and 3D earth-magnetic field data. Two MTi were deployed in a single device, one for each pontoon (see Fig. 8.2, top).

To identify the PTO system performance it is necessary to measure the forces induce by the device motions on the PTO system and its motions. The forces were measured through a particular load cell with a maximum load around 100 kg, placed at the extremity of an air piston. The load cell was calibrated and properly amplified in order to operate in a range of 20 N. Whereas to record the PTO motion, a displacement sensor was secured to the air piston (see Fig 8.2, top).

Resistive Wave Gauges (WGs) were deployed in the basin in order to evaluate the hydrodynamic field around the devices. During the sampling, each WG registers the instantaneous value of the local water elevation. In total, a value of 21 WGs was used (see Fig. 8.1), for each gap width configuration. In particular, the incident wave field was evaluated by means of the first 7 WGs (i.e. n. 1 to 7) located between one device and the wave-maker (at a mean distance of 0.90m from the extreme of the front cylinder of the ahead pontoon). WGs n. 8 to 14 were deployed in an array behind the same device in correspondence to its cross-shore axis. The remaining WGs were placed behind the device (i.e. between the device and the beach) in a long-shore line at a distance of 1.26m from the extreme of the back cylinder of the rear pontoon (see Fig. 8.1).

Before the beginning of the experiments, all the load cells and displacement sensors were properly calibrated, whereas for other measurements, such as MTi and WGs, the calibration procedure was automatically repeated every day. Once the calibration procedure was concluded, the derived functions were introduced in the data acquisition software.
The calibration of the load cells was done by acquiring the value of the mean deformation, in Volt, correspondent to the application of numerous known masses. The calibration function depends on the amplification and/or of the filter coefficient. The series of coupled values of masses and mean Volts has been plotted and a nearly linear distribution Volt-Force was found for each load cell. The calibration of the displacement sensor was done following an analogous procedure, i.e. by measuring the relative voltage associated with known displacements (in meter).

The two models were subjected to several wave state characterised by similar wave height and period of the first investigation (ordinary conditions with wave height in the range 2-5m, wave period 5-11s, in full scale). Tests were performed with a water depth of 0.45m (27m in full scale), which also corresponds to the maximum water depth allowed in the basin.

Two main sets of Wave States (WSs) were chosen, the first set of 10 Regular Waves (RWs) used to determine the best PTO rigidity (see table 8.1), and the second set of 11 Irregular Waves (IRs). The RWs were selected to include similar ranges of wave height and wave period as for the IRs and by keeping constant the wave steepness. The duration of each RWs was about 5 minutes.

Regular wave condition for the PTO rigidity optimization				
H [m]	**T [s]**	**L_p [m]**	**l/L_p**	**s_{op}**
0.024	0.72	0.8	1.23	0.03
0.036	0.88	1.2	0.82	0.03
0.042	0.96	1.4	0.70	0.03
0.054	1.12	1.8	0.54	0.03
0.060	1.20	2.0	0.49	0.03
0.066	1.28	2.2	0.45	0.03
0.072	1.36	2.4	0.41	0.03
0.078	1.45	2.6	0.38	0.03
0.084	1.53	2.8	0.35	0.03
0.090	1.62	3.0	0.33	0.03

Table 8.1 *– Regular WSs used to evaluate the best PTO rigidity in 1:60 scale. H is the wave height, T is the wave period, L_P is the peak wave length, l/L_P is the ratio device–peak wave length and s_{op} is the wave steepness.*

Table 8.2 reports the irregular short-crested wave condition representative of the North Sea wave climate in laboratory scale. These WSs were obtained through a Jonswap spectrum (peak enhancement factor 3.3) with a spreading factor equal to 30 (leading to a spreading angle of 14.7°). The irregular WSs were selected to assess the combined performance of energy conversion, movements and moorings under typical operative and extreme conditions (based on return periods T_R=10, 50, 100 years). Some WSs were also repeated without the devices to better investigate the basin characteristics.

It is worthy to remark that the extreme WSs were performed only for the best mooring pre-tension level (i.e. L_C=80%, see the Section 8.2.2 related to the power production results for the choice of the optimal mooring pre-tension level), and some of them were repeated for the configuration with a wider gap width (i.e. WSs n. 7-10-11). Furthermore for the configuration with L_C=80% and with gap width equals to 8*b*, WSs n.1 and 2 were not performed.

Some irregular WSs were also repeated for oblique waves, i.e. with an incident wave direction of 10° and 20°. Oblique waves were obtained through the wave-maker, keeping constant the position of the device and of the measurement equipment.

All the irregular WS had a duration of 30 minutes each.

Ordinary waves					
WS	H_s [m]	T_p [s]	L_p [m]	l/L_p	s_{op}
1	0.033	0.72	0.81	1.21	0.041
2	0.033	0.90	1.24	0.79	0.027
3	0.050	0.96	1.39	0.70	0.036
4	0.050	1.08	1.70	0.58	0.030
5	0.067	1.27	2.17	0.45	0.031
6	0.083	1.45	2.61	0.38	0.032
Extreme waves					
7	0.133	1.69	3.18	0.31	0.042
8	0.133	1.81	3.45	0.28	0.039
9	0.143	1.69	3.18	0.31	0.045
10	0.150	1.78	3.38	0.29	0.044
11	0.167	1.87	3.59	0.27	0.047

***Table 8.2** – Irregular WSs used to evaluate the device performance in 1:60 scale. H_S is the significant wave height, T_P is the peak wave period, L_P is the peak wave length, l/L_P is the ratio device–peak wave length and s_{op} is the wave steepness.*

8.2. RESULTS

This section encloses all the main results divided into the following main topics: local hydrodynamic fields, PTO performance, loads acting on the mooring system and overall device motions for perpendicular and oblique WSs. It is worthy to remark that only few WSs (with L_C=80%) were repeated also for oblique waves, mainly due to wave-maker warning ("wave obliquity will result in a significant amount of energy redistributed to low frequencies due to spurious wave correction") and failure messages ("Biesel filter too low to accurately reproduce waves"). Table 8.3 summarises the WSs performed also for oblique waves.

WS	10°	15°	20°
1	-	-	-
2	x	-	x
3	x	-	x
4	x	x	x
5	x	x	x
6	x	x	x
7	x	-	x
8	x	-	x
9	x	-	x
10	x	-	x
11	x	-	x

***Table 8.3** – Irregular WSs performed under oblique waves with L_C=80%.*

8.2.1. HYDRODYNAMIC RESULTS

The data from the instantaneous elevation recorded at each WG were elaborated in the time and frequency domains. In particular, in the time domain a zero-down crossing procedure was applied in order to obtain the H_S and T_P at each WG, whereas in the frequency domain two main analysis were performed: one applied to three aligned WGs (WGs n. 3-4-5- and n. 10-11-12) in order to separate the incident from the reflected wave field in front and behind the device (by means of the Mansard and Funke's method, 1980), and a second analysis applied to the WGs castle in order to obtain directional wave spectrum by means of the Bayesian Directional Method (Hashimoto and Kobune, 1988).

In the time domain the zero-down crossing procedure was applied to set of different tests, by varying the pre-tension level L_C or the long-shore gap width. Results related to the narrow gap width and for the three mooring pre-tension levels L_C and to perpendicular WSs are reported in tables 8.4, 8.5 and 8.6.

	Ordinary Wave States						**Extreme Wave States**				
WG	**1**	**2**	**3**	**4**	**5**	**6**	**7**	**8**	**9**	**10**	**11**
1	0.032	0.038	0.056	0.058	0.068	0.085	0.113	0.119	0.125	0.129	0.140
2	0.031	0.039	0.057	0.061	0.068	0.083	0.109	0.123	0.132	0.131	0.140
3	0.032	0.040	0.058	0.062	0.069	0.085	0.112	0.126	0.133	0.129	0.140
4	0.030	0.039	0.055	0.061	0.066	0.082	0.109	0.128	0.131	0.127	0.138
5	0.031	0.038	0.056	0.058	0.067	0.082	0.110	0.125	0.128	0.127	0.138
6	0.032	0.038	0.054	0.058	0.065	0.081	0.110	0.127	0.129	0.126	0.138
7	0.032	0.037	0.057	0.057	0.069	0.085	0.108	0.120	0.124	0.130	0.139
8	0.026	0.035	0.051	0.062	0.066	0.082	0.115	0.122	0.131	0.127	0.144
9	0.027	0.035	0.049	0.060	0.065	0.079	0.117	0.123	0.128	0.125	0.141
10	0.026	0.034	0.049	0.062	0.062	0.078	0.115	0.126	0.131	0.124	0.140
11	0.026	0.032	0.048	0.058	0.061	0.078	0.114	0.124	0.128	0.123	0.136
12	0.027	0.035	0.050	0.062	0.065	0.079	0.118	0.129	0.133	0.127	0.138
13	0.027	0.035	0.052	0.063	0.066	0.084	0.122	0.130	0.135	0.134	0.146
14	0.030	0.033	0.052	0.057	0.067	0.083	0.127	0.127	0.129	0.136	0.147
15	0.031	0.035	0.050	0.055	0.070	0.081	0.117	0.122	0.122	0.127	0.144
16	0.031	0.042	0.050	0.062	0.071	0.084	0.111	0.119	0.121	0.123	0.140
17	0.030	0.038	0.055	0.058	0.066	0.082	0.112	0.123	0.133	0.127	0.142
18	0.030	0.036	0.054	0.056	0.066	0.079	0.106	0.124	0.135	0.125	0.138
19	0.033	0.038	0.056	0.057	0.071	0.081	0.110	0.122	0.131	0.128	0.141
20	0.032	0.041	0.052	0.059	0.068	0.078	0.107	0.127	0.132	0.125	0.138
21	0.030	0.037	0.052	0.056	0.068	0.076	0.105	0.120	0.125	0.122	0.136

Table 8.4 *– Values of H_S in meter in scale 1:60, for the tests with L_C=80% and gap width 5b, under irregular and perpendicular 3D wave attacks. First six WSs represent ordinary sea states, whereas the last five WSs represent extreme sea states.*

	Ordinary Wave States					
WG	**1**	**2**	**3**	**4**	**5**	**6**
1	0.036	0.039	0.054	0.055	0.071	0.087
2	0.043	0.039	0.060	0.055	0.076	0.092
3	0.037	0.041	0.059	0.056	0.077	0.094
4	0.036	0.040	0.058	0.054	0.076	0.094
5	0.035	0.039	0.057	0.056	0.074	0.092
6	0.038	0.040	0.057	0.055	0.074	0.092
7	0.035	0.038	0.055	0.056	0.071	0.088
8	0.031	0.035	0.054	0.054	0.069	0.083
9	0.030	0.036	0.054	0.053	0.067	0.085
10	0.029	0.035	0.052	0.051	0.067	0.084

Table 8.5 *– Values of H_S in meter in scale 1:60, for the tests with L_C=65% and gap width 5b, under irregular and perpendicular 3D wave attacks. First six WSs represent ordinary sea states, whereas the last five WSs represent extreme sea states. To be continued.*

	Ordinary Wave States					
WG	**1**	**2**	**3**	**4**	**5**	**6**
11	0.028	0.033	0.049	0.050	0.066	0.082
12	0.030	0.036	0.052	0.051	0.069	0.087
13	0.032	0.036	0.054	0.054	0.070	0.086
14	0.028	0.034	0.050	0.053	0.066	0.083
15	0.031	0.034	0.054	0.054	0.069	0.084
16	0.033	0.036	0.055	0.054	0.076	0.088
17	0.033	0.036	0.057	0.055	0.076	0.084
18	0.033	0.035	0.059	0.052	0.076	0.085
19	0.035	0.038	0.058	0.054	0.074	0.085
20	0.034	0.036	0.058	0.051	0.073	0.089
21	0.034	0.036	0.055	0.052	0.072	0.085

Table 8.5 *– Values of H_S in meter in scale 1:60, for the tests with L_C=65% and gap width 5b, under irregular and perpendicular 3D wave attacks. First six WSs represent ordinary sea states, whereas the last five WSs represent extreme sea states. Continued.*

	Ordinary Wave States					
WG	**1**	**2**	**3**	**4**	**5**	**6**
1	0.032	0.035	0.064	0.056	0.072	0.081
2	0.033	0.037	0.065	0.056	0.072	0.081
3	0.033	0.036	0.065	0.056	0.073	0.082
4	0.032	0.035	0.066	0.054	0.072	0.081
5	0.033	0.035	0.067	0.057	0.073	0.081
6	0.032	0.035	0.065	0.056	0.070	0.080
7	0.034	0.037	0.069	0.057	0.075	0.084
8	0.027	0.032	0.055	0.055	0.067	0.080
9	0.028	0.033	0.055	0.053	0.068	0.079
10	0.026	0.031	0.055	0.052	0.065	0.075
11	0.025	0.029	0.054	0.052	0.064	0.074
12	0.027	0.030	0.056	0.054	0.065	0.077
13	0.028	0.031	0.057	0.056	0.068	0.081
14	0.029	0.032	0.058	0.054	0.067	0.079
15	0.028	0.033	0.061	0.053	0.067	0.081
16	0.033	0.035	0.067	0.057	0.071	0.087
17	0.028	0.034	0.058	0.054	0.069	0.082
18	0.029	0.034	0.063	0.050	0.069	0.083
19	0.032	0.038	0.066	0.054	0.074	0.085
20	0.031	0.033	0.069	0.052	0.071	0.082
21	0.031	0.034	0.065	0.049	0.069	0.081

Table 8.6 *– Values of H_S in meter in scale 1:60, for the tests with L_C=50% and gap width 5b, under irregular and perpendicular 3D wave attacks. First six WSs represent ordinary sea states, whereas the last five WSs represent extreme sea states.*

For all the WSs, H_S is pretty constant in front of the wave-maker (i.e. WGs n. 1-7), being the average and the maximum variation 7% and 9% respectively (the maximum variation occurs for WS n. 3). In particular the H_S variation among WGs n. 1-7 is derived –for each WS– as the ratio between the maximum difference of H_S and their mean value.

As it was predictable, for the perpendicularly and ordinary WSs, the values of H_S are reduced behind the device close to its axis (i.e. WGs n. 8 to the n. 14) and then tend to increase again at its side (i.e. WGs n. 17 to the n. 21) regardless the mooring pre-tension level. Under oblique waves, instead, only few points can be considered sheltered by the devices, in particular near WGs n.16 - 17 (and sometimes of WGs n. 15-18). The sheltered effects are obviously more visible for ordinary than for extreme WSs.

For the extreme WSs, instead, H_S has a different trend, graphically reported in figure 8.3 for the easier of comprehension. The values of H_S at the WGs n. 8 to 14 are similar or higher than the incoming values recorded at the WGs n. 1 to 7. This aspect can be explained considering that:

1. under these WSs a large amount of incoming waves were breaking before or in correspondence of the devices, leading to a more chaotic wave field;
2. the devices moved much more under extreme than under ordinary WSs and furthermore they were not always able to harmoniously ride the waves. During the drop heaving motion phase the devices crashed into the water surface. These impulsive impacts generated radiated wave, which superimposed to the incoming waves increasing the H_S values at the WGs n. 8 to 14 with respect to the values at the WGs n. 1 to 7.

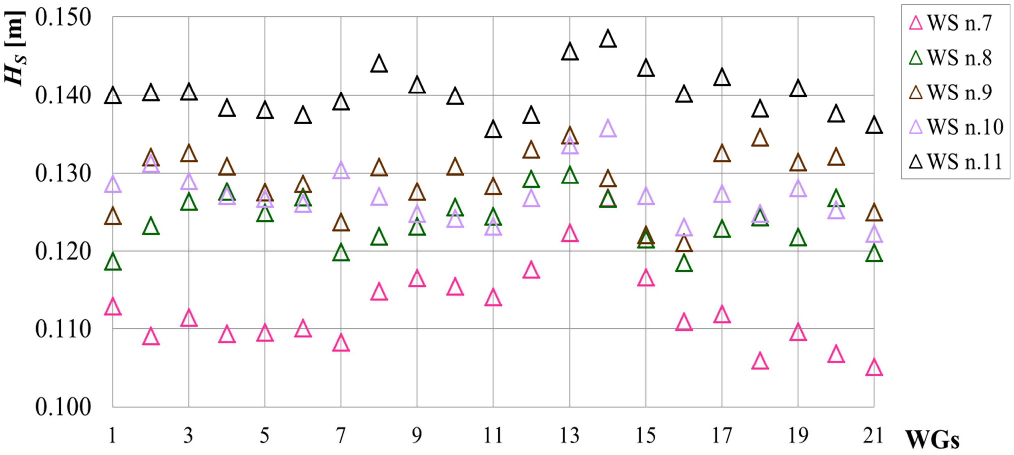

***Figure 8.3** – H_S recorded at the 21 WGs in the basin for the extreme WSs performed with the L_C=80% and a gap width of 5b*

The influence of the chain pre-tension level on the hydrodynamics around the models is investigated by comparing the H_S values for a same WS. Differently from what expected, H_S vary unsystematically with changes of the chain pre-tension levels, in fact an intermediate chain pre-tension level does not lead to intermediate H_S values with respect to the tense and slack chain cases. Figure 8.4 reports the ratio between H_S recorded at the 21 WGs and the H_S at the WG n. 3 (considered as a reference of the incoming wave height value) for the same WS n.5 (l/L_P=0.45) by varying L_C and so the chain pre-tension level. It is possible to note that the lower values of H_S have been achieved with an intermediate chain pre-tension level of 65%. With a tense chain (i.e. 50%) the values of H_S seem often lower or more similar with respect to the slack chain (i.e. pre-tension level 80%). An exception is represented by WS n. 3, with l/L_P= 0.70, where an increasing of the chain pre-tension (i.e. with 50 and 65%) leads to higher values of H_S achieved.

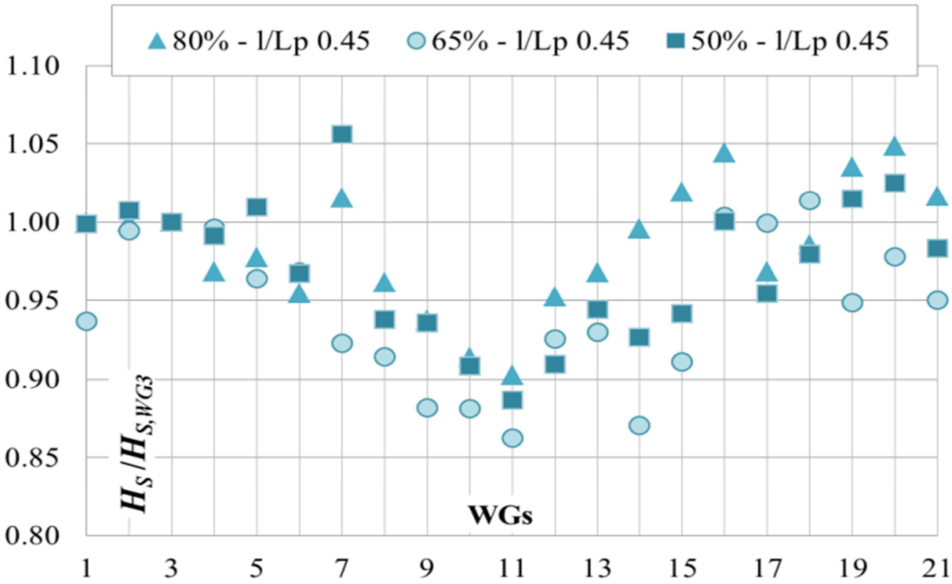

Figure 8.4 *– Ratio between the H_S recorded at the 21 WGs and the H_S at the WG n. 3 in function of different chain pre-tension levels for l/L_P= 0.45 (gap width 5b).*

The influence of the layout were investigated by varying the mutual long-shore distance between the devices, from the minimum value according to the mooring system (i.e. 2.0m, equals to 5*b*) to a maximum distance (i.e. 3.1m, equals to 8*b*) keeping constant the PTO rigidity and the mooring pre-tension level (r_4 and L_C=80% respectively).

The wider gap width leads to slight H_S variations for WSs carried out with the same wave paddle motion (see Fig. 8.5), with the exception of the WS n. 5, where there are differences also in the incoming H_S.

Slight differences (mainly related to the rear centre of the basin –WGs from n.9 to n.16– which is more exposed to the incoming waves than during perpendicular WSs) were also achieved under oblique WSs. Figure 8.5 lead to the conclusion that the two devices did not significantly interact with both the gap widths, therefore further analysis on the wider gap width were considered unnecessary and the configuration with a narrower gap is suggested for economical reason. Visual observations of the maximum long-shore device displacements also suggested that the minimum safe distance is around 3b. However, it should be examined if the gap width reduction assure a correct mooring operation and/or lead to wave interaction which decreases the wave height approaching the back devices, and therefore the energy production of the back line.

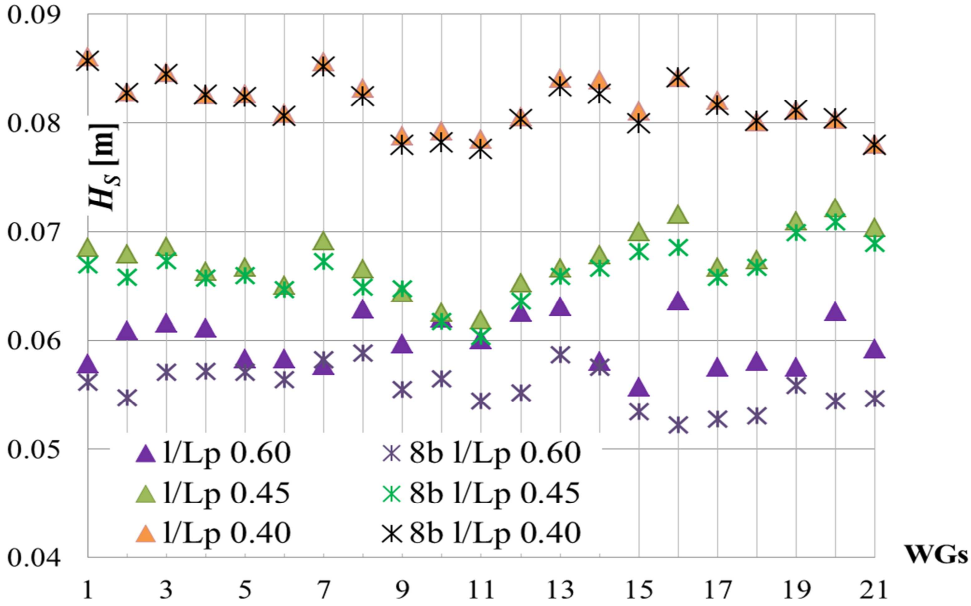

Figure 8.5 *– H_S at the 21 WGs: gap width 5b with triangles, 8b with stars for L_C= 80%.*

To better investigate the H_S variation induced by the device presence, an analysis of it in long-shore and cross-shore direction was performed. The analysis on the long-shore direction allows to investigate the extension of the wake induced by the radiated wave field generated by device heaving motion; whereas the analysis on the cross-shore direction allows to examine the minimum cross-shore distance between the wave farm lines, which allows wave height (and therefore wave energy) to increase again after the obstacles represented by the devices.

In the long-shore direction, the values of H_S at the WGs n. 10 and from n. 17 to 21 (which are at a cross-shore distance of 1.30*l* from the back cylinder of the back pontoon) were investigated as a function of the distance from the cross-shore device axis.

Under perpendicular wave directionality, the device should move essentially along its cross-shore axis without significant re-orientation. Therefore it is expected that H_S is minimum in correspondence of the device axis (i.e. at the WG n. 10) and then rapidly increases again up to the measured value at WG n. 3. Figure 8.6 plots –for an easier comprehension only related to WS n. 1, 2 and 5– the H_S at the WGs mentioned above including also the H_S for WG n. 3 to allow a direct comparison with the incident wave height. For the readability of the graph the value of H_S at the WG n. 3 is reported at the fictitious distance of -0.20 m (instead of 0 m).

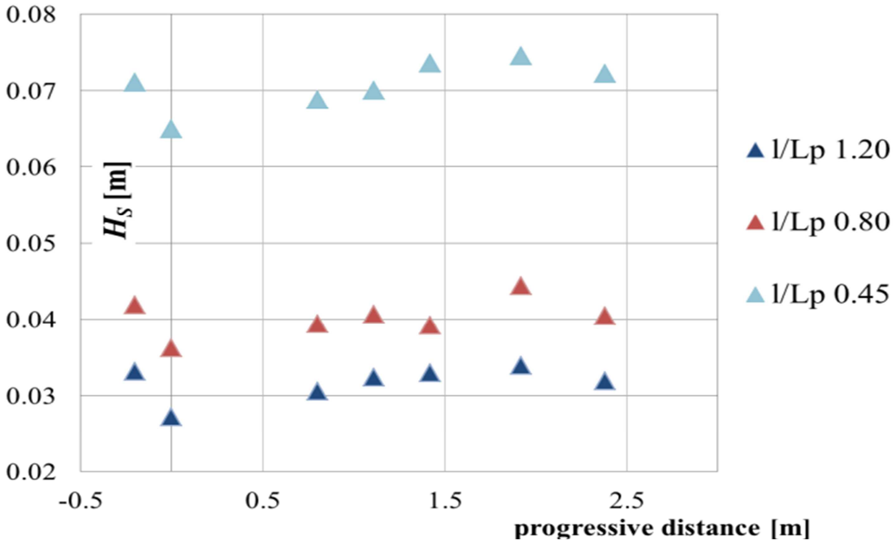

***Figure 8.6** – H_S at the WGs placed in a long-shore direction, i.e. WGs n. 10, 17-21, and n. 3 (gap width 5b, L_C=80%). To facilitate the comprehension only WS n. 1, 2 and 5 are plotted.*

Regardless the mooring pre-tension level, the value of H_S at WG n. 17 (at a distance of 0.80m from the cross-shore device axis) is still affected by radiated waves, whereas H_S at WG n. 18 (at a distance of 1.10m from the cross-shore device axis) seems to be already not affected by the presence of the device. This behaviour is more marked for higher WSs where H_S at WG n. 18 is more similar to H_S at WG n. 3. Therefore the wake zone extends for a distance of around 2.9*b* (i.e. until the WG n.18) from the device cross-shore axis for WGs measurements performed at a cross-shore distance of 1.30*l* from the back cylinder of the back pontoon. The wake angle is thus about 30° from the extreme of the back cylinder of the rear pontoon.

Considering also the incoming wave obliquity, the wake extension due to the device presence seems to be greater in case of oblique WSs with respect to the same perpendicular WSs. In fact, in case of oblique waves it is necessary to reach at least the WG n. 19 (at a distance of 1.40m from the cross-shore device axis), and so a wake extension around 3.5*b*. These indications suggest that with oblique waves and the same devices gap width of 5*b*, some wave interactions could occur among the devices.

In the cross-shore direction, the values of H_S at the WGs from n. 10 to 12 have been considered as a function of the distance from WG n. 10 itself (see Fig. 8.7), which is at a distance of 1.30*l* from the back cylinder of the back pontoon. For the readability of the graph, figure 8.7 includes also the incoming H_S at WG n. 3 at the fictitious device axis distance of -0.10 m (instead of the real distance of -3.30 m from the WG n. 10).

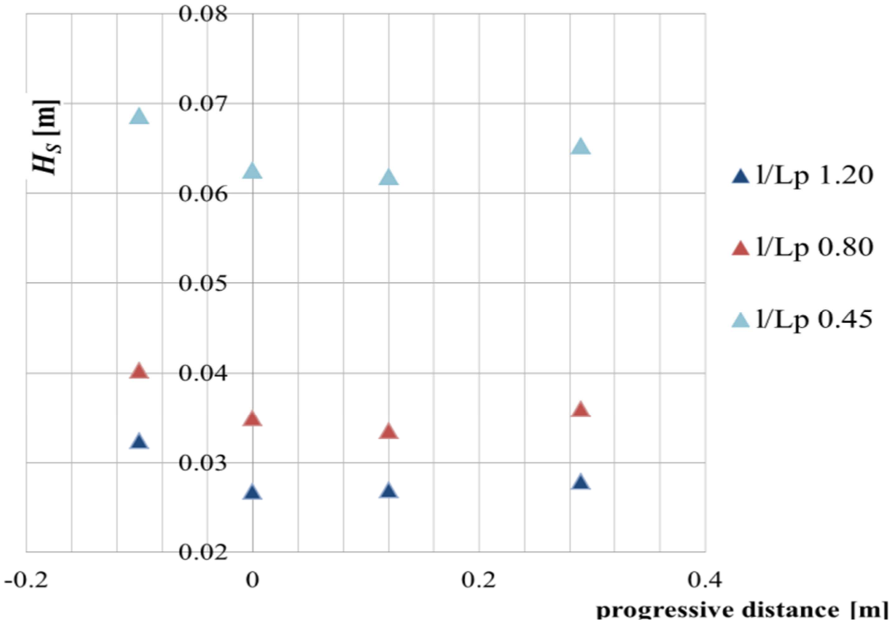

***Figure 8.7** – H_S at the WGs behind the device in a cross-shore configuration (WGs n. 10-12), and n. 3 (gap width 5b, L_C=80%). Only WS n. 1, 2 and 5 are plotted.*

The value of H_S at the WG n. 12 (which is at a distance of 1.65l from the back cylinder of the back pontoon) is still affected by the device, since it is always lower than H_S at the WG n. 3, and for the first 3 WSs the decay is more marked (being the differences between H_S at the WG n. 3 and at the n. 12 greater), these two aspects do not vary by varying the mooring pre-tension level or the wave obliquity (see Fig. 8.8a, b respectively).

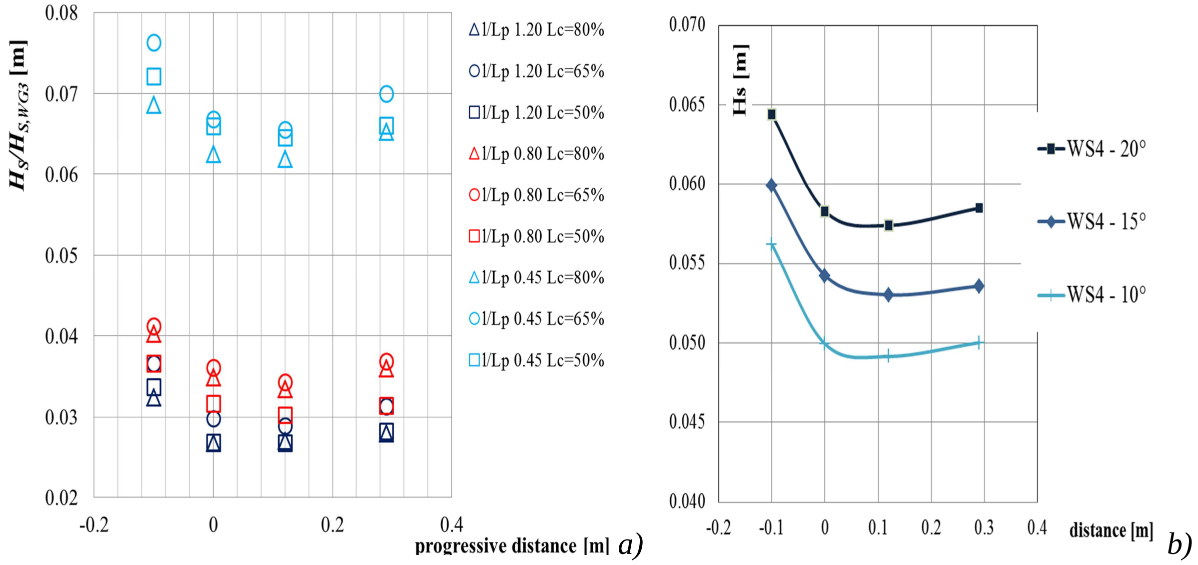

***Figure 8.8** – H_S at the WGs behind the device in a cross-shore configuration by varying the mooring pre-tension level (a) and the wave obliquity (b).*

In the frequency domain, two data elaboration methods were applied, one to the groups of three aligned WGs (Mansard and Funke's method) and one on the groups of 7 WGs (BDM). The first method allows to have information related to the wave energy (in terms of K_T, K_R and 2D spectra) approaching the device and behind it. K_T can be considered as an indicator of the residual wave height, and therefore wave energy, behind the device, whereas K_R gives an indication of the wave energy lost by reflection in front of the device itself. The estimation of the residual wave energy behind the device is an important factor to decide the number of the wave farm line/s. K_T, K_R are derived as indicated in the equations (1) and (2).

Table 8.7 reports K_T and K_R as a function of l/L_P for the three mooring pre-tension levels for each ordinary WS. The results for the extreme WSs are not reported because they have a modest interest due to the absence of reduction of H_S behind the device (as explained above).

A great amount of wave energy is transmitted behind the device, being the values of K_T always above 0.80. With the exception of WS n. 4, the values of K_T almost linearly decrease with increasing l/L_P. K_T is slightly higher for the lower pre-tension level (80%) and its dependence on l/L_P is less evident compared to the moderately taut (65%) and taut (50%) cases.
Also for oblique WSs, a great amount of wave energy is transmitted behind the device, being the values of K_T always above 0.80. For lower WSs, in fact K_T is lower for perpendicular WSs, a reason is connected to lower H_S recorded at the WGs n. 10-12 (with the exception of WS n. 4), whereas for higher WSs lower value of K_T are often derived for β=10°.

The K_R trend is opposite with respect to the trend for K_T, in fact it linearly increases with increasing l/L_P. For all the WSs the reflected wave energy is modest, being K_R always under 0.30, regardless the wave obliquity. For less intense WSs, K_R is lower under oblique than under perpendicular WSs. A reason could be that the reflected waves do not hit directly the WGs n. 3-5; whereas for higher WSs the wave field is more chaotic and therefore K_R does not change by varying the wave obliquity. Furthermore K_R seems to be independent from a change of mooring pre-tension level.

	WS	**1**	**2**	**3**	**4**	**5**	**6**
	l/L$_P$	**1.21**	**0.79**	**0.70**	**0.58**	**0.45**	**0.38**
K$_T$	***L$_C$* =80%**	0.87	0.88	0.87	1.00	0.93	0.91
	***L$_C$* =65%**	0.84	0.84	0.85	0.93	0.89	0.93
	***L$_C$* =50%**	0.84	0.89	0.88	0.90	0.89	0.89
K$_R$	***L$_C$* =80%**	0.27	0.22	0.19	0.18	0.17	0.15
	***L$_C$* =65%**	0.28	0.23	0.21	0.19	0.17	0.15
	***L$_C$* =50%**	0.30	0.21	0.19	0.16	0.17	0.15

***Table 8.7** – K_T and K_R behind and in front of the device respectively, as function of l/L_P for the three mooring pre-tension levels.*

Overall, these results are in agreement with the first investigation carried out in 1:60 scale (see Fig.s 7.5, 7.6 and 7.19) both in terms of trend and of values. In fact the lower values of K_T were found for l/L_P greater than 1.0, while the higher values of K_T were recorded for l/L_P around 0.7 (similarly to what happens with this second investigation, with WS n. 4 where l/L_P is 0.6).

The high values of K_T are also confirmed by the slightly differences between the incident and transmitted 2D wave energy spectra (see Fig. 8.9).

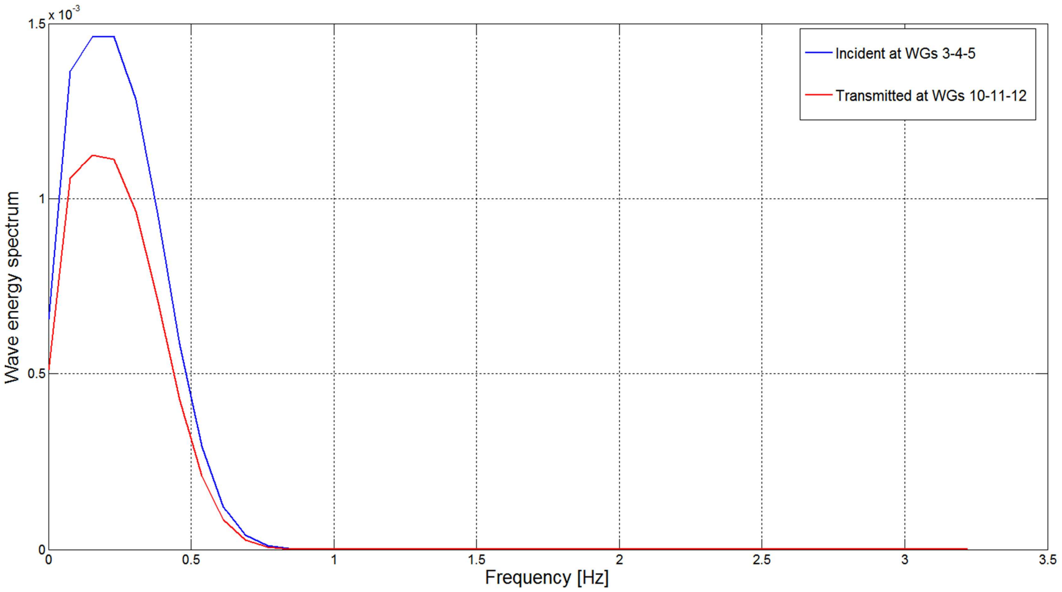

***Figure 8.9** – Incident and transmitted (behind the device) wave energy spectrum for the WS n. 10, L_C=80% with the gap width of 5b.*

By applying the BDM it is possible to derive the 3D wave energy spectra, and therefore to evaluate the incoming and transmitted wave directional spreading. The directional spreading has been assessed as $\Delta\theta = \theta_I - \theta_T$, where θ_I is the main incident wave direction of the WGs from n.1 to n.7 and θ_T is the main incident wave propagation derived at the WGs from n.8 to n.14. Table 8.8 resumes the values of $\Delta\theta$ for the three mooring pre-tension levels.

	WS	**1**	**2**	**3**	**4**	**5**	**6**
	l/L_P	**1.21**	**0.79**	**0.70**	**0.58**	**0.45**	**0.38**
Δθ [°]	**L_C =80%**	1.40	-1.60	-3.50	-4.10	-1.80	1.10
	L_C =65%	-4.10	-1.50	-2.10	-1.40	-2.40	-1.30
	L_C =50%	-2.80	-1.30	-1.50	-1.80	3.20	-0.60

***Table 8.8** – Incident wave direction variation ($\Delta\theta$) after the device reported in function of l/L_P for the three mooring pre-tension levels (for the gap width of 5b).*

For the slack mooring configuration (i.e. L_C=80%) the greater changes of the transmitted wave direction occur especially for WS n. 3 and 4, i.e. for the WSs characterised by the same $H_{S,TARGET}$ and by l/L_P around 0.65; in particular the maximum value of $\Delta\theta$ occurs for WS n. 4, which also corresponds to the highest value of K_T. By varying the mooring pre-tension level, L_C=80% seems to be the optimal configuration (with the exception of the WSs n. 3 and 4), since similar or lower $\Delta\theta$ have been registered for all the WSs leading to a greater predictability of the device performance.

Considering also the wave obliquity, it is possible to assess that the lower values of $\Delta\theta$ are recorded for the smaller wave obliquity β=10°, even if are pretty similar to the values of the perpendicular configuration. The higher values of $\Delta\theta$ appreciable for the greater wave obliquity (β=20°) can be justified by the greater device motion and consequent delay in its re-orientation back to the initial position.

8.2.2. POWER PRODUCTION RESULTS

An initial stage of the tests consisted in the optimisation of the PTO system based on the power production. Furthermore during this study, also the best mooring pre-tension level was chosen. The choice of the PTO rigidity and of the best mooring pre-tension was performed under perpendicular regular and irregular waves summarized in tables 8.1 and 8.2.

The device power production was assessed based on the data acquired from the PTO instrumentation, i.e. the load cell and the displacement sensor. Those data were elaborated in order to obtain the time series of the produced power P_{PTO} (in W) as follows:

$$P_{PTO}(t) = \frac{F(t)+F(t+\Delta t)}{2} \cdot \frac{d(t+\Delta t)-d(t)}{\Delta t} \tag{6}$$

where:

- Δt is the time step interval, equal to the inverse of the sample frequency;
- F(t), F(t+Δt) are the forces induced by the device to the PTO, respectively at the times t and t+Δt;
- d(t), d(t+Δt) are the relative device displacement at the respective time t and t+Δt.

Generally, a zero value of the power production means that the waves did not excited the displacement sensor, i.e. the wave energy was lower than the internal PTO friction at zero velocity. The results reported in the following refer to the average value of the time series of the power production. P_{PTO} values were also calculated by means of the angular velocity (i.e. the changing rate of the relative pitch angle) and of the torque at the hinge point. The results of the two elaborations were in pretty good agreement.

Under regular waves the study consisted of two phases:

- optimization of the PTO rigidity for each mooring pre-tension level;
- assessment of the best mooring pre-tension level for the given optimal PTO rigidity.

The optimization of the PTO was performed by increasing the vertical distance between the PTO and the device buoyancy plane. This distance was increased from 7cm (low damping) to 17 cm (high damping) by steps of 2cm, therefore using 5 (or eventually 6) different rigidity stages. In the following, the figures representing the damping *r* are indicated for example as r_1, the lower the distance the lower the rigidity number the lower the subscript.

The results are reported as a function of the l/L_P (each ratio represents a single WS) in the figures from 8.10 to 8.12 for L_C=80-65-50% respectively.

The best PTO configurations correspond to high rigidity values. In fact for L_C= 80% the r_4 (i.e. vertical distance of 0.13m) is the optimal PTO rigidity and for both L_C=65% or 50%, the r_5 (i.e. vertical distance of 0.15m) is the optimal PTO rigidity. In particular, it is possible to assess that the power production linearly increases by increasing the rigidity since a target value, e.g. for the slack configuration (see Fig. 8.10) from the lower to the best rigidity the power production increases of 2.4 times.

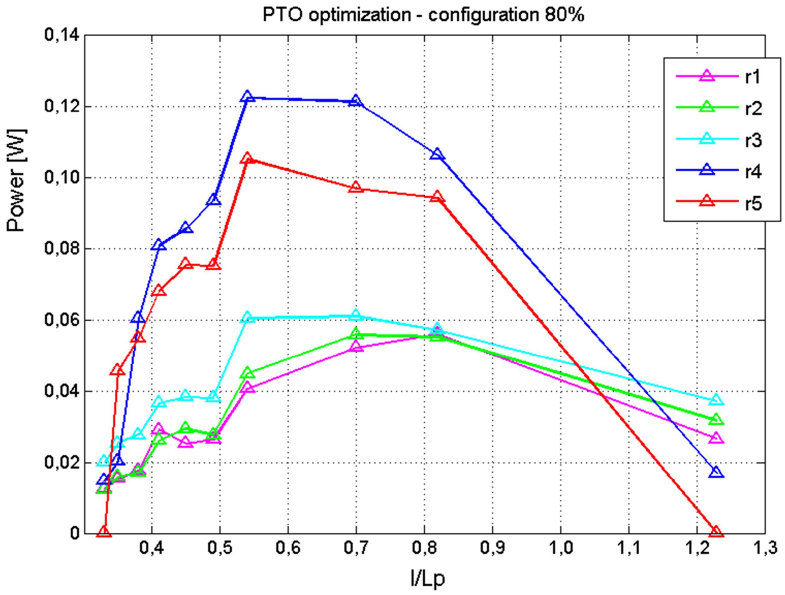

***Figure 8.10 –** PTO rigidity optimization under 10 RW (in terms of l/L_P) for the configuration with L_C=80%. Five PTO rigidity were analysed, where r_1 is the less rigidity configuration. The optimal PTO rigidity correspond to r_4 (PTO height=13cm).*

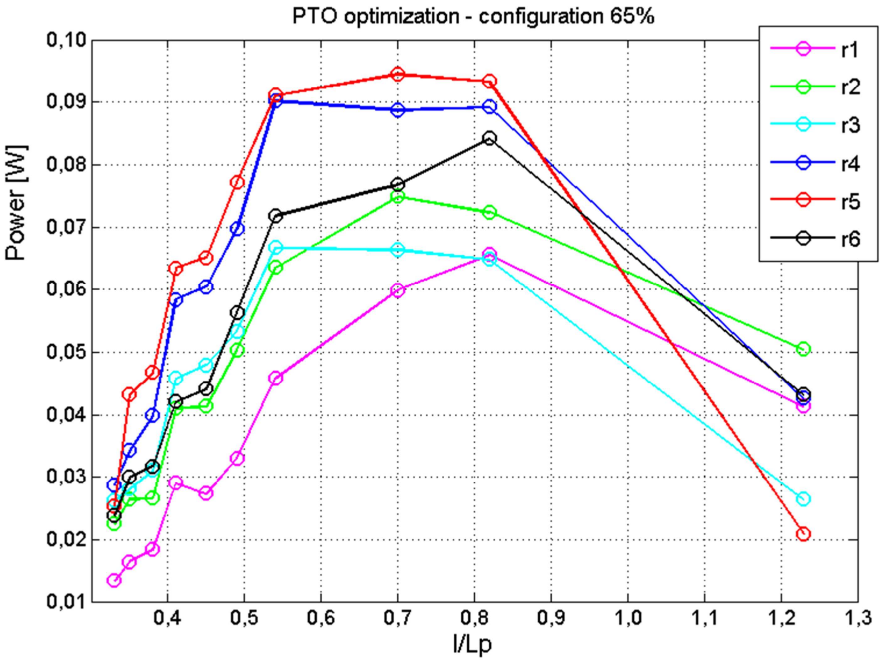

***Figure 8.11** – PTO rigidity optimization under 10 RW (in terms of l/L$_P$) for the configuration with L$_C$=65%. Six PTO rigidity were analysed, where r$_1$ is the less rigidity configuration. The optimal PTO rigidity correspond to r$_5$ (PTO height=15cm).*

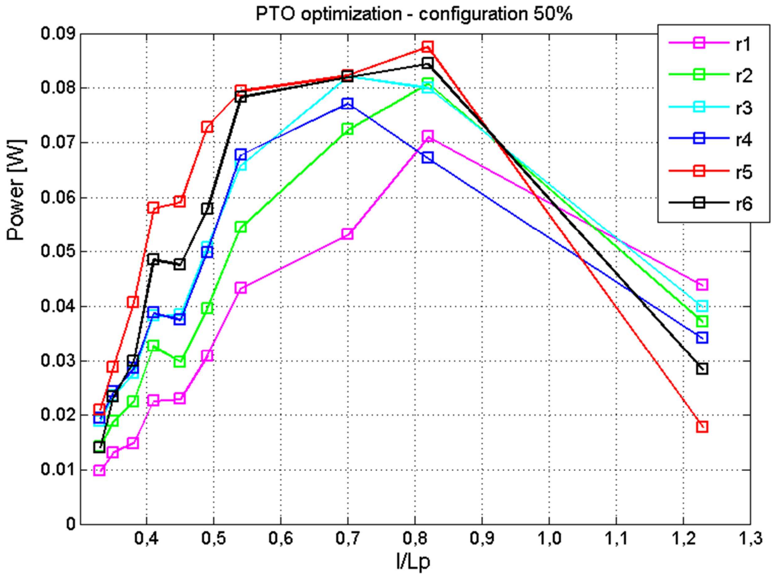

***Figure 8.12** – PTO rigidity optimization under 10 RW (in terms of l/L$_P$) for the configuration with L$_C$=50%. Six PTO rigidity were analysed, where r$_1$ is the less rigidity configuration. The optimal PTO rigidity correspond to r$_5$ (PTO height=15cm).*

Once the best PTO configuration for each pre-tension level was found, the power production was compared for the three optimal PTO rigidities and the corresponding pretension levels (see Fig. 8.13). Figure 8.13 shows that the slack pre-tension level (L_C=80%) results to be the best configuration. However to validate this results a similar study was performed also under irregular waves (see Fig. 8.14).

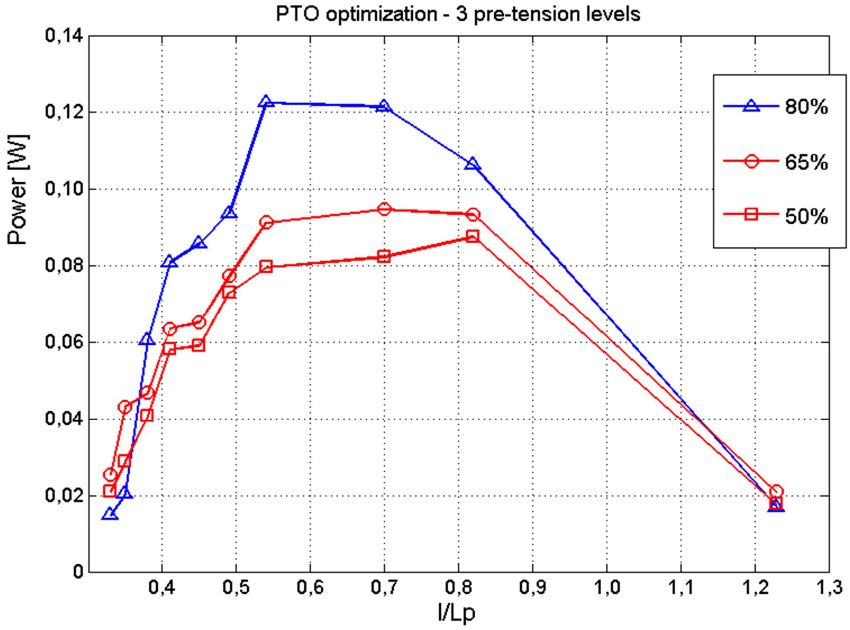

***Figure 8.13** – Mooring pre-tension level optimization based on the best PTO rigidity, under 10 RW (in terms of l/LP). Value of L_C=80 – 65 – 50% are represented with triangles, circles and squares respectively. Blue line colour indicates the r_4 rigidity, whereas red line colour indicates the r_5 rigidity.*

The combination of the results obtained from regular and irregular tests shows that the optimal PTO rigidity and chain pre-tension level to optimise the power production correspond to r_5 (high damping) and to the slack configuration respectively.

By assuming for sake of simplicity the same probability of occurrence for each WS, the power production decreases by increasing the mooring pre-tension level of the 6% for L_C=65% and of the 16% for L_C=50% compared to L_C=80%. Furthermore regardless the mooring pre-tension level, sets of P_{PTO} show high values when l/L_P is less than 0.70 (see Fig. 8.14).

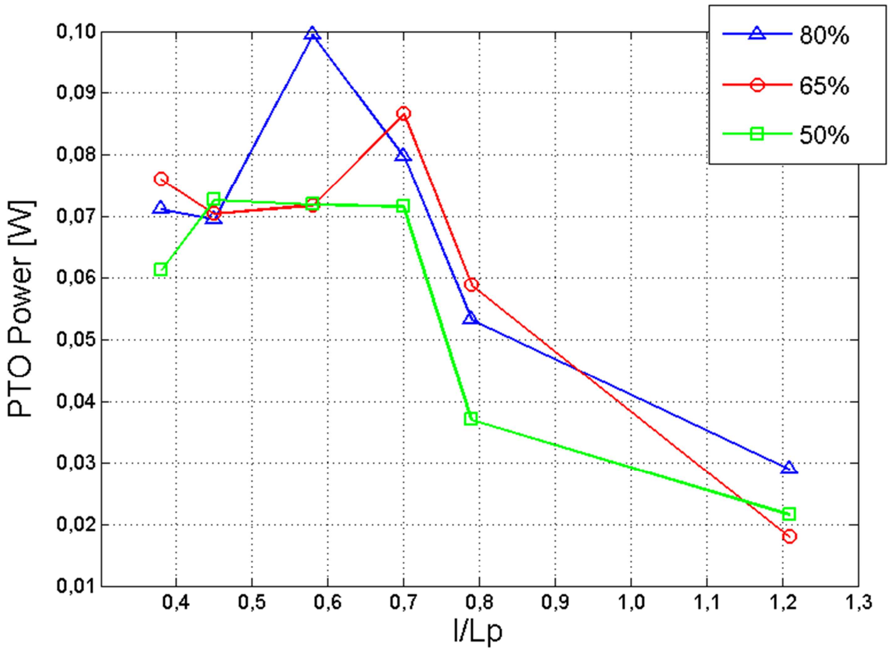

***Figure 8.14** – Power production performance in function of l/L_P for the 6 irregular WSs. Blue triangles, red circles and green squares for L_C=80 – 65 – 50% respectively (each with its best PTO rigidity). L_C=80% is confirmed as the best mooring pre-tension level.*

The device efficiency η was derived as the ratio between P_{PTO} and the available wave power (P_W, in W) as follow and summarised in the tables 8.9 and 8.10 in scale 1:60 and in full scale respectively. Data of power performance at the device were recorded only under ordinary WSs (i.e. WSs from n. 1 to n.6). For the extreme WSs, the PTO system was present on the device but it was not instrumented. This choice was made to protect the measuring systems from splashes due to the high frequency of breaking waves.

$$P_W = \rho \cdot g^2 \cdot \frac{H_S^2 \cdot T_P}{64 \cdot \pi} \cdot b \qquad (7)$$

$$\eta = \frac{P_{PTO}}{P_W} \qquad (8)$$

where:

- ρ is the water density, 1000 [kg/m3];
- g is the gravity acceleration, 9.81 [m/s2];
- H_S is the significant wave height [m];
- T_P is the peak wave period [s];
- b is the device width, 0.38 [m].

	WS	**1**	**2**	**3**	**4**	**5**	**6**
	l/L_P	**1.21**	**0.79**	**0.70**	**0.58**	**0.45**	**0.38**
L_C =80%	**P_W [W]**	0.09	0.17	0.39	0.49	0.75	1.30
	P_{PTO} [W]	0.031	0.059	0.084	0.107	0.074	0.077
	η	33.3%	33.7%	21.5%	21.8%	9.9%	5.9%
L_C =65%	**P_W [W]**	0.13	0.18	0.41	0.43	0.91	1.57
	P_{PTO} [W]	0.024	0.064	0.098	0.079	0.082	0.086
	η	18.3%	35.2%	24.0%	18.4%	8.94%	5.5%
L_C =50%	**P_W [W]**	0.10	0.15	0.35	0.44	0.86	1.25
	P_{PTO} [W]	0.025	0.040	0.078	0.078	0.081	0.069
	η	24.2%	26.6%	21.9%	17.7%	9.4%	5.5%

Table 8.9 *– Summary of the P_W, P_{PTO} and η under ordinary WSs for a gap width of 5b and for the three mooring pre-tension levels. Data are in scale 1:60.*

	WS	**1**	**2**	**3**	**4**	**5**	**6**
	l/L_P	**1.21**	**0.79**	**0.70**	**0.58**	**0.45**	**0.38**
L_C =80%	**P_W [W]**	155.5	291.2	656.1	822.8	1250.5	2177.9
	P_{PTO} [W]	51.7	98.2	141.2	179.0	124.3	128.5
	η	33.3%	33.7%	21.5%	21.8%	9.9%	5.9%
L_C =65%	**P_W [W]**	169.5	251.2	592.2	737.9	1443.6	2095.8
	P_{PTO} [W]	41.0	66.8	129.8	130.7	135.2	115.6
	η	18.3%	35.2%	24.0%	18.4%	8.94%	5.5%
L_C =50%	**P_W [W]**	215.9	304.3	685.0	719.2	1524.6	2620.6
	P_{PTO} [W]	39.5	107.2	164.1	132.2	136.4	144.2
	η	24.2%	26.6%	21.9%	17.7%	9.4%	5.5%

Table 8.10 *– Summary of the data in 1:1 scale of the P_W, P_{PTO} and η under ordinary WSs for a gap width of 5b and for the three mooring pre-tension levels.*

Figure 8.15 shows the dependence η on l/L_P for the three mooring pre-tension levels; sets of η show pretty well marked peaks around l/L_P=0.80 or greater.

Analogous to the perpendicular wave condition, table 8.11 reports the results of the P_W, P_{PTO} and η in scale 1:60 for perpendicular and oblique waves. Even for oblique waves, data of power performance at the device were recorded only under ordinary WSs (i.e. WSs from n. 1 to n.6).

Figure 8.16 shows the dependence of η on l/L_P for L_C=80% under perpendicular and oblique waves. The trend of η remains constant by varying the wave obliquity (i.e. peaks around l/L_P=0.80 for orthogonal and oblique WSs). The effects of the wave obliquity is limited, however η tends to decrease for wave obliquity greater than 10°.

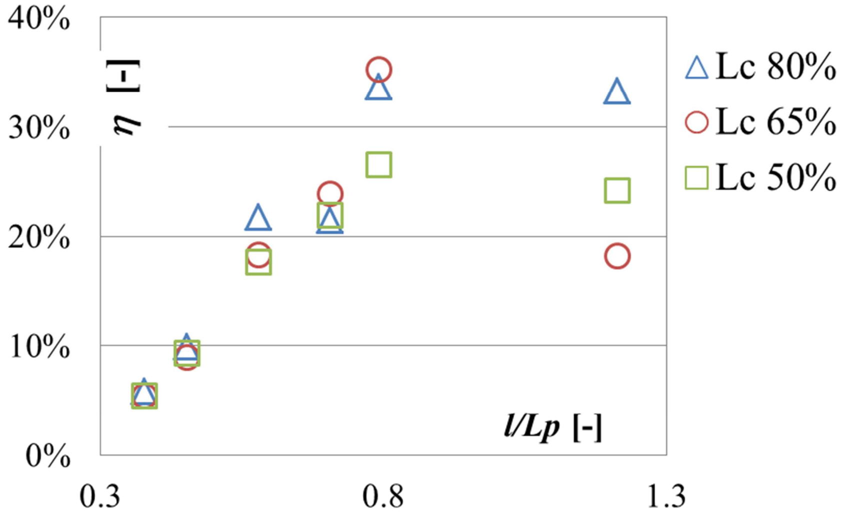

Figure 8.15 – *η against l/LP under ordinary WSs for the three mooring pre-tension levels.*

	β_1=0°			β_2=10°			β_3=15°			β_4=20°		
WS	P_w [W]	P_{PTO} [W]	η [-]	P_w [W]	P_{PTO} [W]	η [-]	P_w [W]	P_{PTO} [W]	η [-]	P_w [W]	P_{PTO} [W]	η [-]
1	0.09	0.03	33.3%	-	-	-	-	-	-	-	-	-
2	0.17	0.06	33.7%	0.15	0.05	35.5%	-	-	-	0.18	0.06	31.5%
3	0.39	0.08	21.5%	0.36	0.09	24.3%	-	-	-	0.41	0.09	20.4%
4	0.49	0.11	21.8%	0.43	0.08	17.6%	0.48	0.06	13.2%	0.55	0.08	14.5%
5	0.75	0.07	9.9%	0.85	0.09	10.4%	0.88	0.06	6.8%	0.86	0.08	8.9%
6	1.30	0.08	5.9%	1.30	0.08	6.2%	1.36	0.07	4.9%	1.66	0.08	4.6%

Table 8.11 – *Summary of the P_W, P_{PTO} and η under ordinary WSs for a gap width of 5b, L_C=80%, for perpendicular and oblique WSs. Data are in scale 1:60.*

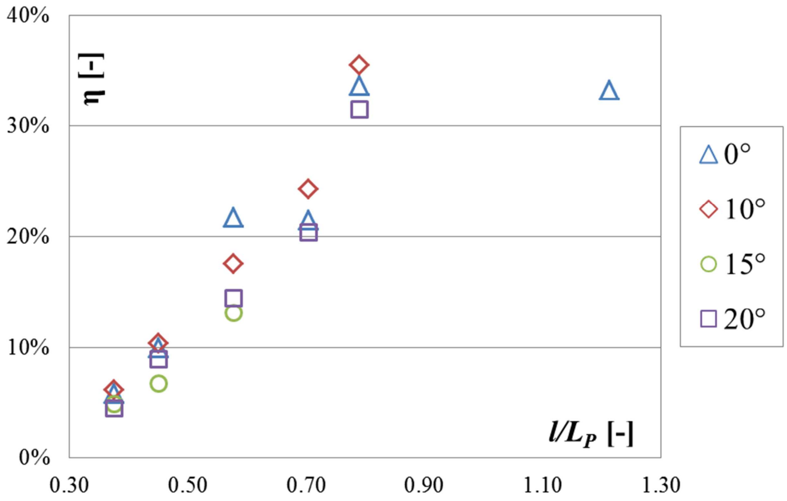

Figure 8.16 – *η against l/L_P for L_C=80% under perpendicular and oblique waves.*

8.2.3. MOORING RESULTS

The forces acting on the mooring chains were derived from a time domain analysis of the data recorded from the load cells by means of the WaveLab software (Aalborg University, 2007b). The results of this procedure are statistical values, e.g. F_{MAX} (i.e. the maximum value recorded), $F_{1/100}$ (i.e. the mean value of the 1% of the highest points), $F_{1/50}$ (i.e. the mean value of the 2% of the highest points), $F_{1/20}$ (i.e. the mean value of the 5% of the highest points) and in $F_{1/3}$ (i.e. the mean value of the 33% of the highest points).

In the following, "F" and "B" indicate the chains respectively in front of the wave maker and on the back of the device. The letters "R" and "L" denote the chains that are respectively to the right and to the left of the device, for an observer standing on the gravel beach and looking at the wave maker (see Fig. 8.1). All the values of the forces, even under extreme WSs were well below the chain failure condition (breaking limit around 1000N).

The load cell signals were very susceptible to the electrical noise typically present in the laboratory. The noise mainly affected the reliability of the maximum values (F_{MAX}), hence further observations were based on the statistical values only.

Figure 8.17 represents the statistical values of the forces acting on the four mooring lines as functions of the WS for the mooring pre-tension level L_C=80%, whereas figure 8.18 shows the effects of the mooring pre-tension level on the same FL chain, as functions of the WS.

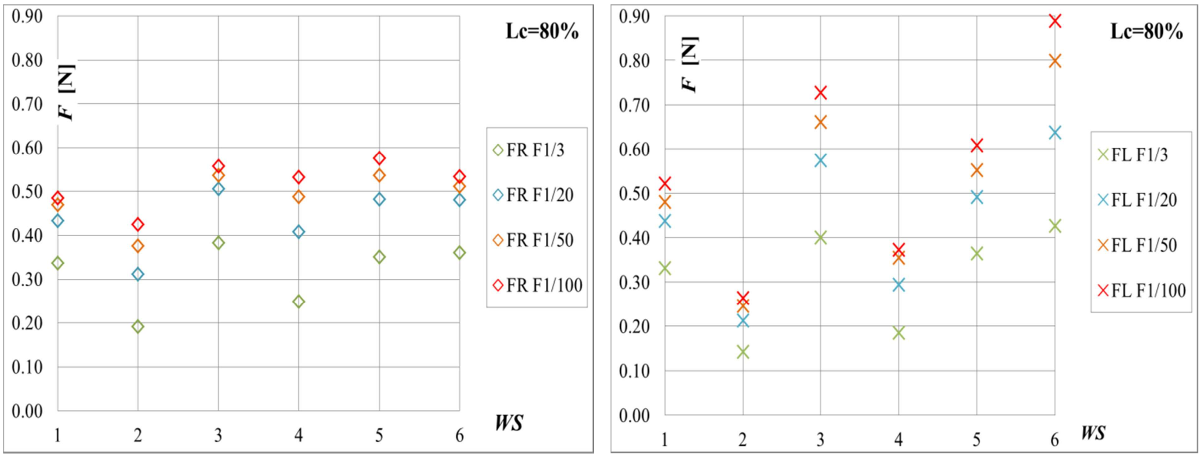

Figure 8.17 – *Statistical values ($F_{1/3}$, $F_{1/20}$, $F_{1/50}$, $F_{1/100}$) of the force acting on the FR chain on the left, on the FL chain on the right for the mooring pre-tension level L_C=80%. To be continued*

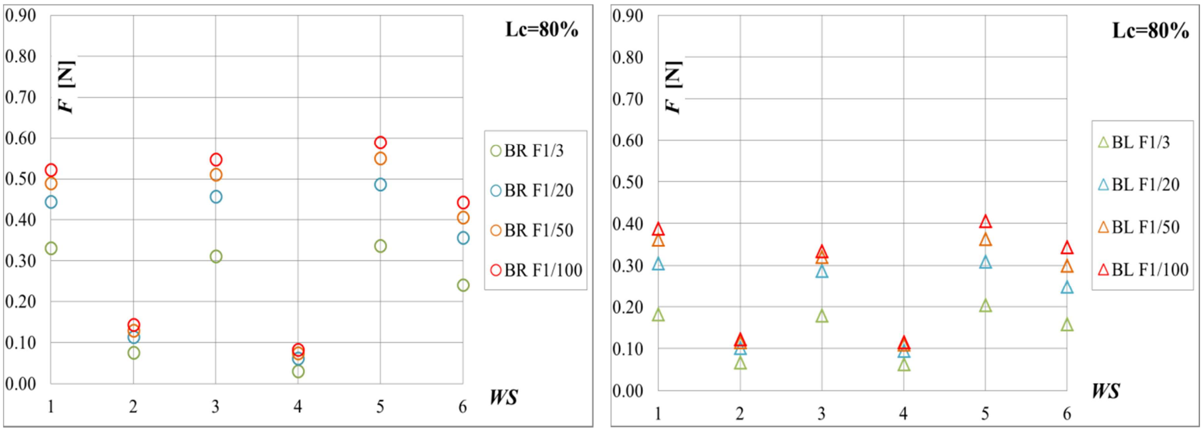

Figure 8.17 – *Statistical values ($F_{1/3}$, $F_{1/20}$, $F_{1/50}$, $F_{1/100}$) of the force acting on the BR chain on the left, on the BL chain on the right for the mooring pre-tension level L_C=80%. Continued.*

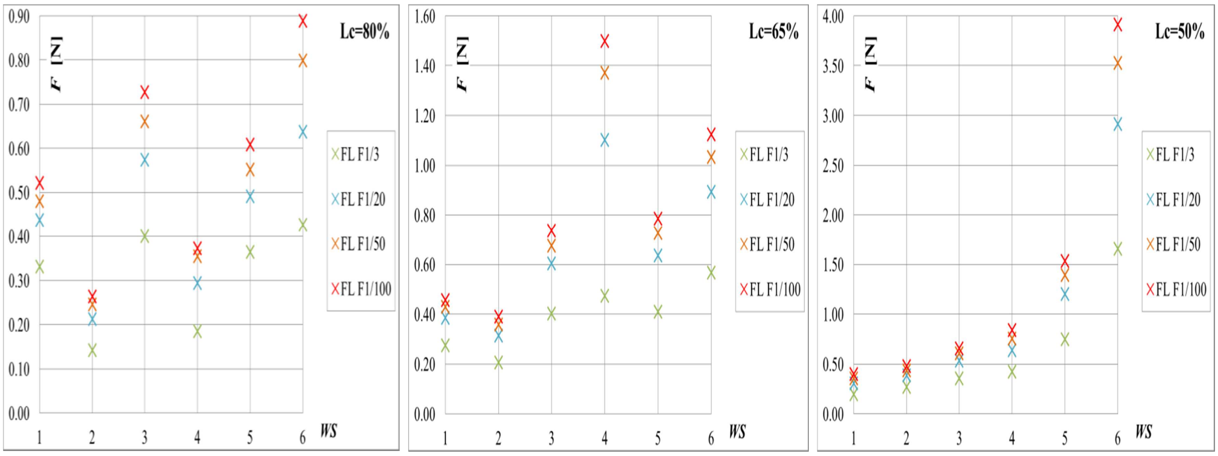

Figure 8.18 – *$F_{1/3}$, $F_{1/20}$, $F_{1/50}$, $F_{1/100}$ of the force acting on the FL chain for the three L_C.*

The comparison of figures 8.17 and 8.18 shows –as it was predictable– that an increasing of the mooring pre-tension level (i.e. from L_C=80% to L_C=50%) leads to an increase of the forces acting on every mooring line and that for the front chains the dependence of the force trend on the WS (i.e. on the available wave power) is more pronounced.

Furthermore, for a same WS differences can be found in the values recorded at the FR and FL chains and also between the two back chains. These differences are mainly related to electrical noise and/or small change in the geometry configuration (e.g. interlocking of one or more chain elements) which leads to different reliability of the measured forces as it was well observed during the analysis of the time series. That is why it is suggested to consider –as trustworthy– only some tests and the related forces acting on the most stressed chain (see Tab. 8.12).

Figure 8.19 graphically reports the trends of $F_{1/50}$ with L_C=80%; it is possible to note that for the ordinary WSs the forces are lower for perpendicular wave attacks, whereas for the extreme WSs the trend is the opposite.

WS	**L_C =80%**				**L_C =65%**	**L_C =50%**
	β_1=0°	**β_2=10°**	**β_3=15°**	**β_4=30°**	**β_1=0°**	**β_1=0°**
1	0.47	-	-	-	-	-
2	0.25	0.58	-	0.53	0.45	0.25
3	0.54	0.98	-	0.83	0.63	0.54
4	0.36	0.53	0.65	0.67	0.70	0.36
5	0.54	0.82	0.69	0.66	1.39	0.54
6	0.51	0.68	0.81		-	-
7	-	1.54	-	1.20	-	-
8	1.20	1.54	-	-	-	-
9	3.14	-	-	-	-	-
10	4.87	2.28	-	2.73	-	-
11	6.33	4.76	-	1.48	-	-

***Table 8.12 –** Most reliable tests in relation to the forces acting on the mooring system under perpendicular and oblique waves for the three L_C. Value of the forces $F_{1/50}$ measured in 1:60 scale expressed in Newton.*

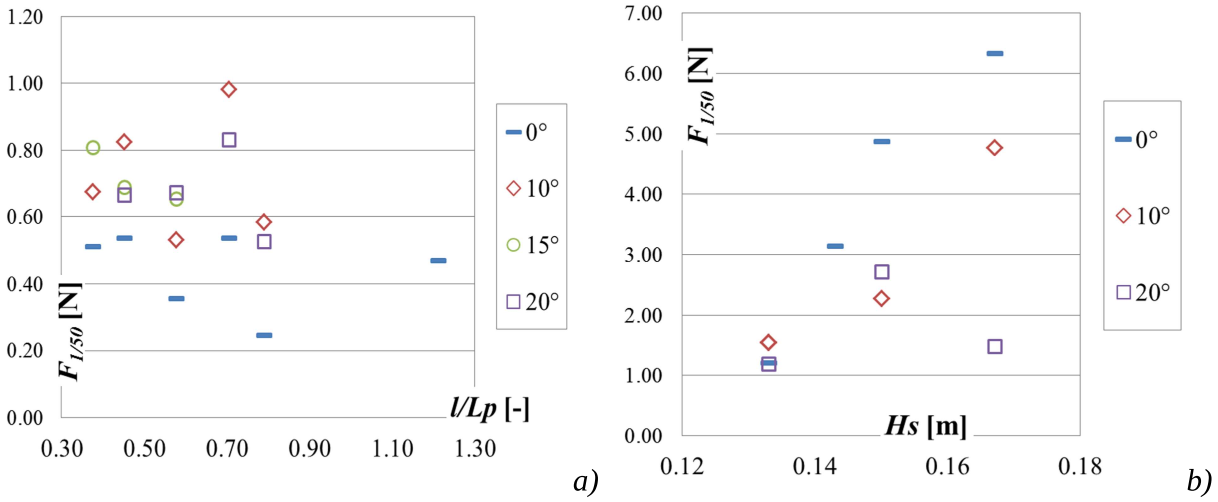

a) *b)*

***Figure 8.19 –** $F_{1/50}$ of the reliable signals of the force under perpendicular and oblique waves (with L_C=80%) for ordinary WSs (a) and extreme WSs (b).*

8.2.4. MOTIONS RESULTS

The possible motions of the device under analysis are 7, i.e. the 6 canonical Degree of Freedom (DoF) represented in figure 8.20, plus the relative pitch motion.

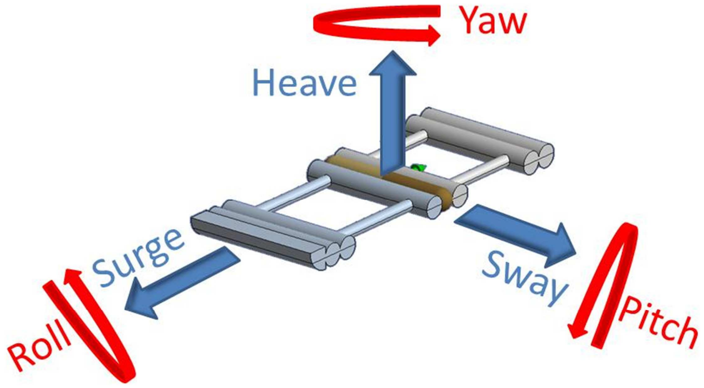

Figure 8.20 – *Possible movements for the device under exam.*

The motion measures in the canonical 6 DoF were obtained from the two MTi signals, positioned at the bow and stern of the device (see Fig. 8.2). The raw output consisted of three accelerations, related to the local coordinate system, and three Euler angles. In order to evaluate the position of the device in its fixed coordinate system (at the hinge position), the following steps were undertaken:

1. removal of the acceleration due to the gravity;
2. double integration of the acceleration signals;
3. filtering of the obtained position signals (a high pass filter was used to remove the linear and eventually second order term caused by the double integration procedure);
4. transposition of the signal from local to fixed coordinate system through a rotation matrix, described in turn from the Euler angles. In particular in order to remove the effect of the rotation on the displacements, the position of the floating WEC is transposed at the hinge position.

Due to the procedure describe above, it is obvious that the motions have different reliability levels; in particular the angle motions are more consistent than the translations, because they do not need the double integration procedure and the relative filter application. An example of the effects of the procedure on the surge signal is shown in figure 8.21.

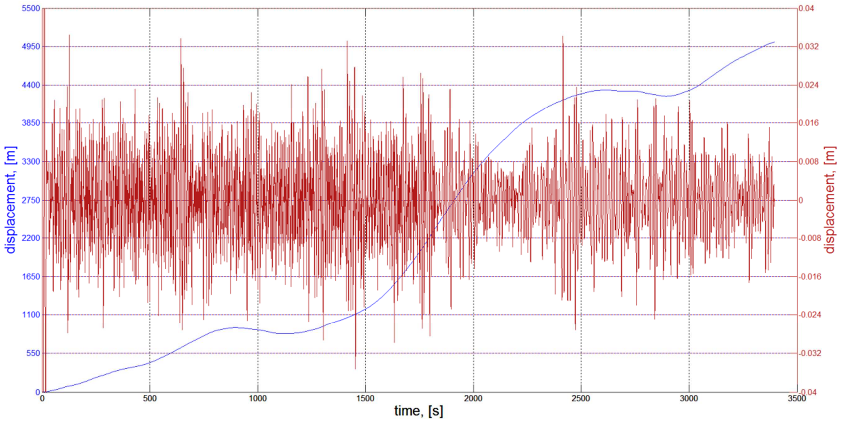

***Figure 8.21** – Same surge signal in the time domain, after the double integration (in blue) and after the filtering (in red). The filter removes fictitious amplifications due to a double integration.*

The time series of the 6 canonical motions data were derived once the previous procedure was performed on the MTi signals. These time series were first compared with the incoming wave signals (in particular with the WG n. 3 signal) and then analysed in terms of motion amplitude and finally considering also the motion directions.
The time series of the relative pitch angle (i.e. the 7th DoF) can be calculated as the instantaneous difference between the pitch signals of the two MTi placed at the two pontoon of the same device (see Fig. 8.2). However the measurements at the two MTi showed a different number of points, so that it was not possible to reconstruct the instantaneous correspondence of the two time series.

Figure 8.22 reports an example of the motion-wave comparison in the frequency domain, considering the surge motion for the WS n.1 with L_C=80%.

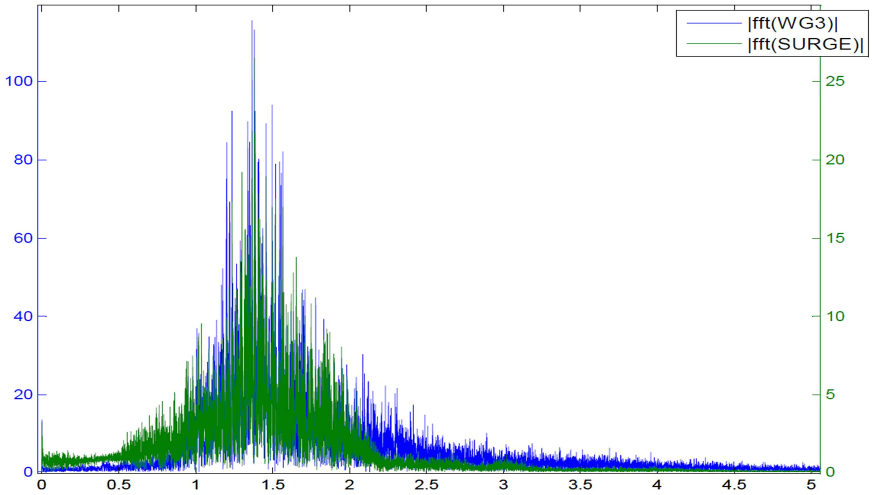

***Figure 8.22** – Surge and incoming wave signal in the frequency domain. In the x-axis the frequency in Hz, in the y-axis the spectra value.*

The comparison between the two frequency signals shows –as expected– a good agreement between surge and wave. In fact the surge spectra has a major peak in correspondence to the main incoming wave frequency (1/0.72=1.4Hz) and a minor energetic zone in correspondence to frequencies that are very low (around 0Hz) and close to its natural period (T_N=7.1s, see Tab. 8.14).

The motion amplitudes were derived through a zero-down crossing analysis of the signals. Table 8.13 reports the mean value of the 10% of the highest points for each WS and for the three L_C.

		Ordinary Wave States					
Motion	**Chain FL**	**1**	**2**	**3**	**4**	**5**	**6**
***Surge* [m]**	L_C = **80%**	0.010	0.012	0.017	0.026	0.037	0.046
	L_C = *65%*	0.009	0.012	0.018	0.028	0.041	0.051
	L_C = *50%*	0.010	0.012	0.021	0.032	0.050	0.061
***Heave* [m]**	L_C = **80%**	0.016	0.035	0.051	0.060	0.068	0.085
	L_C = *65%*	0.013	0.030	0.043	0.055	0.067	0.079
	L_C = *50%*	0.015	0.022	0.038	0.055	0.073	0.081
***Sway* [m]**	L_C = **80%**	0.003	0.005	0.010	0.012	0.014	0.017
	L_C = *65%*	0.004	0.005	0.007	0.011	0.023	0.017
	L_C = *50%*	0.003	0.005	0.008	0.014	0.015	0.021
***Roll* [°]**	L_C = **80%**	2.59	2.48	3.46	3.18	3.14	3.63
	L_C = *65%*	4.69	2.56	2.84	3.27	4.13	3.59
	L_C = *50%*	2.64	1.99	2.80	3.20	3.28	3.90
***Yaw* [°]**	L_C = **80%**	5.31	7.34	11.14	12.94	14.09	15.73
	L_C = *65%*	3.45	5.04	8.55	12.23	13.15	15.08
	L_C = *50%*	3.32	3.90	7.67	11.73	13.40	13.13
***Pitch* [°]**	L_C = **80%**	5.86	9.57	13.09	13.49	14.34	16.30
	L_C = *65%*	4.94	8.97	12.34	13.51	14.47	16.01
	L_C = *50%*	5.61	7.64	11.31	13.47	14.95	15.88

Table 8.13 – *Amplitude of the device motion. Data obtained from the MTi and elaborated through a time domain analysis. The data represent the statistical value of the 10% of the highest points for each ordinary WS for the three mooring pre-tension levels.*

To investigate if there was a prevalent movement direction, the times series of the motion were divided in two signals accounting for the (positive and negative) directions of the motion. Figure 8.23 shows an example of the procedure for the surge signal.

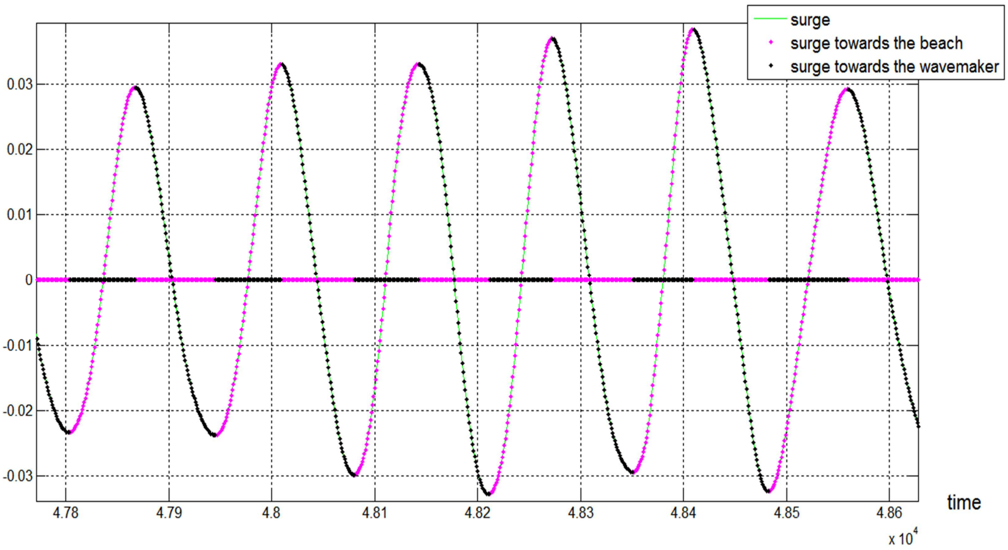

Figure 8.23 – *Division of the surge signal considering its directions (i.e. toward the beach in magenta and toward the wave-maker in black). Data related to the WS n.6 and* L_C*=80%.*

In this case the mean values of the 10% of the higher motion were derived as the sum between the 10% of the higher motions in both the directions. The trend of the mean values of the 10% of the higher motions is reported as a function of l/L_P for the three L_C and for the ordinary irregular WSs (see Fig. 8.24 and 8.25).

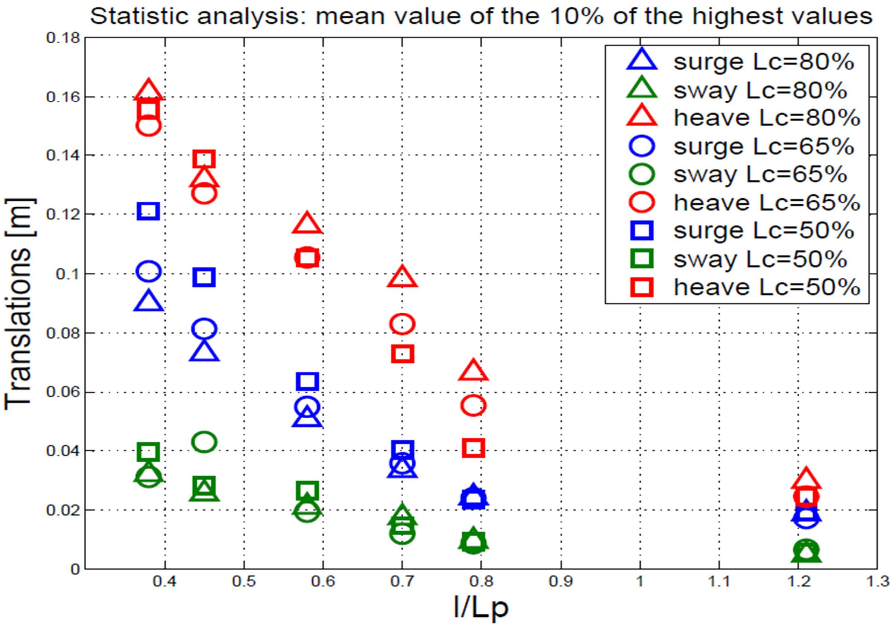

Figure 8.24 – *Statistical analysis of the translations: representation of the mean value of the 10% of the higher values, as a function of* l/L_P *for the three chain pre-tension levels* L_C*.*

The second analysis shows that there are not prevalent motion directions. The two analyses differ by an order almost equal to two, however they have similar trends. In fact, all the motions tend to decrease with increasing l/L_P. This parameter was selected since it has been shown that it affects the power production, while the dependence of the motions on H_S is rather obvious (i.e. the motions tend to increase with increasing H_S).

When analysing the translations, it can be observed that the mooring pre-tension level affects the surge motion for $l/L_P<0.70$. The heave seems to be independent from the pre-tension level, except around $l/L_P=0.70-0.80$, whereas the sway seems always independent from L_C. In particular, for most WSs, the heave decreases and the surge increase with decreasing L_C.
For all L_C, the surge and sway motions are indeed limited compared to the heave motion, proving that the moorings are effective in keeping the device position, and in particular the smallest motion is the sway.

When analysing the rotations (see Fig. 8.25), pitch and yaw are much greater than roll, and both tend to decrease with decreasing L_C. The roll motion seems to be independent from incident wave energy and from L_C.

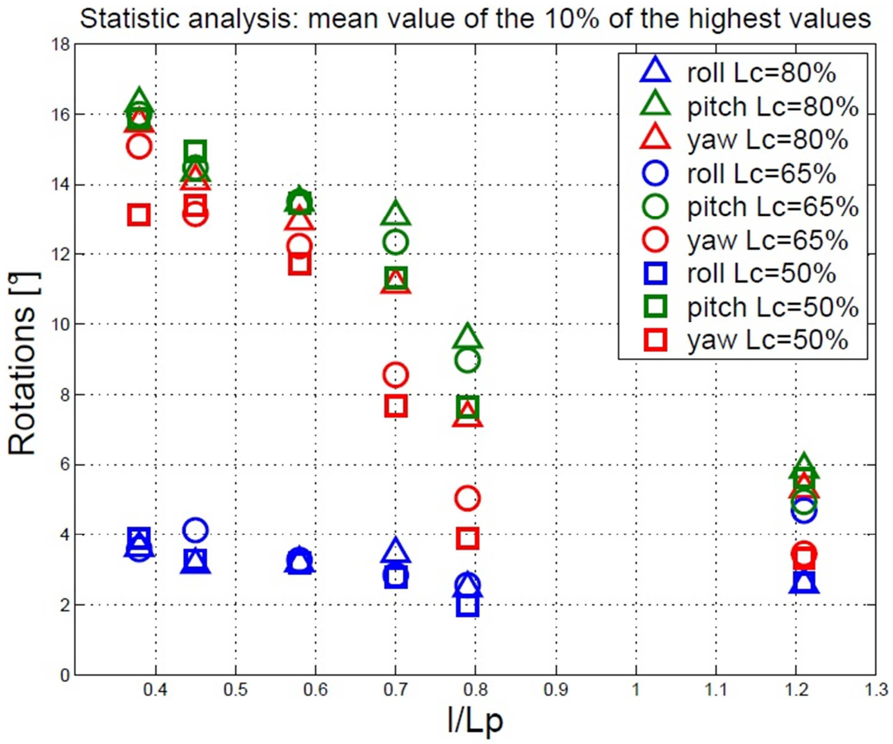

Figure 8.25 – *Statistical analysis of the rotations: representation of the mean value of the 10% of the higher values, as a function of* l/L_P *for the three chain pre-tension levels* L_C.

Even if the measurements at the two MTi showed a different number of points, an attempt of the evaluation of the relative pitch statistical value was made, and it emerged a linear relation between the relative pitch and the device power production (see Fig. 8.26). This result proved that the PTO is truly activated by this angle.

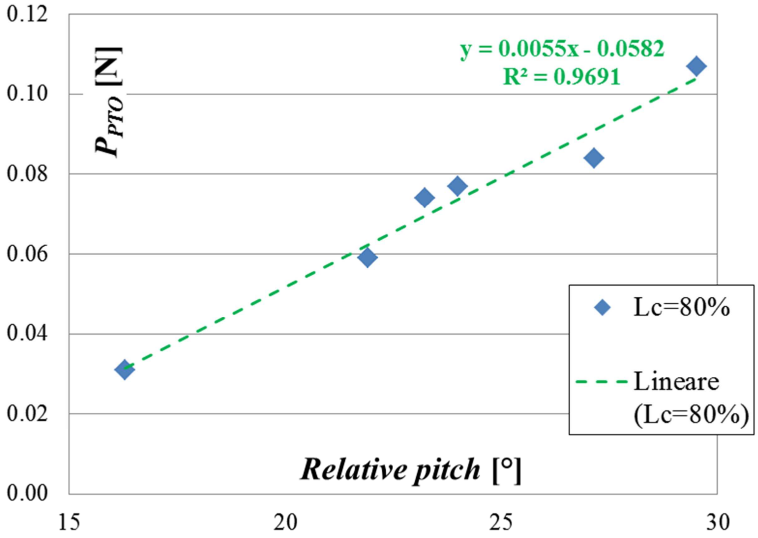

Figure 8.26 – *Linear relation between the relative pitch angle and P_{PTO}.*

Figures from 8.27 to 8.29 report the translation motion by varying the wave obliquity for surge, heave and sway respectively. All the translations tend to increase by increasing the wave obliquity especially for higher WSs (i.e. l/L_P<0.5). This result confirms previous visually observations done during the first experimental activity. The wave obliquity effects is more evident –as expected– for the sway motion, i.e. the greater β the greater the motion, regardless the l/L_P values.

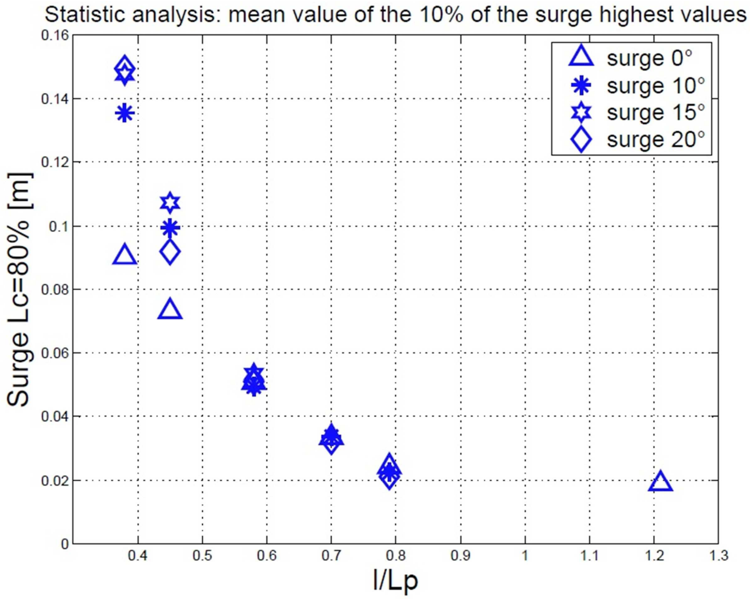

Figure 8.27 – *Surge statistical values by varying the wave obliquity.*

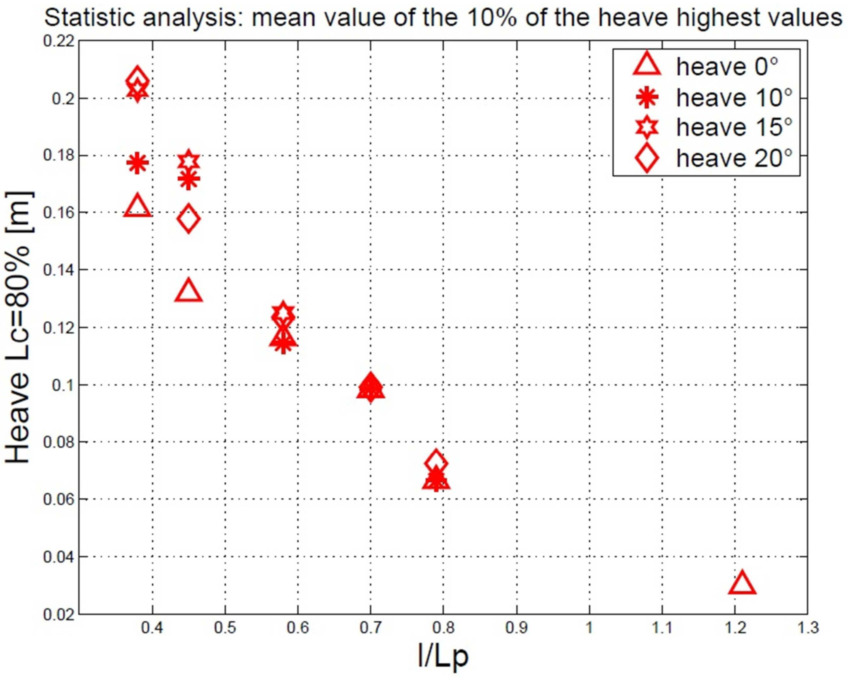

Figure 8.28 – *Heave statistical values by varying the wave obliquity.*

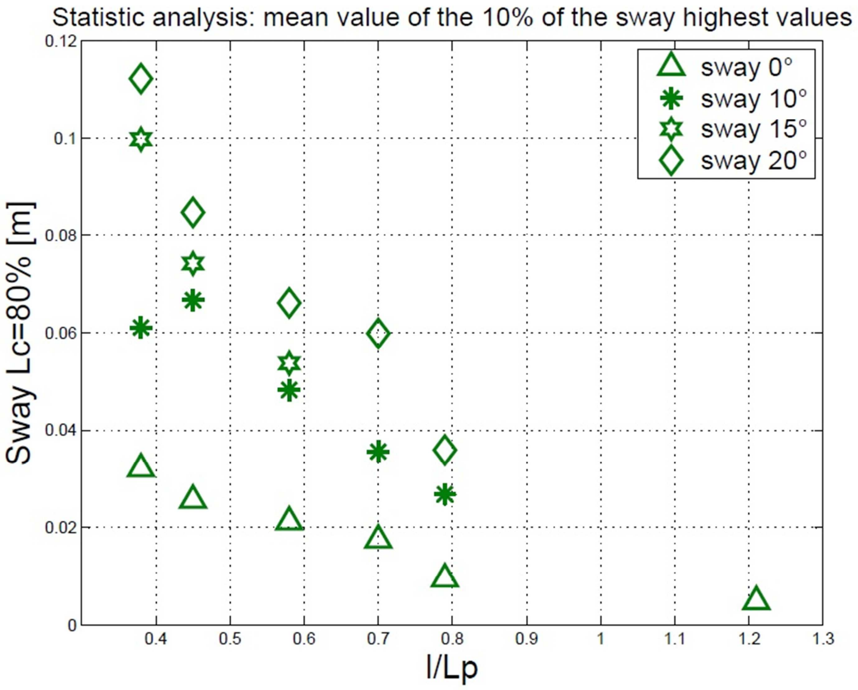

Figure 8.29 – *Sway statistical values by varying the wave obliquity.*

For l/L_P=1.21 both translations and rotations have the minimum value (see Fig.s 8.24 and 8.25) and appear to be substantially independent from L_C. Since the motions and the dissipations have a minimum, it could be explained why for this situation the device performance is the highest among the tested conditions (see Fig. 8.16). However there is only one test for $l/L_P>1$, therefore a general conclusion cannot be drawn, even if this results is confirmed by the results of the first experimental investigation.

In order to evaluate the maximum motion, the free decay tests were performed. The analysis of the device natural periods (for each movement) is important to assure the device survivability, because at the resonance condition the device displacements –and therefore the loads on the mooring system– significantly increase.

The free oscillating tests were performed in absence of incident waves (generated by the wave-maker), by applying an instantaneous displacement along each direction, keeping the system in place for few seconds and then releasing it. During this procedure, the displacements were continuously recorded by the two MTi.

Table 8.14 reports the natural periods T_N, in particular the first six motions are directly derived by the front MTi sensor, whereas the T_N of the relative pitch angle is derived considering the difference between the two MTi for the pitch motion. The value of T_N for this motion can be assessed as 0.5s, however due to noise its reliability should be proved by further tests.

Each natural mode usually is affected by and affects a specific component of the device. For example, the surge and yaw modes are affected by the mooring dynamics, whereas pitch and heave are mainly driven by the geometry and by the PTO loads. The table 8.14 indeed highlights two main ranges of T_N: around 7s for surge and yaw, and around 0.5s for pitch and heave. Therefore, for example, to optimise the power production the device should operate in a wave climate characterised by wave period around 0.5s in 1:60 scale, a conditions that includes the presence of very short and steep waves.

Motion	Natural Period T_N [s]
Surge	7.14
Heave	0.53
Sway	Not recognisable
Roll	0.54
Yaw	7.47
Pitch	0.50
Relative Pitch	0.50

Table 8.14 – *T_N of the device. Two main ranges can be noted: around 7 and 0.5s.*

Among the tested WSs, WS n.1 (with T_P=0.72s and l/L_P=1.21) is the closest to the T_N value of the pitch motion. Figure 8.16 reports the trend of the device efficiency η, which achieves –as expected– the maximum value in correspondence of the WS n.1.

It is worthy to remark that the typical operation range of the laboratory paddle system is for waves with $0.7 < T_P < 2$, therefore it was no possible perform test with $T_P=T_{N,PITCH}$.

8.3. PRELIMINARY CONCLUSIONS

The second experimental investigation allows to assess several outputs, for example it confirms the importance of the parameter l/L_P not only for the hydrodynamics around the devices, but also for the device motions and power production.

Minimum distances among the devices of a farm, could be derived from the hydrodynamic measurements, in particular it has been highlighted that in the main direction of the incoming waves there should be at least 2*l*, where *l* is the device length, whereas in the perpendicular direction the optimal distance –in accordance with the spread mooring system– is 5*b*, where *b* is the device width.

Furthermore from the motions measurements it was possible to assess ranges of wave periods able to optimises the power production (i.e. considering the pitch natural period) or to have indication on the mooring design (if it is considered the surge natural period). Furthermore for the mooring design particular interest is the displacements-loads relation including ordinary and extreme WSs, which is a not linear curve (see Fig. 8.30).

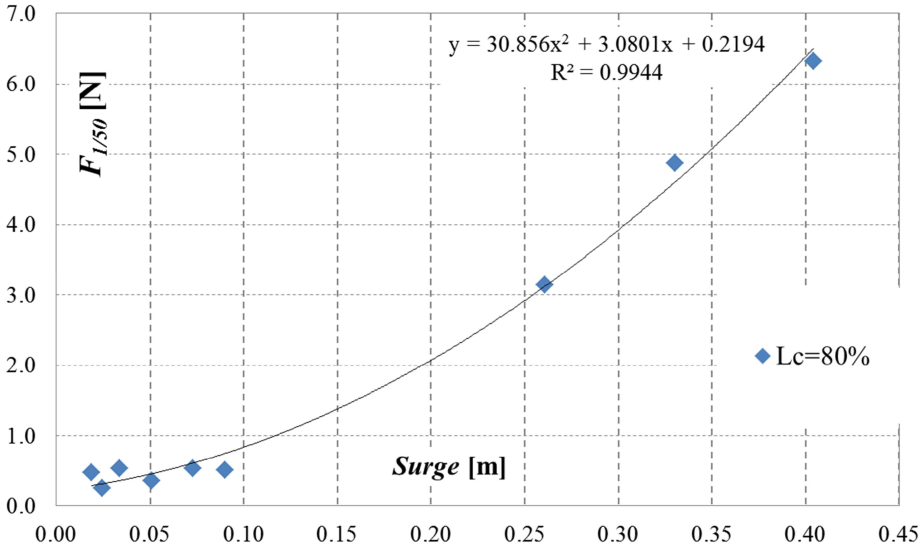

Figure 8.30 *– Relation between the device surge motion and the forces acting on the mooring lines under ordinary and extreme WSs performed with L_C=80%.*

PART B - NUMERICAL MODELLING

The numerical modelling allows to confirm and, at the same time, extend the experimental database. Two main commercial software were chosen: MIKE 21 BW (i.e. the Boussinesq Wave module), developed by DHI Water & Environment & Health and ANSYS-AQWA developed by ANSYS. MIKE 21 BW allows to completely consider all the hydrodynamic processes (run-up, shoaling, refraction, reflection, diffraction, transmission, etc.), whereas AQWA allows to include aspect such as the mooring system and is able to model floating moving structures. This chapter reports the numerical activities carried out with the two models mentioned above, in terms of calibration and main results.

9. MIKE 21 BW INVESTIGATION

The main activity performed implementing MIKE 21 BW is related to the first experimental configuration. However some parameters (especially the beach reproduction) have been analysed using the second experimental investigation.

The numerical parameters of the code were opportunely calibrated in order to reproduce the same effects of the laboratory tests and to forecast the device performance in different wave conditions. In particular, the hydrodynamics around a farm of multiple floating WECs has been investigated at the same experimental points, and its elaboration specifically focused on the wave transmission and device wave interaction. Furthermore with the numerical simulation it is also possible to obtain 2D maps, e.g. of H_S and of the disturbance coefficient (K_D) defined as the ratio between the local and the incoming H_S.

The farm under exam is composed by three devices in a staggered layout and in 1:60 scale. The performance of the farm module is analysed under a variety of ordinary irregular WSs and accounting sea level rise variations (see Tab. 7.1), at intermediate depth condition (being $1/20<h_{max}/L_0<1/2$) and with the incoming wave direction aligned with the main axis of the devices, i.e. only 0° wave direction have been examined for the two water depths. The staggered farm configuration is composed by two devices in the first line and one in the second line at the centre of the first gap line. The gap width is approximately $8b$, while the cross-shore distance among the devices is about $2l$.

The release version of this model was based on the numerical solution of the enhanced Boussinesq equations (i.e. the validity is extended also for small wave period) formulated by Madsen and Sørensen (1992) and their updates related to the wave breaking and moving shoreline (Madsen et al, 1997; Sørensen et al, 1998; Sørensen and Sørensen, 2004; Sørensen et al, 2004).

9.1. NUMERICAL SET-UP

The main parameters are report in the following list.

1- Wave Module

MIKE 21 BW includes two modules: the 1DH and 2DH Boussinesq Wave Module. The first module, i.e. one horizontal space co-ordinates, solves the enhanced Boussinesq equations by a standard Galerkin finite element method with mixed interpolation for variables defined on a grid. The 2DH BW, i.e. two horizontal space co-ordinates, solves the enhanced Boussinesq equations by an implicit finite difference technique with variables defined on a space-staggered rectangular grid. The hydrodynamics induced by the WEC farm is represented with the 2DH BW module.

2- Bathymetry

The numerical bathymetry corresponds to an extended version of the wave basin, to reduced boundary effects. The bathymetry was created through a xyz AutoCAD file that exactly reproduced the basin and the beach.

A first attempt of the bathymetry included the floating device as a structure, therefore with a change in bathymetry in their correspondence, but with this configuration the simulation always aborted due to stability problem. Therefore a second attempt was analysed, where there is no bathymetry difference in correspondence to the space occupied by the devices.

In order to guarantee a good accuracy and numerical stability, a space high-resolution grid was selected. The grid spacing in both cross-shore (i.e. direction of wave propagation) and long-shore direction was equal to 0.05 m.

MIKE 21 BW implements as numerical parameters for the space discretisation of the convective terms four alternative, the results reported in this report were obtained using the central differencing with simple up-winding at steep gradients and near land.

3- Deep terms

The deep water terms, included in the enhanced Boussinesq equations, allowing to extend the model into deeper water and/or smaller wave period. In the tested configuration the wave breaking is not include, and h_{max}/L_0 is often lower than 0.22, hence the classical Boussinesq formulation (deep water terms excluded) has been chosen.

For the smallest wave periods (i.e. h_{max}/L_0=0.40) the comparison among simulations run both with the classical and with the enhanced Boussinesq equations shows in the latter case lower incident wave energy spectra and lower wave heights along the basin. Moreover the model requires more CPU time, therefore all the results here presented were obtained from simulations run with the classical formulation.

4- Bottom friction effects

Usually the effects of bottom friction are relatively important if there is a sufficient distance for the bed resistance to attain any significant effect on the wave propagation. In the configuration under exam the bottom friction was included by means of a constant Manning number of 40 $m^{1/3}/s$ for the concrete bottom, of 30 $m^{1/3}/s$ for the devices and a varying Manning number between 40 and 20 $m^{1/3}/s$ was adopted for the beach (see Fig. 9.1).

Furthermore an eddy viscosity coefficient with a constant value of 0.5 in all the grid was added. However the presence or the variation of the eddy viscosity value does not seem so influent on the simulation results.

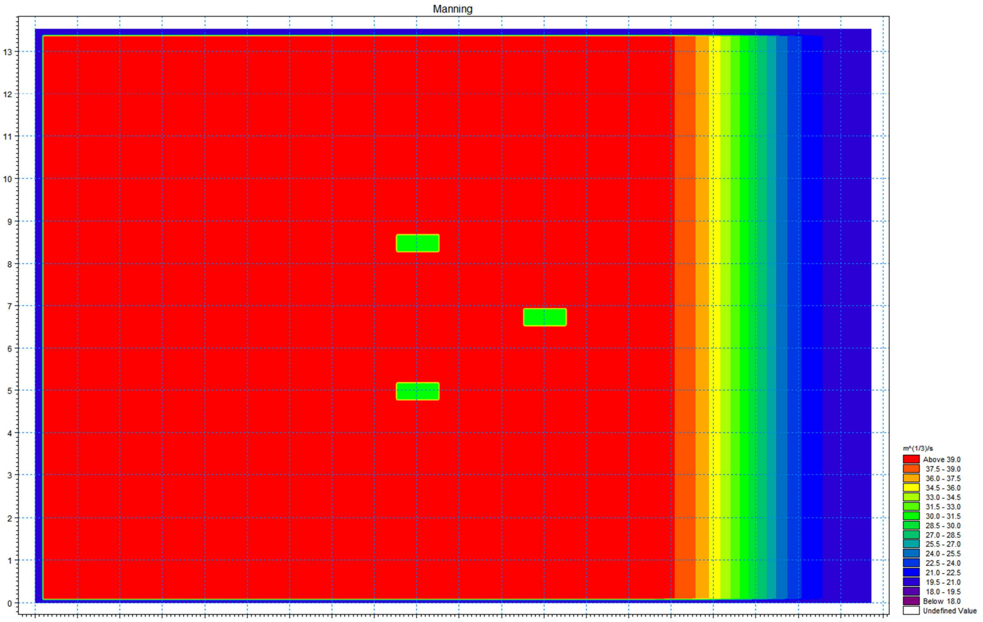

***Figure 9.1 –** Final configuration of the bottom friction effects used in MIKE 21 BW.*

5- Simulation period and wave generation

The minimum wave period (i.e. T_P=0.74s) was resolved by more than 35 time steps (i.e. $T_{min}/3$) since the moving shoreline was included. Therefore the calculation time step of 0.01s was chosen. Each simulation had a duration of 20 minutes. The output was post-processed to achieve the same sample frequency used in the laboratory.

The released software MIKE 21 BW includes itself a Model Setup Planner. This Model Setup Planner gives an estimation of the required total time for the simulation, the maximum value for the optimization of the spatial discretization, the suggested minimum wave period allowed, having as input parameters such as the model extensions, the water depth, the spectra peak wave period, etc. Following the set-up planner suggestion, the chosen discretization parameters fulfil the Courant criterion, i.e. C_R<1.00.

Once the smallest wave period allowed is known, the waves are generated through an internal Toolbox. The MIKE 21 Toolbox – Module waves – Random Wave Generation was used. This toolbox permits the choice of several wave spectrums and it accepts as input significant wave height and period, directionality, water depth, smallest wave period, grid spacing and line where apply the waves. The simulations were performed by imposing measured water levels or target Jonswap wave spectrum at the off-shore boundary. The results seem to not strongly feel the effect of the different choice in the wave generation.

6- Filter layer

In MIKE 21 BW it is possible to insert a local filter layer in order to remove high-frequency instabilities during up-rush and down-rush and to dissipate the wave energy in the area where the surface roller cannot be resolved. Since the simulations were stable and the wave breaking was not included, the filter was not been applied to the simulation.

7- Porosity layer

Porosity values are used to model partial reflection and/or transmission through structures. The width of the porosity layer should be at least 1/4 of a wave length corresponding to the most energetic waves. In the simulations, the three floating devices were reproduced as porous layers, in order to simulate wave transmission and reflection through them. Since the code is 2D and not 3D, parameters –as the draft– are not important, and the layer had the same characteristics from the bottom to the surface, thus the device is a porous pile extended for all the water depth.

The selection of the value to be attributed to the porous layers, i.e. the so called porous factor, has been derived from an iterative procedure.

The internal Toolbox of MIKE 21 –Waves- Calculation of reflection coefficient, allows to obtain the value of this factor depending on the water depth, the wave conditions, the width and permeability/impermeability of the layer and on the typical diameter of the stones.

The porous factor proved to be the key design and calibration parameter. After several attempts, in order to optimise the representation of wave transmission, a porous factor of 0.90 has been selected, having the width layer equals to 1m, stone diameter equals to 0.05m and the other parameters (laminar and turbulent resistance parameters) equal to their default values. In the porosity map, the porosity factor is different (and in particular less) than one only along bodies where it is expected dissipation effect.

To reduce the wave reflection induced by the beach a second analysis on the porosity map was performed in a later phase. The main difference in the beach representation is related to its permeability/impermeability (i.e. without the porous layer the beach is assumed as impermeable).

8- Sponge layer

Sponge (or absorbing) layers can be used as numerical wave absorbers in Boussinesq wave simulations. These may e.g. be set up along model boundaries to provide radiation boundary conditions, which absorb wave energy propagating out of the model area.

In the numerical tests, to assure full wave absorption behind the numerical wave-maker a sponge layer of 50 cells has been created. The assigned sponge values are obtained, as for the porosity factor, through an internal Toolbox. The set-up of the sponge layer fulfilled the provided guidelines (MIKE BW User guide), for instance: the sponge layer width should be one/two times the wave length corresponding to the most energetic waves; sponge layers should be at least 20 lines wide (but 50 are suggested); to minimise reflections, the values of the sponge layer coefficients increase smoothly towards the boundary/land.

The whole set-up configuration is summarized in the following figure.

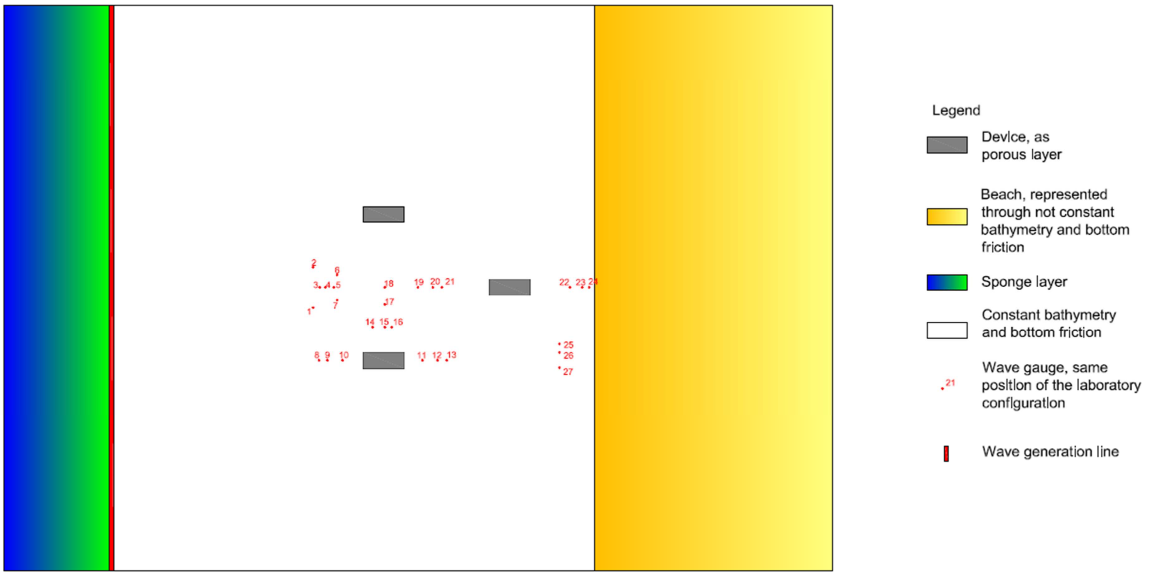

***Figure 9.2** – Summarizing of the setup used in MIKE 21 BW.*

9.2. CALIBRATION

The numerical parameters were calibrated by comparing the numerical and the experimental results. The main model outcomes are e.g. the time series of the surface elation, the significant wave height and the disturbance coefficient in the entire grid. The calibration focused on data elaboration on the frequency domain.

A first comparison was related to the estimation of the overall wave energy, in terms of 3D wave energy spectrum obtain through the BDM analysis applied to the same first 7 WGs as in the elaboration of the experimental data.

Figure 9.3 reports the comparison among experimental and numerical 3D wave energy spectrum (i.e. considering both wave frequency and direction) for the WS n.6. For several WSs, the spectrum has a greater spreading factor in the laboratory than in the numerical simulations, both in frequency and direction. As it will be shown later the approximation of measured and simulated K_T is overall good; however a different spreading could lead to a different H_S distribution in the wake of the devices and therefore would be worthy of further investigation.

In order to better investigated the effect of the wave reflection, incident and reflected 2D spectrum were derived from the frequency analysis domain at the groups of three aligned WGs in front the wave maker and along the basin.

As regards the wave generation, the numerical model is able to predict the incident wave energy at the WGs 8-9-10 (see Fig. 9.4), being the energy difference at the peak frequency on an average of the 3%. The worst case, leading to a difference up to the 18%, corresponds to the lower WS, i.e. WS nr. 2, where problems in generation may have occurred due to physical wave-maker limitations.
This behaviour is notable both when wave generation is forced with the measured water levels and when the target Jonswap wave spectrum is selected, regardless the water depth, and therefore only results related to h_1 are graphically reported.

Regarding the reflected wave energy, instead, the model overestimates the lab values at least of 2.5 times (see Fig. 9.5). A possible solution for reducing wave reflection may be a different representation of the beach dissipation in the model.

These differences are also confirmed by K_T and K_R, in fact table 9.1 reports their values and –to facilitate the comparison– also the experimental values of table 7.3. It is possible to note that numerical and experimental data sets have the same trend in function of l/L_P, i.e. by increasing l/L_P, sets of K_R tend to increase whereas sets of K_T have the opposite trend. Furthermore table 9.1 highlights that $K_{R,LAB}$ is in the range 16-34%, $K_{R,NUM}$ instead varies in a wider range 27-70% (e.g. for h_1), whereas the average K_T values differ for less than the 3.5% for K_{T1} and 7% for K_{T3} (e.g. again for h_1).

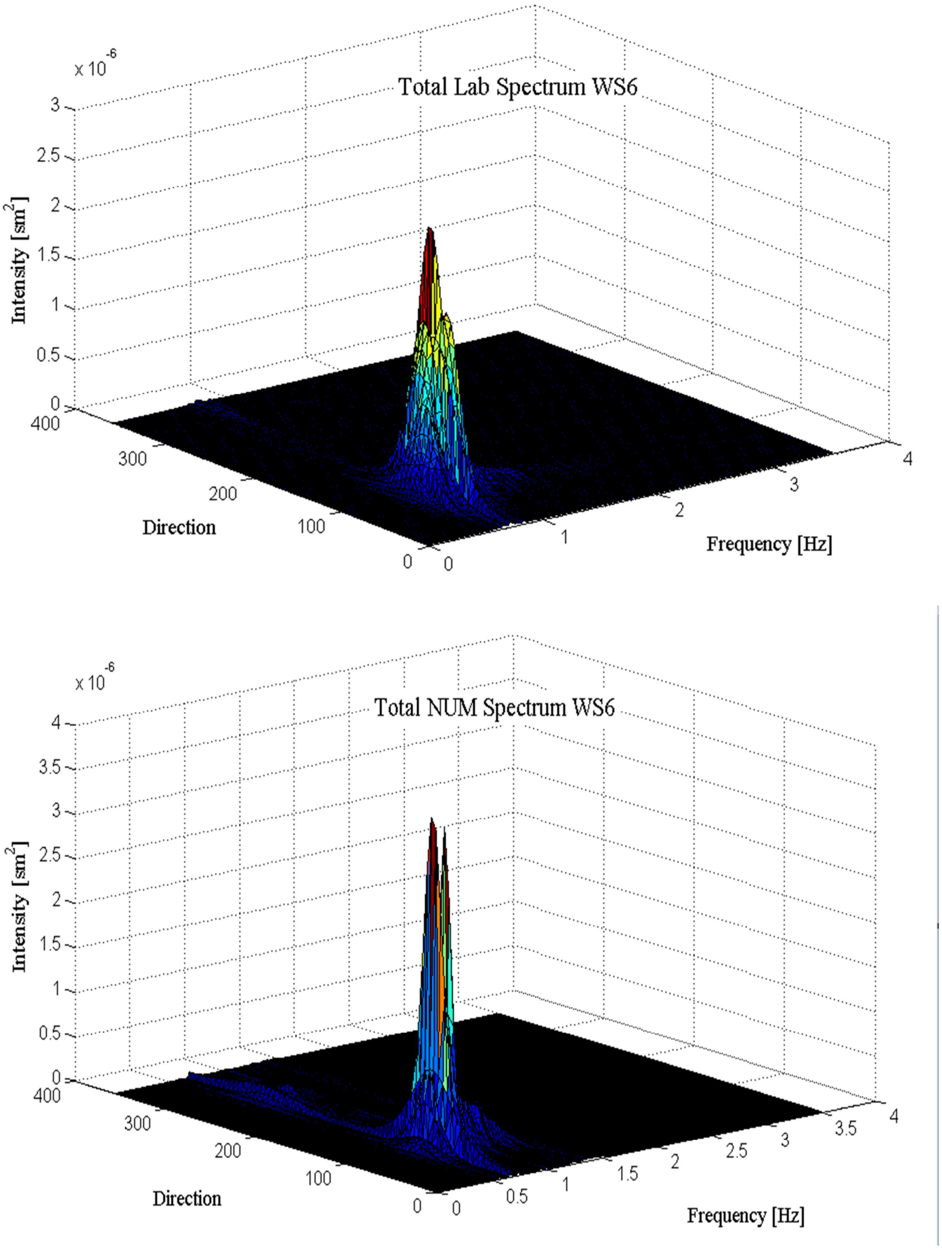

Figure 9.3 – *3D wave energy spectrum for the WS n.6 for the laboratory tests (on the top) and for the numerical simulations (on the bottom).*

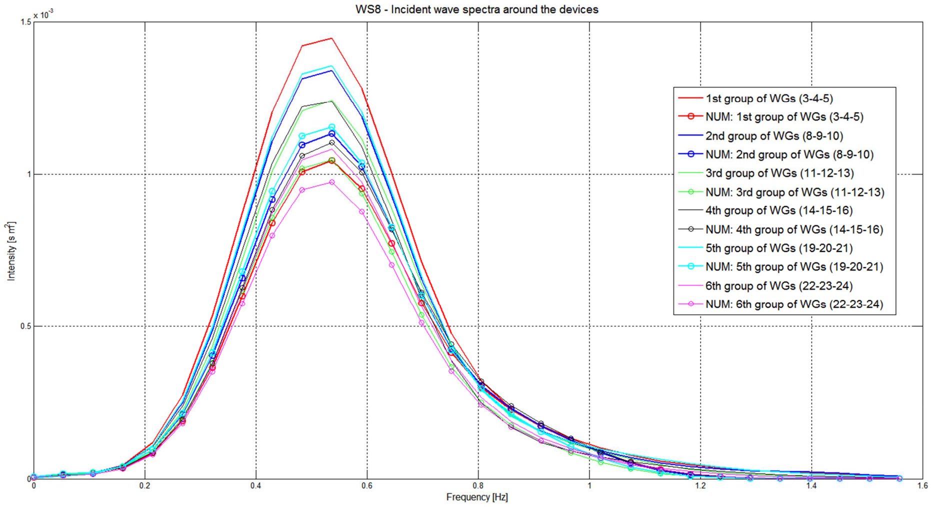

***Figure 9.4 –** Example of laboratory and numerical 2D incident energy spectrum for the WS n.8 at the water depth h_1, frequency in the x-axes, and energy distribution in the y-axes.*

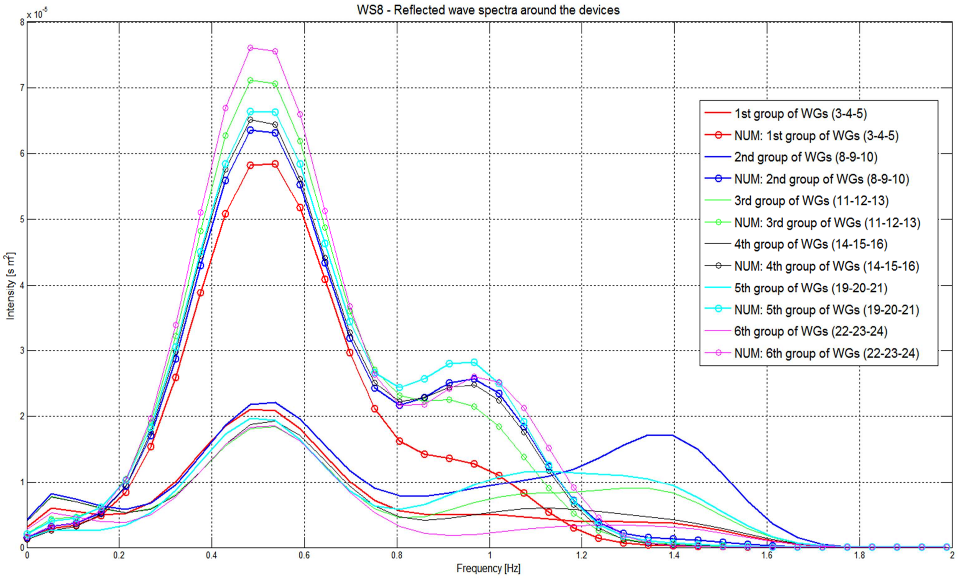

***Figure 9.5 –** Example of laboratory and numerical 2D reflected energy spectrum for the WS n.8 at the water depth h_1, frequency in the x-axes, and energy distribution in the y-axes.*

Analogous to the wave energy spectra, the greater differences –between the laboratory and the simulation– in the values of K_R with respect to the values of K_T could be mainly related to a different representation of the dissipation induced by the beach.

WS	**1**	**2**	**3**	**4**	**5**	**6**	**7**	**8**
$K_{T1,\,LAB}$	0.88	0.96	0.97	0.97	0.97	0.97	0.99	0.96
$K_{T1,\,NUM}$	0.82	0.90	0.94	0.97	0.93	0.96	0.92	0.95
$K_{T3,\,LAB}$	0.94	0.97	0.95	0.95	0.92	0.91	0.92	0.89
$K_{T3,\,NUM}$	0.82	0.86	0.92	0.96	0.90	0.94	0.89	0.92
$K_{R1,\,LAB}$	0.32	0.28	0.23	0.18	0.23	0.18	0.25	0.19
$K_{R1,\,NUM}$	0.53	0.41	0.39	0.39	0.35	0.38	0.32	0.27
$K_{R3,\,LAB}$	0.34	0.28	0.21	0.17	0.20	0.16	0.22	0.17
$K_{R3,\,NUM}$	0.70	0.48	0.44	0.39	0.39	0.38	0.36	0.28

***Table 9.1** – Experimental and numerical K_T and K_R under 3D perpendicular WSs with h_1.*

Regarding the wave transmission, figures 9.6 and 9.7 report their values for the two water depths at installation, from which it is possible to appreciate that in the numerical simulation h seems not to significantly affect K_T. The higher differences are related to the back device (see Fig. 9.7 with K_{T3}) due to a different wave height distribution along the gap of the first line and so different representation –in the model– of the mutual interaction among the devices and different wake effects acting on this third device (see next sub-section 9.3). In particular figure 9.7 shows that $K_{T3,NUM}$ is higher than $K_{T3,LAB}$, the reason is related to the device motion and to its placement, i.e. in a sheltered area induced by the wave interaction of the two first line devices, and this interaction is not well reproducible with the numerical simulation.

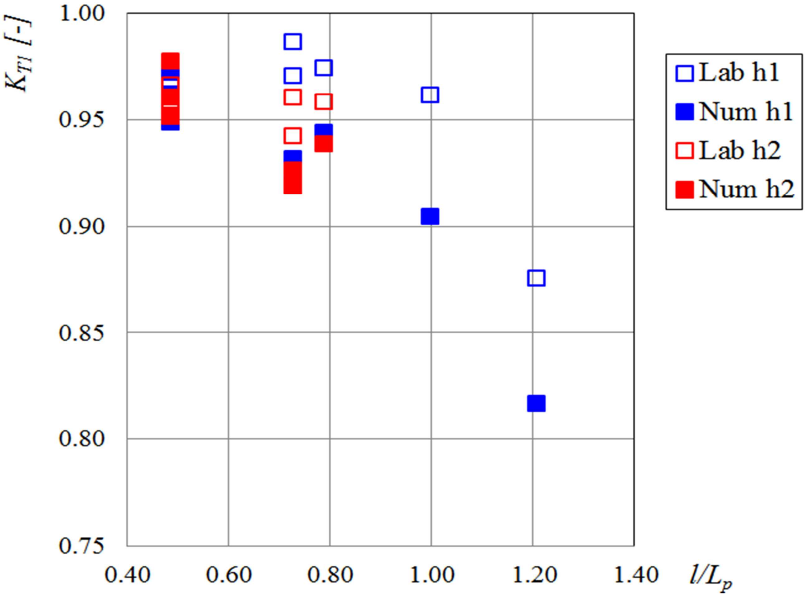

***Figure 9.6** – K_{T1} from the laboratory and numerical data and for the two water depths.*

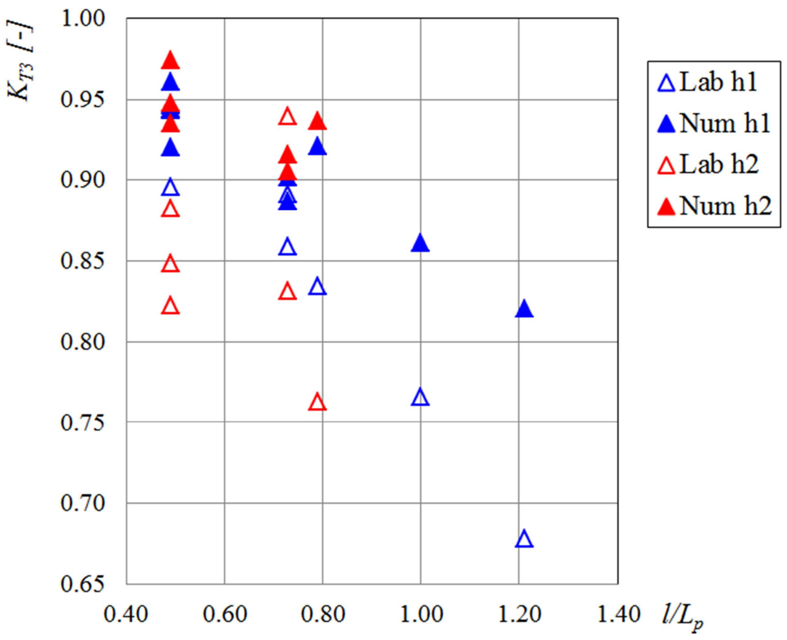

Figure 9.7 *– K_{T3} from the laboratory and numerical data and for the two water depths.*

However the numerical results can be used to validate laboratory hypothesis made on the wave transmission behind the lines of a wave farm, which were based on simplified assumptions on measurements dealing with local values. As reported in the section 7.2, the K_{T2} values are obtained through a weighted average considering constant the K_{T1} values for the space occupied by the devices and their anchors, and a value equal to 1.00 (i.e. total transmission) for the remaining basin zones. K_{T4}, instead, is derived in a similar way, by replacing the K_{T3} value in the space in between the anchors of the third device. The approximation to keep constant the transmission coefficient for a long-shore extension equals to the space between the anchors was based on the measured trend of H_S at WGs n. 22-25-26-27.

In order to check these assumptions, numerical results are extracted along two long-shore lines, covering the whole long-shore extension of the experimental tank. Figure 9.8 reports this comparison.

Figure 9.8 shows for WS n. 2 a good match among the presumed laboratory trend and the grid by grid K_T values, derived from the simulations. Both the effects of wave interaction at the gap (values greater than 1) and the reduction of wave height induced by the devices can be appreciated.

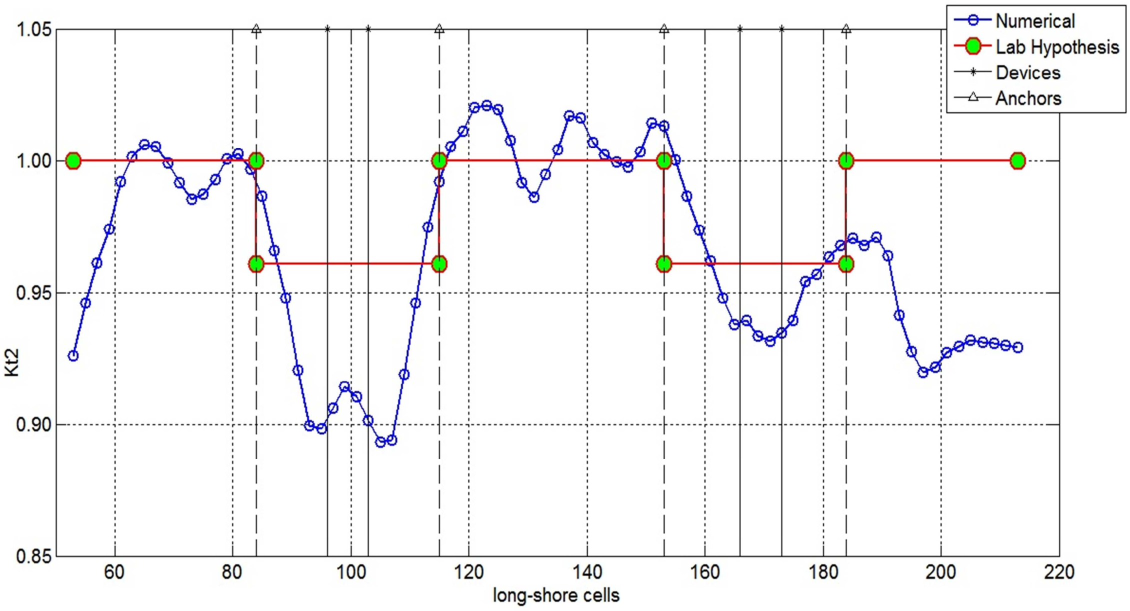

Figure 9.8 *–K_T behind the first farm line for the WS n.2;*
in red: laboratory hypothesis; in blue: numerical results.

Furthermore, figure 9.9 compares the lab and numerical values of K_{T2} and K_{T4}. To derive single values of $K_{T2,NUM}$ and $K_{T4,NUM}$, the results from simulations have been averaged along the extraction line.

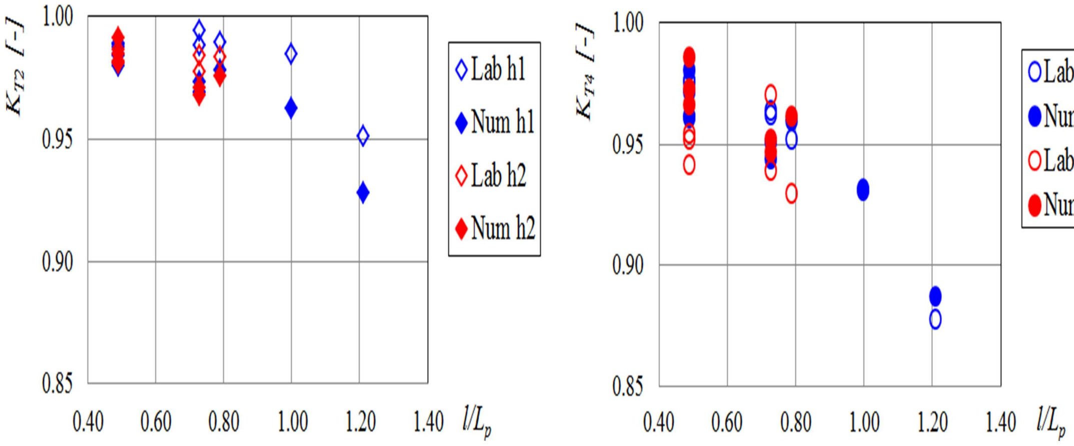

Figure 9.9 *– Numerical and laboratory values of K_{T2} and K_{T4} in the left and right side respectively.*

9.3. NUMERICAL RESULTS

The numerical results have been based on the H_S values along the basin, in particular in the gap between the two first line devices and in the wake of the rear device of the second line. Table 9.2 summarises the H_S value at each WG for the WSs performed with h_1 in full scale. The numerical H_S along the basin are close to the experimental ones (see Tab. 7.4) with the exception of the values related to the WGs within the gap (see next figures). The reason of the differences in the gap is due to the device motion, since in the numerical simulation the device is modelled as a fixed body (a porous pile with rectangular section). Also the different incoming wave spreading leads to a different wave height distribution in the wake of the devices.

Besides, from table 9.2 and figure 9.10, it can be observed that the numerical wave-maker is more stable than the laboratory one: in fact it is able to reproduce the same $H_{INCOMING}$ by changing T_P also for the less energetic WSs (see WGs n. 1-8 for WSs n. 1-2 in the Fig. 9.10).

	WS							
WG	**1**	**2**	**3**	**4**	**5**	**6**	**7**	**8**
1	1.89	1.97	2.01	2.09	2.71	2.82	3.28	3.42
2	1.87	1.94	1.98	2.10	2.68	2.82	3.25	3.45
3	1.85	1.94	2.00	2.08	2.71	2.82	3.29	3.45
4	1.88	1.94	2.02	2.07	2.74	2.78	3.32	3.42
5	1.84	1.95	1.98	2.05	2.68	2.77	3.26	3.40
6	1.85	1.9	1.93	2.08	2.62	2.81	3.19	3.40
7	1.89	1.97	1.99	2.08	2.70	2.81	3.29	3.40
8	1.91	1.98	2.00	2.14	2.71	2.88	3.29	3.51
9	1.91	1.99	2.03	2.11	2.74	2.84	3.32	3.51
10	1.91	1.98	1.97	2.07	2.68	2.81	3.25	3.39
11	1.6	1.76	1.81	2.00	2.42	2.68	2.92	3.22
12	1.63	1.79	1.92	2.10	2.57	2.82	3.08	3.30
13	1.61	1.82	1.92	2.08	2.56	2.79	3.07	3.35
14	1.89	1.94	1.98	2.06	2.66	2.78	3.20	3.47
15	1.84	1.95	2.01	2.14	2.73	2.86	3.31	3.44
16	1.81	1.94	2.00	2.15	2.70	2.89	3.28	3.46
17	1.86	1.95	2.03	2.07	2.75	2.80	3.33	3.33
18	1.84	1.97	2.06	2.06	2.79	2.77	3.38	3.32
19	1.77	1.88	2.00	2.04	2.68	2.77	3.24	3.43
20	1.74	1.87	1.94	2.12	2.62	2.86	3.20	3.42
21	1.74	1.90	1.98	2.14	2.67	2.90	3.23	3.54

Table 9.2 *– Values of the numerical H_S in full scale under 3D perpendicular WSs with h_1.*
To be continued

	WS							
WG	**1**	**2**	**3**	**4**	**5**	**6**	**7**	**8**
22	1.49	1.71	1.88	2.13	2.51	2.90	3.00	3.16
23	1.56	1.73	1.89	2.16	2.49	2.86	2.95	3.28
24	1.55	1.70	1.73	2.04	2.30	2.62	2.76	3.31
25	1.66	1.84	1.91	2.05	2.54	2.73	3.05	3.40
26	1.69	1.85	1.91	2.04	2.53	2.72	3.05	3.37
27	1.66	1.83	1.88	2.03	2.51	2.70	3.02	3.34

Table 9.2 *– Numerical H_S values in full scale under 3D perpendicular WSs with h_1. Continued*

WG	**3**	**4**	**5**	**6**	**7**	**8**
1	1.65	1.68	2.68	2.76	3.24	3.34
2	1.59	1.65	2.58	2.72	3.12	3.3
3	1.62	1.65	2.62	2.72	3.16	3.31
4	1.61	1.66	2.6	2.73	3.12	3.31
5	1.58	1.66	2.55	2.69	3.08	3.27
6	1.57	1.65	2.53	2.69	3.05	3.27
7	1.62	1.65	2.61	2.71	3.13	3.3
8	1.64	1.69	2.62	2.78	3.15	3.36
9	1.62	1.67	2.6	2.73	3.14	3.33
10	1.65	1.64	2.63	2.7	3.15	3.27
11	1.48	1.63	2.36	2.6	2.81	3.12
12	1.52	1.63	2.42	2.63	2.89	3.16
13	1.54	1.63	2.44	2.64	2.92	3.17
14	1.62	1.68	2.61	2.74	3.14	3.31
15	1.63	1.7	2.63	2.78	3.16	3.38
16	1.62	1.71	2.62	2.79	3.17	3.39
17	1.61	1.65	2.59	2.7	3.13	3.27
18	1.62	1.64	2.61	2.68	3.15	3.25
19	1.59	1.66	2.58	2.72	3.11	3.3
20	1.56	1.67	2.52	2.72	3.04	3.3
21	1.59	1.69	2.56	2.77	3.08	3.36
22	1.54	1.64	2.41	2.58	2.87	3.09
23	1.53	1.57	2.42	2.48	2.89	2.97
24	1.5	1.62	2.36	2.56	2.81	3.07
25	1.57	1.75	2.5	2.81	2.99	3.38
26	1.56	1.74	2.48	2.81	2.96	3.37
27	1.57	1.73	2.48	2.79	2.97	3.35

Table 9.3 *– Values of the numerical H_S in full scale under 3D perpendicular WSs with h_2.*

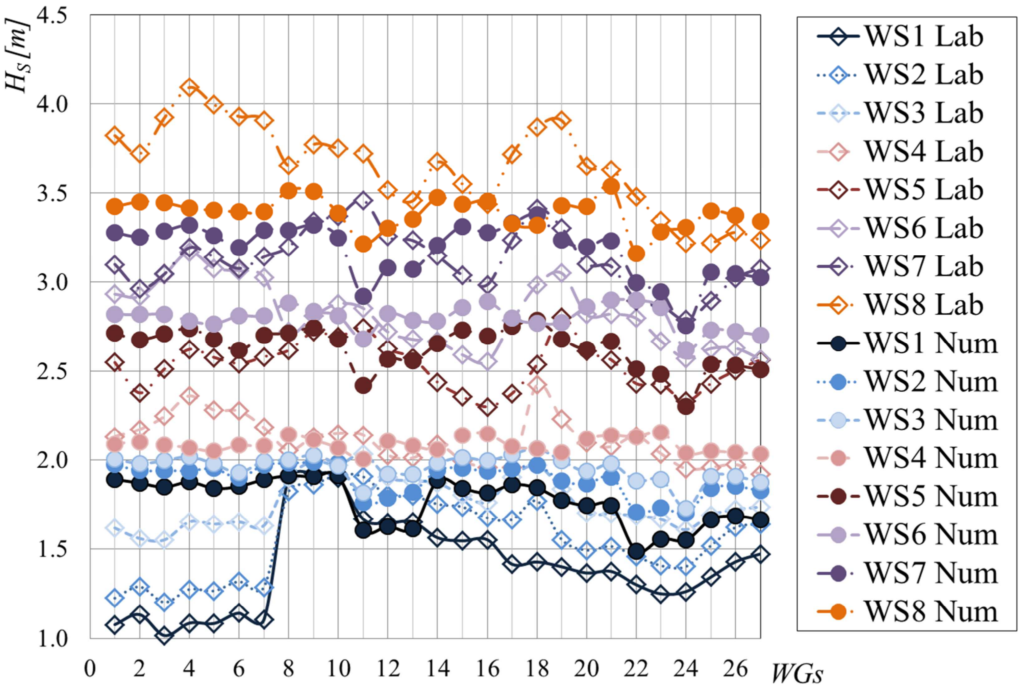

***Figure 9.10** – Comparison of the experimental and numerical H_S recorded in the 27 WGs placed along the basin for the water depth h_1. Values are in full scale.*

For an easier comprehension of the numerical potentials and limitations related to the reproduction of the laboratory results, the H_S values are analysed in the gap, both in long-shore and in cross-shore, and in the wakes behind the farm module.

The long-shore wave interaction can be stated from the measurements at the WGs 15-17-18. Figure 9.11 shows a different numerical and laboratory H_S trend, in fact the laboratory H_S tend to decrease from the centre of the gap towards the device (i.e. from WG 18 to WG 15) while the trend of the numerical values instead seems to be constant, regardless the water depth.

The cross-shore wave interaction is derived from the measurements at the WGs 18-19-20-21. As for the long-shore analysis, even in this case there are differences between numerical and laboratory H_S. In fact, laboratory H_S tend to decrease from the centre of the gap towards the device of the second line (i.e. from WG 18 to WG 21) while numerical H_S instead seems to be constant, regardless the water depth (see Fig. 9.12).

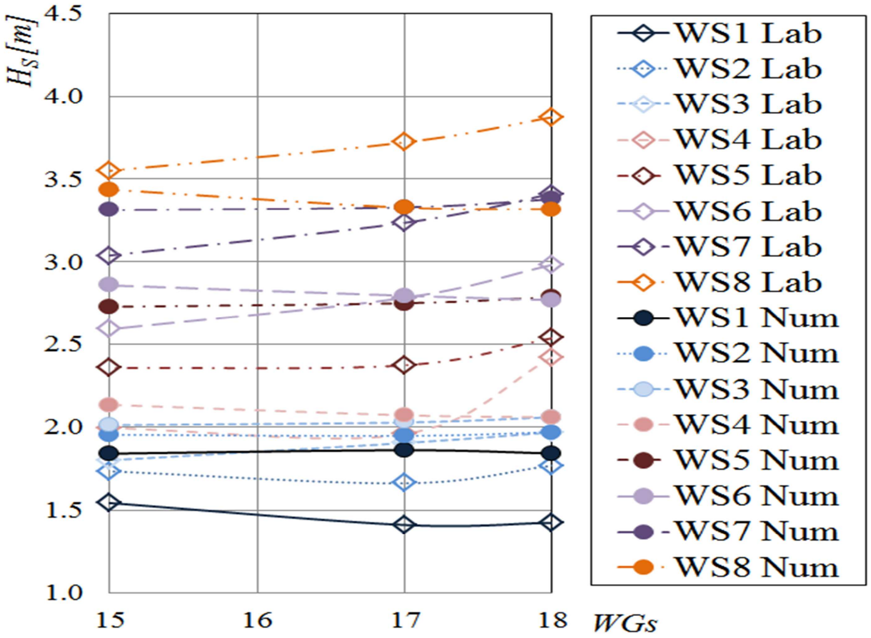

***Figure 9.11** – Numerical and experimental values of H_S in long-shore direction with h_1.*

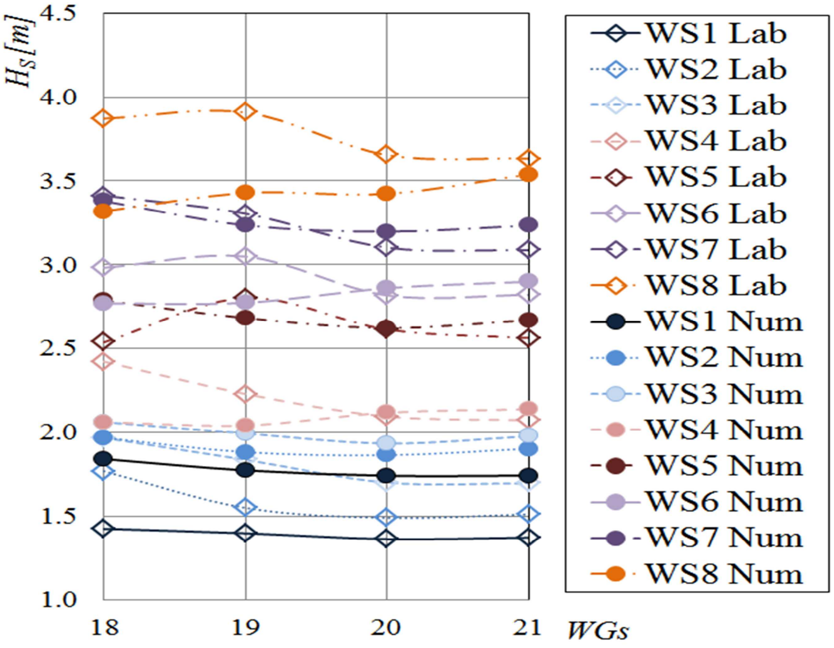

***Figure 9.12** – Numerical and experimental values of H_S in cross-shore direction with h_1.*

Figure 9.13 shows the wave field behind the farm, in terms of H_S related to the WGs n. 22-25-26-27, for every WS with h_1. The comparison shows less difference with respect to the H_S comparison in the gap, this is related to the greater distance from the interaction zone due to the device motion (i.e. the gap of the first farm line).

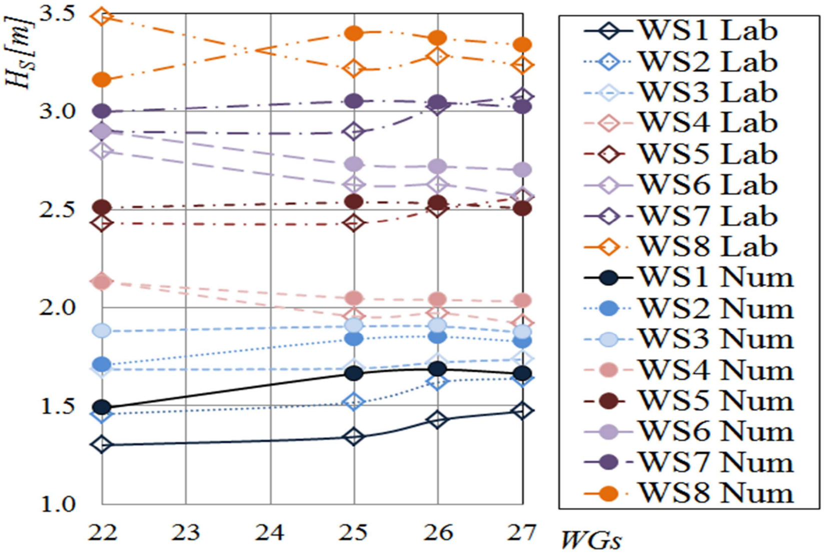

Figure 9.13 *– Numerical and experimental H_S values in the wave farm module wake with h_1.*

9.4. EXTENSION OF THE EXPERIMENTAL DATABASE

Once the accuracy and the limitations of the software are well-known, the numerical simulations allow to extend the experimental database in terms of not punctual results and, at the same time, in terms of further configurations to be examined (at lower cost). In particular this section proposes map results of the disturbance coefficient K_{DIS} defined as the ratio between the local H_S and the incoming H_S and two additional wave farm layouts, obtained by changing two design parameters of the farm layout: the alignment and the distance between the devices. These two additional configurations were carried out for WSs 4-5-7, in order to analyse both the influence of a change in wave height and wave period the numerical tests were.

9.4.1. 2D MAPS

The laboratory hydrodynamic measurements do not allow to completely describe the wave field around the devices, because they give only a local value. With the numerical simulation instead, it is possible to achieve a complete view of the wave farm hydrodynamics, since the hydrodynamic measurements are available in all the cells of the grid.

Figure 9.14 shows an example of 2D maps of KDIS for the WS n. 5 (H_S= 0.067m, T_P= 1.01s) for the water depth h_1. Values from green to blue denote areas where the devices are effective in reducing wave height. Values from yellow to red denote areas where the local wave height is greater than the target; it can be specifically noticed wave reflection in front of the three devices and in some area at the gap (due to the interaction of the devices placed in the first line). The wakes behind the first two devices have an orientation of about 30° with respect to the direction of wave propagation and show an extension greater than the distance between the anchors. The disturbance coefficient varies in the range 0.90-1.04 in the gap and 0.84-0.96 in the device wakes.

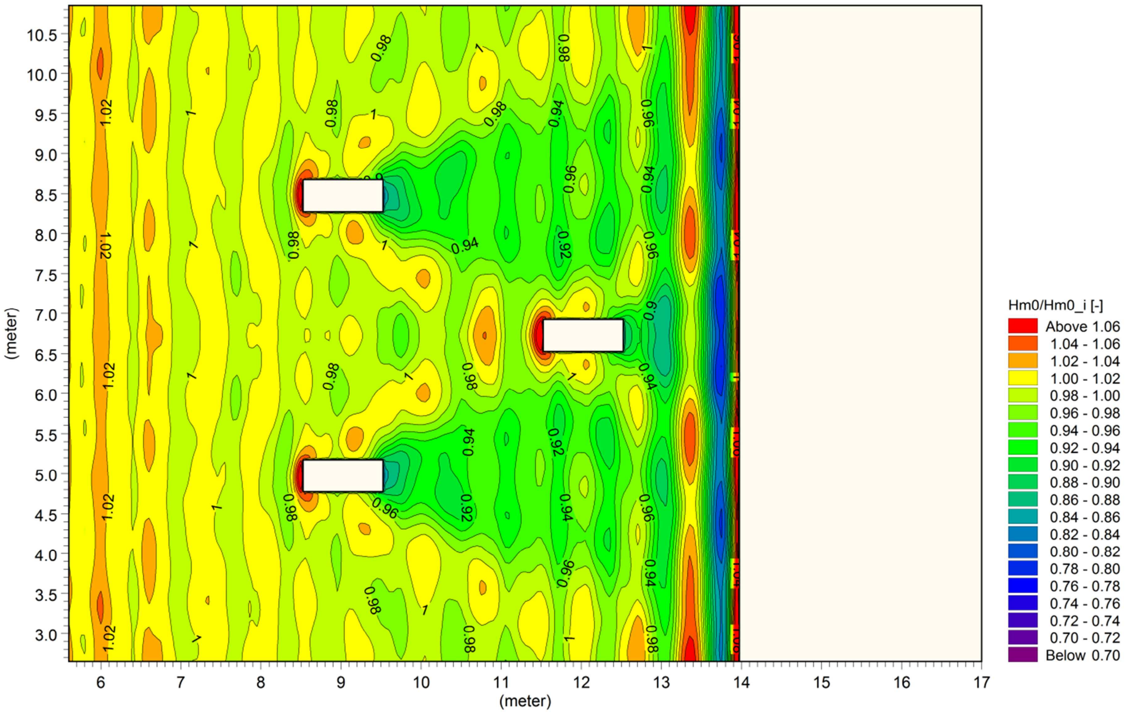

Figure 9.14 – *K_{DIS} for the WS n. 5 (laboratory configuration) after 10 min of simulation.*

9.4.2. DIFFERENT WAVE FARM CONFIGURATIONS

Two design parameters of the farm layout have been selected so far: the alignment and the distance between the devices. In order to analyse both the influence of a change in wave height and wave period the numerical tests were carried out for WSs 4-5-7. The main results are reported below.

The first additional configuration was obtained by changing the placement of the devices in the basic module, i.e. from a three staggered devices to a module with four aligned devices (keeping constant the distance between the farm lines). Furthermore, to compare the results with the initial configuration, the same 27 WGs are used, with the addition of other 3 WGs (WGs 22a-23a-24a) behind the new back device, see figure 9.15.

As expected, the addition of a fourth device in the second line leads to H_S variation only for the WGs between the rear devices and the beach, in fact due to the absence/presence of the device H_S respectively increases at the WGs 22-23-24 and decreases at the WGs 25-26-27 (see Fig. 9.16).

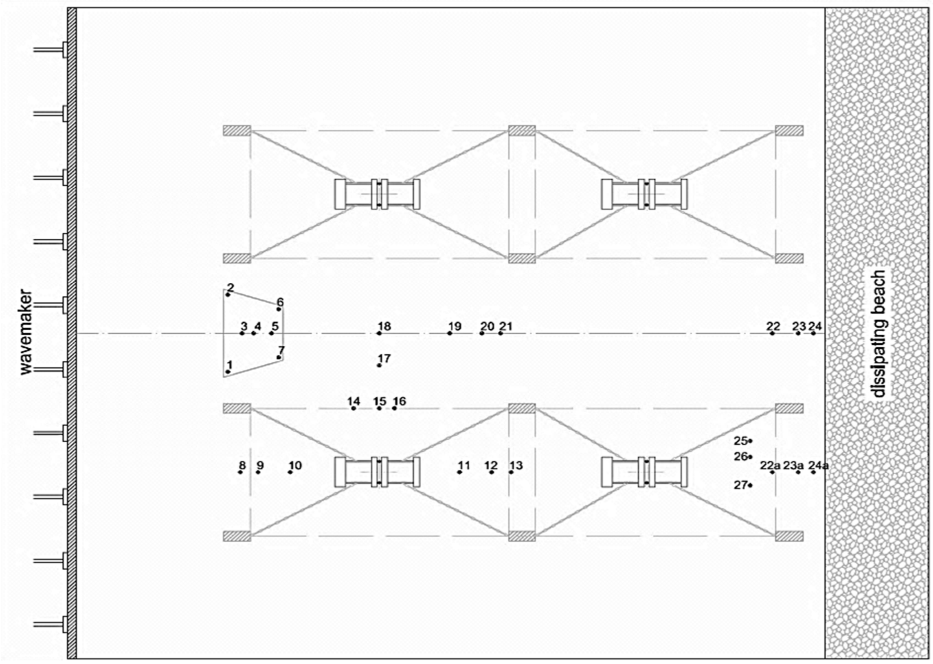

***Figure 9.15** – Aligned configuration with four devices (two for each line) with the same 27 WGs, and 3 further WGs (22a-23a-24a) behind one of the new back device.*

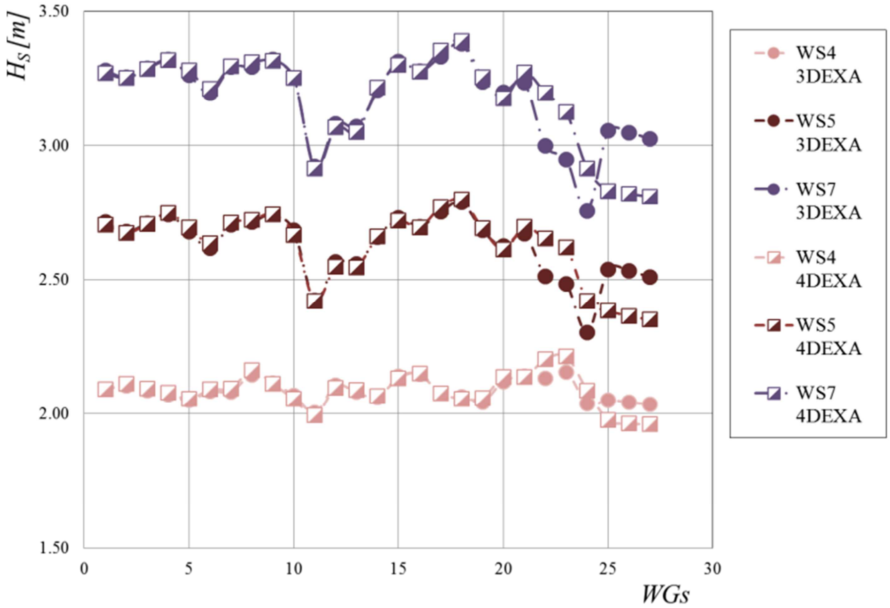

***Figure 9.16** – Numerical H_S at the 27 WGs, derived from the staggered (circles) and aligned (squares) wave farm configuration.*

Figure 9.17 –i.e. the 2D map of K_{DIS}– shows that the back devices fall completely in the wake of the first line and the wakes of the second line are affected by wave reflection from the beach. Therefore the H_S values in front of the back devices and also behind them (and in turns the K_{T3} values) are lower than in the staggered case. However with this new configuration the free area is globally wider and therefore K_{T4} is not so reduced with respect to the staggered configuration. If one considers the combined application coastal protection-energy production, the wave energy available in front of the second farm line is clearly lower.

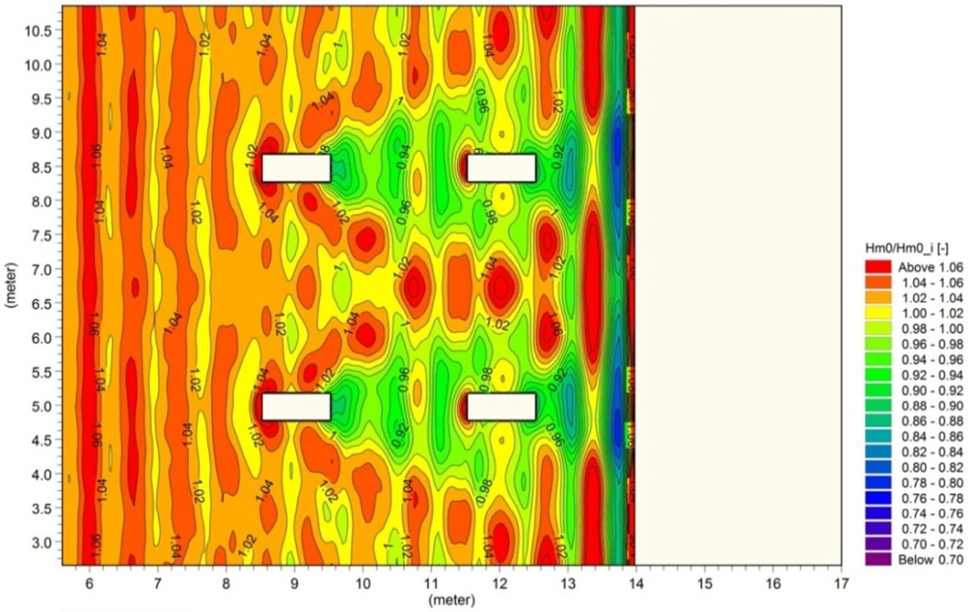

Figure 9.17 – *K_{DIS} derived for the aligned wave farm configuration, after 5 min of simulation.*

The second additional configuration was created in order to examine the influence of the gap width using a staggered configuration. The gap width can be a design parameter able to optimize the combination of coastal protection and energy production. In fact the gap width reduction could increase the number of devices in the farm, i.e. the energy production, and at the same time could decrease the wave height behind the farm exploiting a constructive interaction between the devices in a same farm line.

In the simulation, the gap width has been decreased from 8*b* to 6*b*, keeping constant the cross-shore distance between the farm lines. In order to compare the results with the initial configuration, the same 27 WGs were used, modifying only the long-shore position of the WGs in the gap (WGs 14-17).

This reduction leads, as expected, to modest changes in the H_S recorded in the gap. Figure 9.18 compares the cross-shore (to the left) and long-shore (to the right) H_S values for the two staggered layouts. Along the cross-shore direction the differences are hardly appreciable, whereas H_S is reduced in long-shore direction with respect to the initial configuration especially for the highest WS.

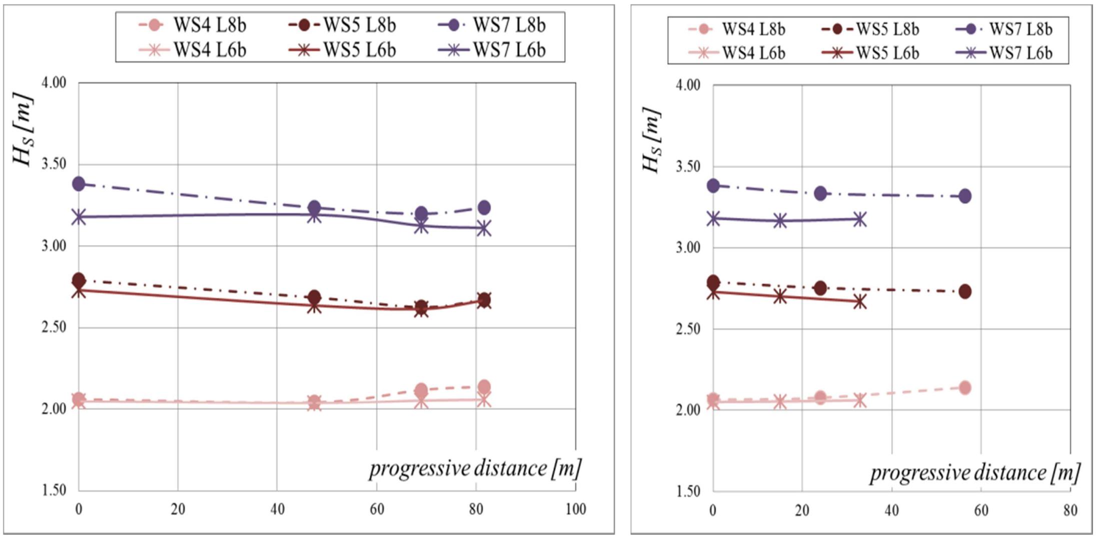

***Figure 9.18** – H_S variations for the two staggered layouts, related to the WGs placed in cross-shore direction and in the long-shore direction respectively to the left and to the right.*

With respect to the wider gap width configuration, with a narrow gap width the back device is more affected by the wake of the front devices (see Fig. 9.19), leading to lower H_S in front of the back device and therefore a lower H_S behind it. Furthermore, it can be also observed again a H_S reduction in the gap (especially in long-shore direction, see Fig. 9.18).

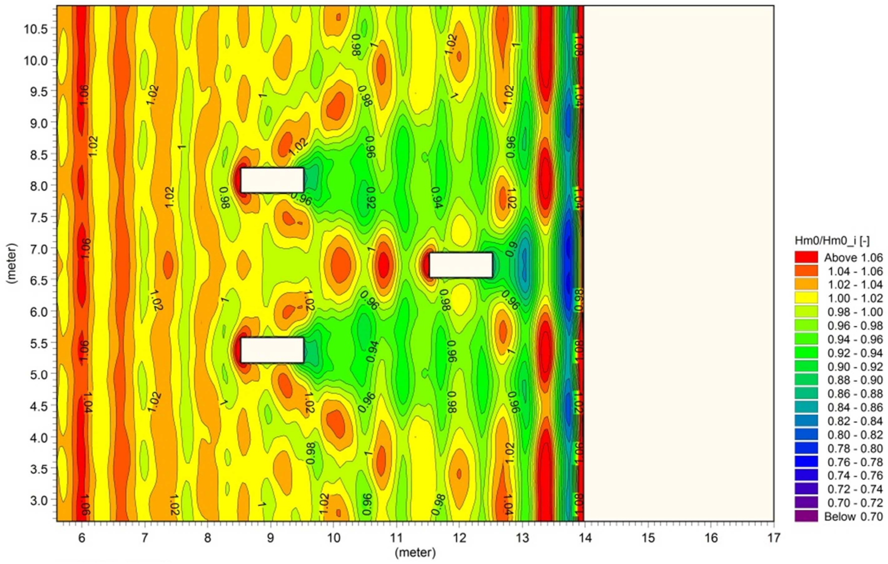

***Figure 9.19** – K_{DIS} derived for the staggered configuration with a gap width of 6b, after 5 min of simulation.*

9.5. PRELIMINARY LAYOUT ASSESSMENT

The selection of the optimal layout depends on the contemporary achievement of a good level of wave reduction for coastal protection and a sufficient level of wave energy still available at the rear lines for energy production purposes. The combination of these results leads to a feasible farm installation. Figure 9.20 reports the H_S numerical values extracted along two long-shore lines (in front and behind the whole farm), for the WS n. 5. The K_{DIS} map comparison coupled with figure 9.20 allow to assess the layout effect on the wave field behind the wave farm module.

In particular, there are slight differences between the two staggered configuration (wider gap width of 8*b* in purple and narrow gap width of 6*b* in orange), and these are related to the gap zone, where a narrow gap width leads to lower H_S. An aligned configuration instead leads to greater H_S reduction only in correspondence of the device (green line vs. purple). Based on the overall analysis of the numerical data, the best configuration for both coastal protection and energy production seems a staggered layout, which also increases the density of the devices.

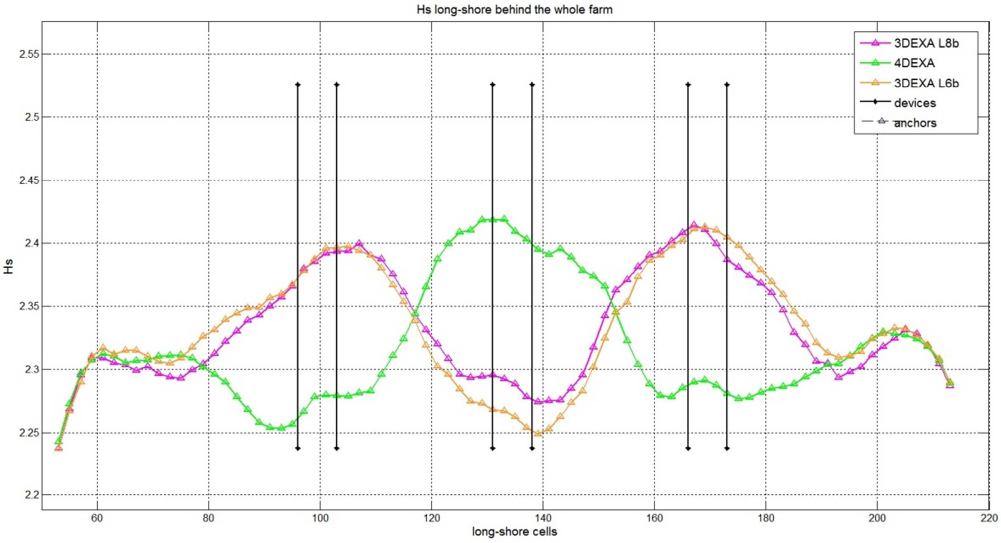

Figure 9.20 – *Numerical H_S in long-shore direction, for the WS n.5, derived behind the whole farm line from the three configurations: staggered with a gap wide 8b (purple), aligned (green) and staggered with a gap wide 6b (orange). The black lines represent the devices positions (e.g. the back device is represented through the central lines).*

9.6. IMPROVEMENT OF THE NUMERICAL SET-UP

The first numerical activity highlighted some weak points, mainly related to the representation of the reflection wave field. Therefore some parameters has been investigated more in details, and then calibrated based on the results of the second experimental activity. In particular the focus was pointed to the beach representation.

The experimental activity was related to two devices were deployed at the same distance from the wave-maker (3.60m), with a minimum mutual long-shore distance according to the mooring system (i.e. 2.00m, equals to 5*b*) at a water depth of 0.45m in 1:60 scale.

The same module MIKE 21 BW - 2DH was chosen to represent the laboratory configuration. The basin was reproduced considering its real dimension and a virtual space around it (50 cells in each direction) with a space grid of 0.05m. The bottom of the laboratory basin is made in concrete and so a constant Manning number of 40 $m^{1/3}/s$ was used whereas the beach side is full with gravel and a varying Manning number between 40 and 20 $m^{1/3}/s$ was adopted. The devices were represented through a porous layer simplified with a rectangular shape (1.0m in cross-shore, 0.4m in long-shore direction). Following the MIKE manual guidelines (DHI,2008), waves were created through an internal wave generation choosing a Jonswap wave spectrum (spreading factor equal to 30, i.e. maximum deviation from the main incident wave direction of 14.7°) and a sponge layer (of 50 cells) was adopted to numerically absorb the waves in the wrong direction of propagation. The minimum wave period reproducible with MIKE 21 BW with this configuration was 0.75s, and since it is closer to the milder WSs, only the higher WSs have been used in the calibration procedure. The whole numerical set-up is summarized in the figure 9.21.

The beach has been represented with a not constant bathymetry and bottom friction, and at the same time through a constant porosity layer. The optimal porous factor has been calibrated through a direct comparison with the laboratory results in order to represent the laboratory wave reflection. In particular the comparison was possible by extracting the surface elevation in cells corresponding to the laboratory WGs.

The calibration focused on the beach representation, i.e. its extension, its bottom friction and/or slope and porosity factor, and was preliminary performed without the presence of the devices, and then each attempt has been compared with the relative physical tests (i.e. empty basin). The several alternatives are summarised in the following table 9.4.

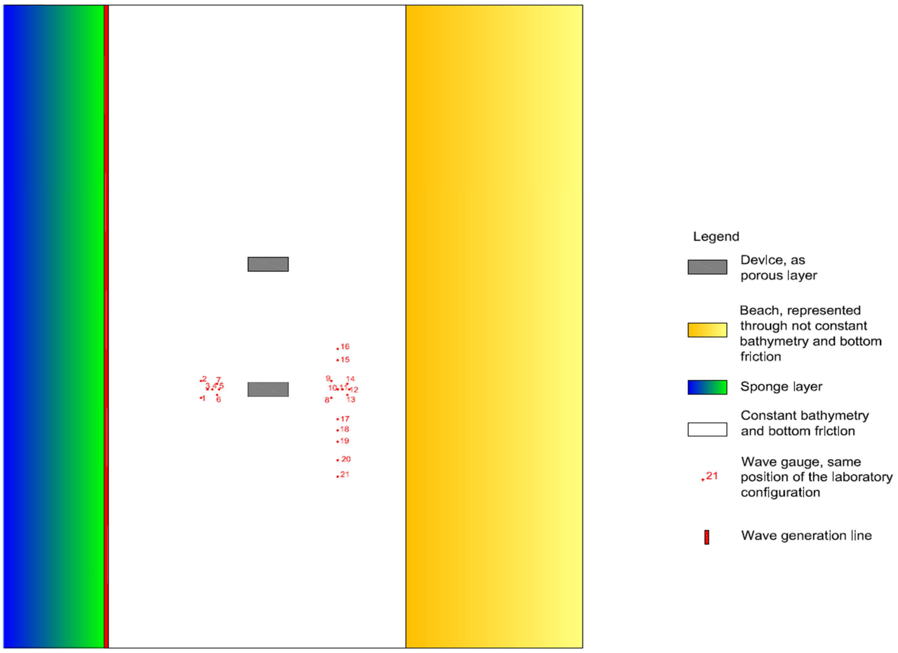

***Figure 9.21** – Summarizing of the set-up used in MIKE 21 BW.*

Test num.	Name of the Test	Description
1	WS6n1	2D, beach slope 1:2.67 (20.6°), porous factor of 0.85, porous layer on the laboratory beach space
2	WS6n3	2D, beach slope 1:2.67 (20.6°), porous factor of 0.85, porous layer on all the beach space (real + virtual)
3	WS6n4	2D, beach slope 1:2.67 (20.6°), porous factor of 0.90, porous layer on the laboratory beach space
4	WS6n5	2D, beach slope 1:2.67 (20.6°), porous factor of 0.70, porous layer on the laboratory beach space
5	WS6n7	2D, beach slope 1:1.87 (28.2°), porous factor of 0.90, porous layer on the laboratory beach space
6	WS6n8	2D, beach slope 1:2.67 (20.6°), higher bottom friction in the beach zone, porous factor of 0.90, porous layer on the laboratory beach space
7	WS6n9	2D, beach slope 1:2.33 (23.2°), porous factor of 0.90, porous layer on the laboratory beach space
8	WS6n2	3D, beach slope 1:2.67 (20.6°), porous factor of 0.85, porous layer on the laboratory beach space (analogous to WS6n1)
9	WS6n6	3D, beach slope 1:2.67 (20.6°), porous factor of 0.90, porous layer on the laboratory beach space (analogous to WS6n4)
10	WS6n10	3D, beach slope 1:2.33 (23.2°), porous factor of 0.90, porous layer on the laboratory beach space (analogous to WS6n9)

***Table 9.4** – List of the simulations performed for the calibration of the beach representation.*

The results of the sensitivity analysis performed on the 2D tests listed in the previous table are graphically reported in figure 9.22. In particular, it is possible to assess that:

- the extension of the porous layer (from test n.1 to n.2) does not cause any significant effect on the overall wave field;
- the porous factor seems to be the key parameter (as already found in previous simulation, i.e. in the sections 9.2 and 9.3), in particular:
    - a reduction of its value (from test n.1 to n.4) leads to a noteworthy increase of the wave height –especially in the incoming zone (WGs n.1-8)– and of the wave reflection derived at the group of three aligned WGs (3-5 and 10-12);
    - an increase of its value (from test n.1 to n.3) leads to slight wave height variation, more marked in the centre basin zone (WGs n.8-14) where the results are more similar to the laboratory ones;
- the increase of the bottom friction (from test n.3 to n.6) does not show notable differences, since the bottom friction was already pretty high and similar to the laboratory condition even for the test n.4;
- a strong increase of the beach slope (from test n.3 to n.5) produces higher wave height in all the basin and higher wave reflection (derived at same two groups of three aligned WGs as before).

The differences between numerical and physical results at the WGs n.15-21 (which were at the same distance from the beach) are mainly related to the global and local shape of the beach and to its reflectivity, which were fickle parameters in case of the laboratory tests. The exact geometrically beach variation is obviously not representable with MIKE.

However the configuration that better reproduced the laboratory was the one with a beach slope of 20.6°, higher bottom friction in the beach zone, porous factor of 0.90 (i.e. WS6n9). This configuration was then checked also under 3D wave condition (WS6n10).

The effects induce by the presence of the devices were analysed by adding a second porous layer in their correspondence and reported in figure 9.23. In the configuration named Test1, the porous factor assigned to the devices porous layer was 0.85, whereas Test3 is by a porous factor of 0.70.

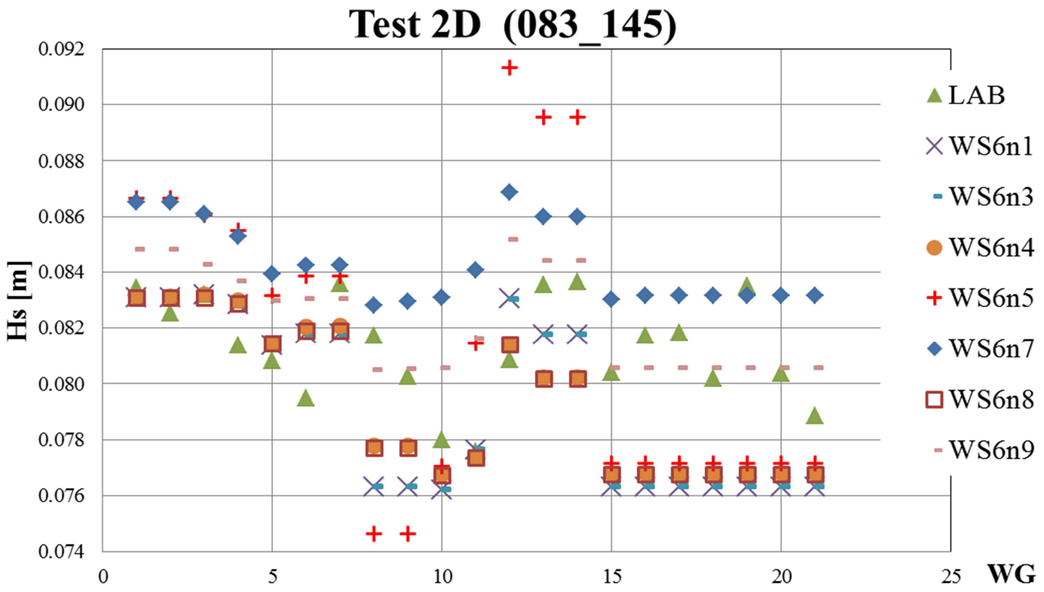

Figure 9.22 *– Calibration analysis on the* H_S *at the 21 WGs for the 2D numerical simulations.*

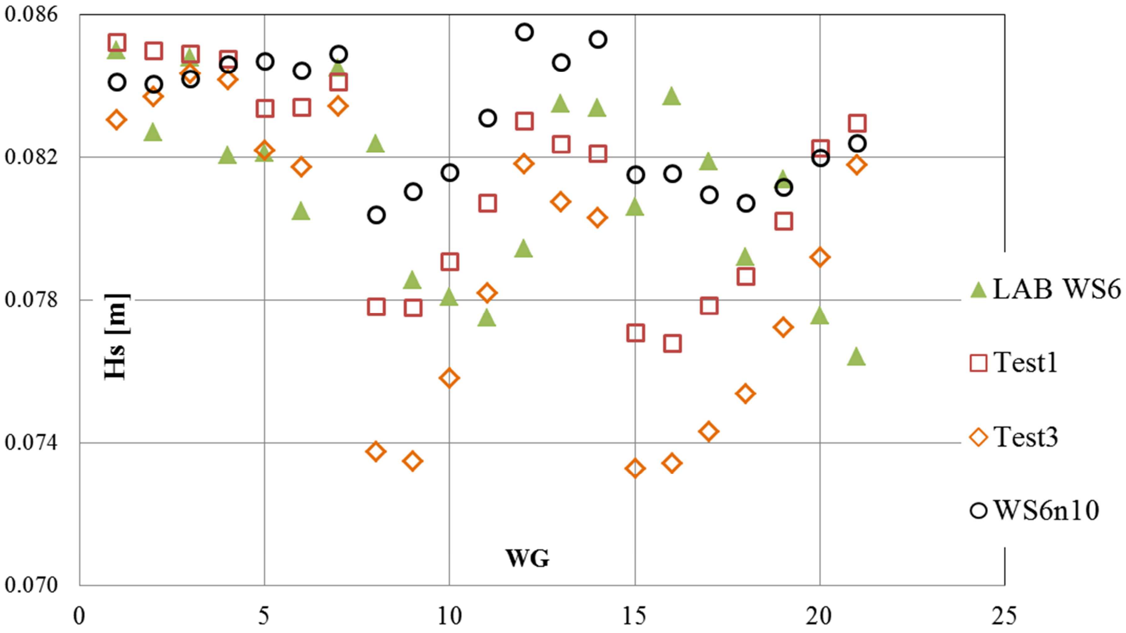

Figure 9.23 *–* H_S *at the 21 WGs for the laboratory results (green triangles), the simulation performed without the device (black circles) and the same configuration with the devices decreasing the porous factor on the devices (red squares and orange diamonds respectively).*

The presence of the devices (WS6n10 vs. Test1) produces a global wave reduction, mainly notable with the following effects:

- a significant reduction of the H_S behind the devices (WGs from n.8 to n.14);
- a different H_S trend in the centre of the basin, i.e. behind and between the devices (WGs n.15-16). These differences could be explained due to the wave interaction induced by the two devices;
- a different H_S trend in the lateral zone behind the devices (WGs from n.17 to n.19). This reduction is due to the wake zone induced by one device.

The numerical effect induced by the presence of the devices are more marked than in the laboratory results, e.g. in the laboratory the interaction between the devices (WGs n.15-16) seemed absent (i.e. H_S at the WG n.16 was equal to the incoming value).

Furthermore figure 9.23 shows that a reduction of the porous factor (Test1 vs. Test3) leads to lower H_S and higher difference with respect to the laboratory results. Therefore the configuration of the Test1 has been selected.

However, the porous layer expedient on the beach does not solve the overestimation problem of the reflected field, in fact the numerical K_R are again higher than the laboratory ones, even if their similarity is improved.

10. ANSYS-AQWA

Since MIKE 21 is not able to represent dynamic aspects, such as mooring systems (type, pre-tension levels, inertia, etc.) or joint connection (as the hinge below the PTO) or energy lost due to device rigidity and/or inertia, etc. the numerical activity was integrated with a second software: ANSYS-AQWA developed by ANSYS. The numerical results were compared to the experimental ones (i.e. related to the second investigation phase). Once the comparison is optimized, ANSYS allows to evaluate different mooring configurations more suitable to response to real sea states. It is worthy to remark the ANSYS software work in full scale and not in laboratory scale.

ANSYS has several modules, the ones relative to the hydrodynamic analysis are ASAS (software for advanced structural assessment of all types of fixed and floating structures), FLUENT fluid analysis, ANSYS AQWA Hydrodynamic Diffraction and ANSYS AQWA Hydrodynamic Time response. For the purpose of this thesis only the last two modules were used.

In particular, ANSYS AQWA Hydrodynamic Diffraction develops the primary hydrodynamic variables required for complex motions and response analyses, solving the Green function for irrotational flow by means of boundary element and panel method (Newman, 1985).

ANSYS Hydrodynamic Time response, instead, performs the dynamic analysis in frequency or time domains, deriving the impulsive response from the previous module and solving the equation of motion by means of the state-space method (Journée and Massie, 2001). The analysis is coupled to the cable dynamics, where each line is solved by a finite element approximation. Slow-drift effects and extreme-wave conditions may be investigated within the time domain (Chakrabarti, 2004). Damage conditions, such as line breakage, may be included to investigate any transient effects that may occur.

In this section the investigation carried out on the device under exam is reported focusing on the reproduction of the experimental spread mooring system set-up and on the main numerical results.

10.1. SET-UP

The laboratory configuration (device + spread mooring system) described in the second experimental investigation (see Section 8) was reproduced in full scale in ANSYS-AQWA. The laboratory device dimensions (in cm) are reported in the following figure.

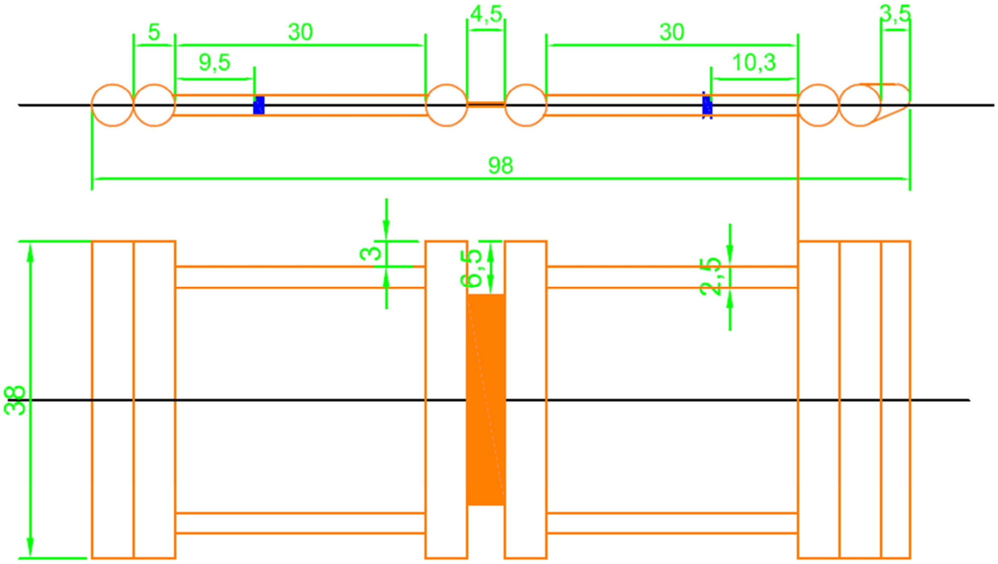

Figure 10.1 *– Device dimensions in cm in 1:60 scale.*

In the numerical software, the device was reproduced with two rigid and separate structure (see Fig. 10.2) jointed with a hinge connection. The numerical rigidity of the hinge connection should represent the PTO presence. However numerical hinge rigidity variations do not lead to significant result dissimilarities, as it was proved by the experimental activities. Furthermore, according to the manual, "a connection stiffness object only applies to a hydrodynamic diffraction analysis" and not to the time response module. However also in the Hydrodynamic Diffraction analysis the effect of the stiffness is quite negligible, only the extreme cases of infinite and zero rigidity are handled with accuracy.

In order to complete the numerical analysis, the device was meshed. According to the manual, it is required that the most of the elements size is lower than $L/7$, where L is the wavelength of the highest frequency; if this suggestion is violated for more than 10% the results may be inaccurate. In the performed simulation, in order to guarantee this condition and to accurately reproduce the device geometry, a mesh size of 1m was chosen. However a greater grid space proved to not strongly affects the results.

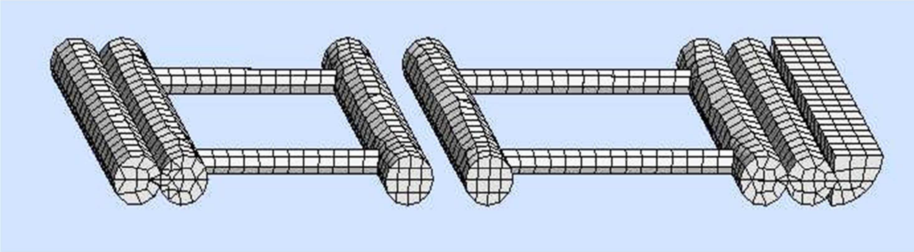

Figure 10.2 *– Mesh of the device used for the ANSYS simulations.*

Once the geometry, the draft and the material have been defined, ANSYS automatically derives the mass and the centre of masses. Even if the geometry was set to reproduce as close as possible to the laboratory one, differences on the overall weight occurred. In particular, in the numerical simulation the device has a weight of 480ton, whereas the laboratory device was around 4 kg in 1:60 scale, i.e. 864 ton in full scale. It is possible that the device draft in the experiments was larger than design conditions.

The global numerical set-up is shown in figure 10.3; the front chains diverged 24°, or more precisely their anchors were 122.4m along the axial direction (i.e. the direction of the wave, in case of perpendicular wave attack) and 55.2m along the transverse direction (direction of the wave front); whereas the rear chains diverged 23°, or more exactly the anchors were at 84.0m and 36.0m, for the axial and transverse direction, respectively. The mooring lines were modelled assuming a weight of 720kg/m, an equivalent diameter of 0.34m, $EA=1.9\cdot10^{10}$N, $F_{max}=1.8\cdot10^{7}$N.

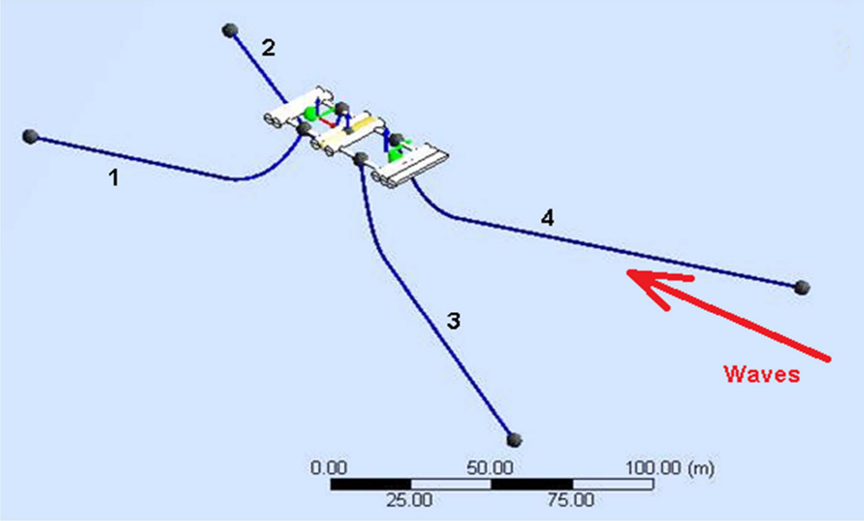

Figure 10.3 – *Global numerical set-up: device + spread mooring system.*

The simulation target was to reproduce the experimental results (in particular regarding the loads acting on the mooring lines and the device motions), in terms of statistical values and also of time history. In order to replicate the signal time series, the input used in the software was the reconstructed waves time history derived from experimental data at the WGs n. 3-4-5 (see Fig. 8.1). It is worthy to remark that the software does not accept a long time series as input, and therefore the input cannot be the actual incident wave but a random sequence.

Numerical simulations were performed under regular and irregular WSs, regarding the irregular WSs, only few tests were carried out, corresponding to the WSs from n. 2 to n. 9 of table n. 8.2, obviously in full scale (see Tab. 10.2). Among the numerical simulations, only the WS n. 5 was repeated for all the three mooring pre-tension levels, since the measured load has a low noise, and waves are not so large to induce breakings.

10.2. MAIN RESULTS

The numerical software provide several outputs, such as the RAO (Response Amplitude Operator), displacements of the centre of mass, bodies position or velocity or acceleration, time history of the forces acting on the mooring lines or on the structure or on the joint connection, etc.

A preliminary study was assessed to determine the device stability. This analysis was carried out under regular waves by varying frequency and direction. Figure 10.4 shows an example in the yaw direction. It may be observed that before reaching the equilibrium, the device oscillates in yaw quite significantly, however the equilibrium is reached approximately after 300 s.

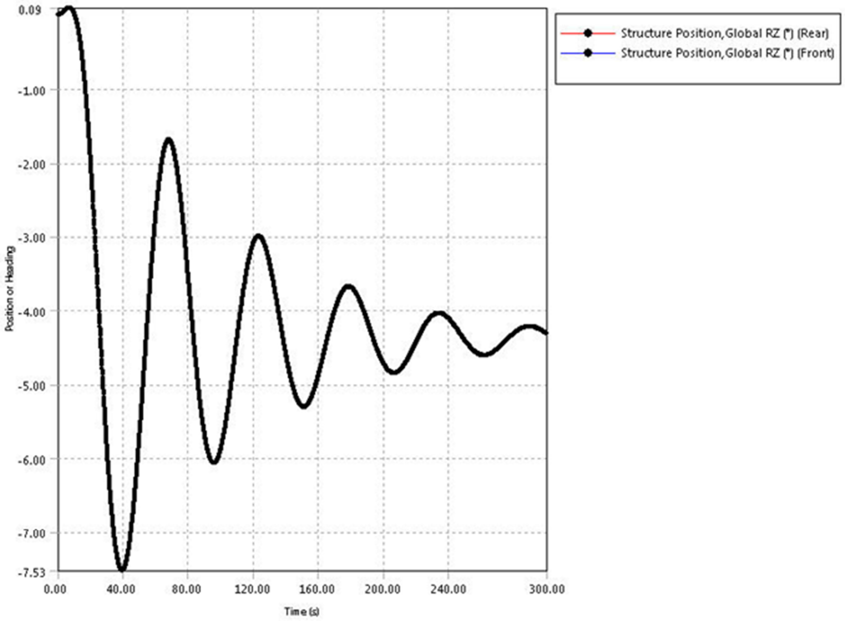

***Figure 10.4 –** Device yaw rotation when subjected to waves with 30° angle, T=4 s. An asymptotic value is reached after a few oscillations (300s).*

The Hydrodynamic Diffraction module does not consider the mooring configuration and mainly run with regular waves, varying the wave frequency and directions. However some results of this module are particularly important, such as wave field due to the device presence and RAO.

Figure 10.5 shows an example of resulting wave field for a regular waves with H=1 m and wave frequency of 0.24 Hz. The used release version of ANSYS do not allow to extract the surface elevation in the domain, however it supplies this wave field map, from which it is possible to visually derived the H_S in front and behind the device.

The values of H_S, obtained from visual considerations, have been used to have a preliminary trend of the K_R and K_T (see Fig. 10.6) derived as (1) and (2). This result confirms the experimental data, i.e. K_T tends to decrease increasing the wave frequency, i.e. decreasing the wave period and so increasing l/L_P; whereas the K_R has the opposite trend.

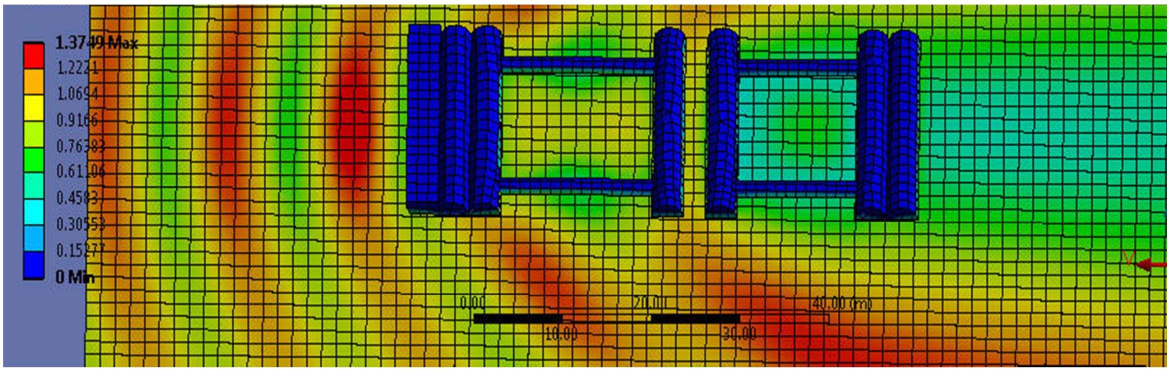

***Figure 10.5** – Wave field around the device for an incident wave with H=1m and f=0.24Hz.*

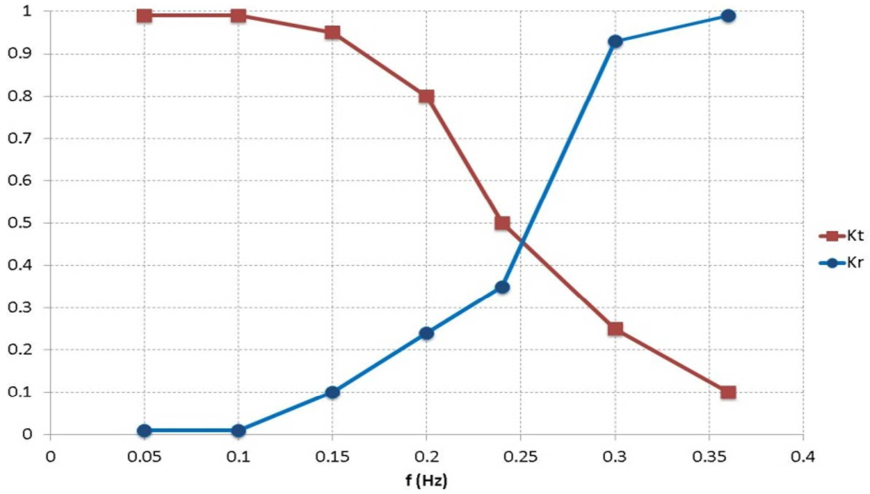

***Figure 10.6** – Device K_R and K_T visually derived from the wave field map obtained with the ANSYS AQWA Hydrodynamic Diffraction module.*

The RAO matrix are available for each DoF of the device; since it was not possible to derive the time series for the experimental 7th DoF, i.e. the relative pitch angle, due to different number of points at the two MTi, particular attention was given to this motion (see Fig. 10.7). It may be observed that there are rotational amplifications in the order of 4 times for wave frequency of 0.22Hz, and of 2 times for wave frequency in the range 0.19-0.25Hz, i.e. T 4-5.26 s. It is worthy to remark that the experimental natural period of the relative pitch was supposed around 0.5s in 1:60 scale, corresponding to 3.9s (i.e. 0.26Hz) in full scale, and therefore the numerical RAO for the relative pitch confirms this previous experimental conclusion.

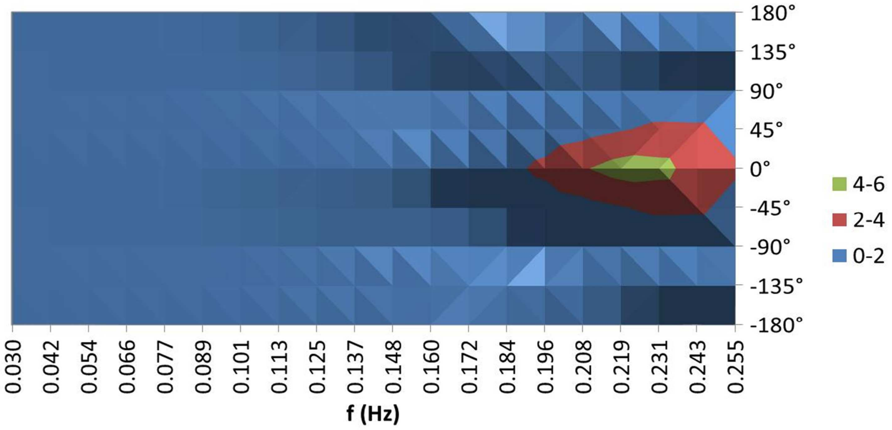

Figure 10.7 – *Amplification factors for the relative pitch angle.*

In order to optimise the forces comparison, a sensitivity analysis was performed under irregular waves. This analysis considered: draft of the device, length of the chains (i.e. initial load on the chains), use/not use of dynamic computation of the mooring loads or computation of long period drift, value of the added mass of the chains and value of the longitudinal and transverse drag coefficients.

From this sensitivity analysis it was highlighted that the average of the measured signal is not compatible with the initial load on the mooring lines. In fact, it is common that the load cell signal is close to zero at the beginning of the tests, rather than being equals to the initial pretension. This aspect is due to electrical noise on the load cells signal, which requires a periodic re-setting of the load cell zero, and this operation removes the initial load.

However the lack of the initial pretension values at the beginning of the test does not compromise the measurements of the dynamic loads. Therefore the comparison between numerical and experimental results was carried out considering the standard deviation of the measured signal rather than the total value.

Results of the sensitivity analysis are summarized in table 10.1.

The removal of the dynamic computation of the mooring lines leads to load peak amplifications and at the same time it is not reproduced all the load peaks (especially the ones due to small period, see Fig. 10.8). The inclusion of the option “evaluate dynamic response of the mooring lines” gives a more realistic result, since it allows to represent peak observed in the measured load time history.

An increase of the added mass (from the value of 1 to a value of 2) increases the load of an insignificant quantity (0.1%), in correspondence of the crest of the “force oscillation”. An increase of the drag or of the cross sectional area increases the load of an appreciable quantity (1-5%) only when the load is large.

The optimal choices in the set-up are the bold case in table 10.1.

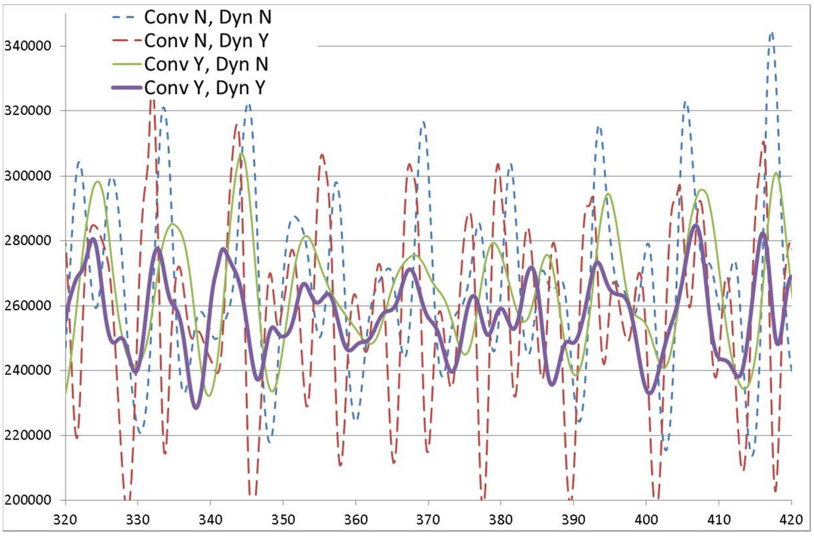

Figure 10.8 – *Effects of the inclusion/exclusion of the dynamic computation of the mooring lines.*

Value of the std of the force (scaled in 1:60 scale) for the WS n.6	Front right (ch23)	Front left (ch22)	Rear right (ch25)	Rear left (ch23)
measured	*0.061*	*0.080*	*0.038*	*0.047*
Dyn=Y, L=design, large mesh+	0.045		0.033	
Dyn=Y, L=+0.5, large mesh+	0.044		0.032	
Dyn=Y, L=+0.8, large mesh+	0.043		0.031	
Dyn=Y, L=+1, large mesh+	0.041		0.030	
Dyn=Y, L=102/145, lm+	0.118		0.092	
Dyn=Y, L=104/147, lm+	0.069		0.050	
Dyn=Y, L=104/148, lm+	0.061		0.043	
Dyn=Y, L=104/148, use frequency sum=Y, dt=0.02 s, lm+	**0.061**		**0.043**	
Dyn=Y, L=104/148, use frequency sum=Y, dt=0.2 s, lm+	0.060		0.040	
Dyn=Y, L=104/148, No wave damping=N, lm+	0.060		0.040	
Dyn=N, L=design, large mesh+	0.070		0.067	

Table 10.1 – *Standard deviation of measured and simulated loads for WS n. 6, L_C=80% under perpendicular waves.*

Figure 10.9 shows an example of comparison relative to the front chains, with the optimal set-up described above. The numerical results are almost perfectly symmetric, hence only the front cable n. 3 (FR, see Fig. 10.3) is given in the legend for simplicity. The measured signals are similar –but not equal– between them, and sometime show a double peak induced by dynamic effects. Furthermore oscillations in the wave period time scale are smaller than predicted, and there is a long period drift, varying with time (with period around of 15 s at model scale).

The numerical and experimental signals are different, both in shape and amplitude. This differences are mainly related to the absence of the long period drift in the simulations (although the option "computation of long period drift" was flagged, maybe because the full matrix of second order response cannot be evaluated in ANSYS), to the different hinge rigidity (which should represent the PTO effects), and to the impossibility to simulate wave spreading, i.e. short-crested waves. This reasons lead to a numerical load overestimation (average standard deviation ratio of 2.2).

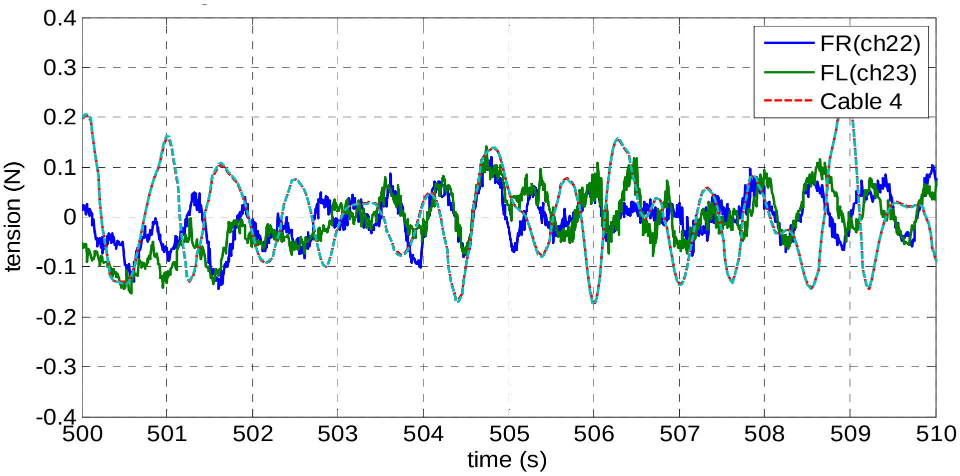

***Figure 10.9** – Comparison of the numerical and experimental load signals at the front chains, for the WS n.5, with L_C=80%.*

The times series of the numerical forces differently from the experimental tests include also information regarding the initial pre-tension level on the chain. It is very common that measures do not account for the initial pretension, because the electrical drift of the load cells requires a periodic re-setting to zero, and this operation also removes the initial pretension from the signal.

From the forces times series it was possible to obtain statistical values $F_{1/100}$, i.e. the mean value of the 1% of the highest points. Table 10.2 reports the results of this analysis, which could be compared to the experimental data represented in the section 8.2.3. The comparison among experimental and numerical forces shows a good agreement (up to 20%) for the ordinary WSs, whereas the discrepancy are much more greater for extreme WSs, due to the not reproduction of breaking waves in the numerical simulations. Even if the numerical results over predict the physical loads, even the numerical forces are well below the breaking condition (which is around 18000kN). There are two main positive aspects of the numerical forces on the mooring lines, i.e. –as expected– they increase more than linearly with H_S and with the mooring pre-tension level (see values of the force for the WS n. 5 in Tab. 10.2). These aspects are coherent to the experimental data, which there was often electrical noise and/or chain interlocking.

WS	L_C **=80%**	L_C **=65%**	L_C **=50%**
2	-	0.18	-
3	0.42	-	0.45
4	-	-	0.88
5	0.65	0.77	2.22
6	1.31	-	6.99
7	7.57	-	-
8	-	-	-
9	7.56	19.68	-

Table 10.2 – *Numerical results of the $F_{1/100}$ for the simulation performed with ANSYS-AQWA, under perpendicular 2D irregular WSs.*

10.3. MODEL LIMITATION

The model limitations may be divided into different groups, e.g.:

- incident wave generation. The model reproduces first order Airy waves, long-crested regular and irregular waves (no spreading), small wave obliquity are correctly reproduced. A short time history of wave elevation in a specified point may be defined, however it is considered only at 0° and the maximum duration of the time history is around two hours;
- simulated process: reflection and transmission could be derived only in a visually form; overtopping is not really represented, although during the simulation waves seem to flow over the temporarily submerged body. Long drift process is not reproduced;
- geometry is limited by the size of the mesh and of the tolerance dimensions, this aspect has consequences on the choice of the natural frequency in the ANSYS-AQWA Hydrodynamic Diffraction module;
- general bugs of the 14.0 release: the whole matrix with non-linear transfer functions is not solved, modifications on the connection stiffness does induce a load along the connection, but do not affected the movements of the body,

10.4. MODEL POTENTIALITY

Some of the ANSYS output may be elaborated in order to improve the device knowledge, for example the assessment of a forces/displacement curve to be used in the mooring design phase (analogous to Fig. 8.30), or in a more complex software which may be include also the PTO system representation. ANSYS does not directly provide this information, however it is possible to obtain it through the time history of displacements of fixed/known points and of the forces acting on the mooring lines.

According to the analysed response of the device under exam, it was found that the vertical oscillations of the fairlead are significantly lower than the wave amplitude. Consequently, it is reasonable to presume that the quasi-static load on the mooring only depends on the relative horizontal position of e.g. the fairlead.

10.5. MORE REALISTIC MOORING CONFIGURATION

During the experimental activities, it was proved that the device should work aligned with the main wave direction, or at least there should be a small angle between the main device axis and the incoming waves. Since real sea states are characterized by several prevalent wave directions the spread mooring system may be the not-optimal mooring configuration. Therefore a different mooring configuration (i.e. a CALM system) was analysed through ANSYS-AQWA. The CALM system allows the device to freely re-oriented it-self to the incoming wave direction.

In particular, this new mooring configuration consider a buoy (diameter 12m, draft 2m and freeboard 2m) moored with four steel chains, and a cable which connects the buoy and the device (see Fig. 10.11). The device is also restrained with a rear long chain, necessary to avoid a rotation at 360° and provide a sort of extra security connection in case the line breaks down.

This new configuration was subject to several ordinary and extreme WSs (from n.3 to n.8 of table 8.2 scaled in full scale) and to different wave obliquity.

Milder WSs produce really small loads on the chains, whereas loads obtained for most energetic WSs may be inaccurate due to the possible presence of wave breaking in proximity of the device. During the simulations, an initial warning suggests that the chains connecting the buoy are too slack, (even if they never go slack during the simulations, and the synthetic line does, see Fig. 10.12).

Figure 10.13 shows the statistical value of the force ($F_{1/100}$) the different mooring lines as a function of the wave obliquity β for the same irregular WS n. 5.

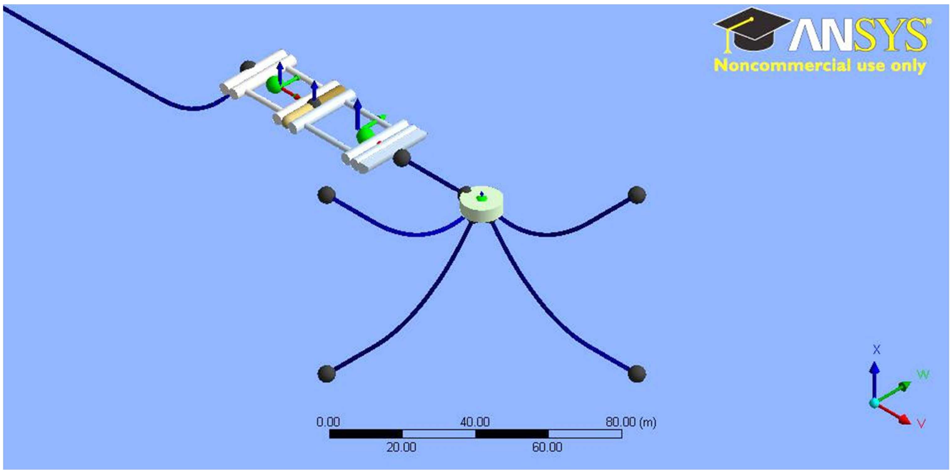

Figure 10.11 – *CALM system analysed through ANSYS-AQWA.*

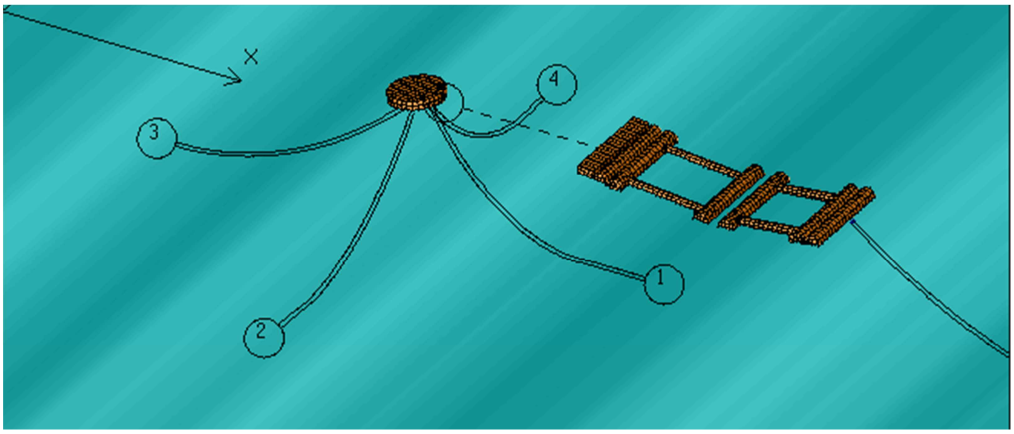

Figure 10.12 – *Instant when the synthetic line, between the device and the buoy, goes slack.*

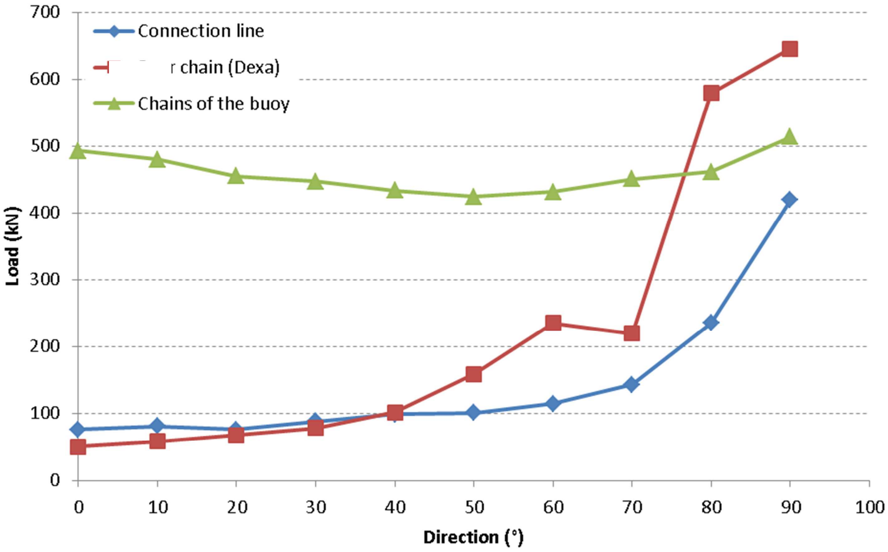

Figure 10.13 – *$F_{1/100}$ on the different mooring lines, in function of β for the WS n. 5.*

11. CONCLUSION

This thesis is focused on the analysis of a floating Wave Energy Converter (WEC) of the Wave Activated Body type. The device is composed by two rigid pontoons with a hinge in between, which allows each pontoon to pivot in relation to the other. In particular the main target is the hydrodynamic induced by an array of WECs, under a physical and numerical point of view.

The physical investigation was carried out in two phases both at the University of Aalborg (DK). During the first investigation the hydrodynamics around a staggered wave energy farm composed by three devices in 1:60 scale was analysed, and the tests were integrated also with a model in 1:30 scale. Two mooring systems were investigated: a “spread” and a CALM type. The second investigation, instead, employed two devices in 1:60 scale and anchored with an asymmetric “spread” mooring system, at a same distance from the wave-maker.

During the experimental activity several tests were performed in order to investigate geometry (device dimensions, mutual distances, Power Take-Off (PTO) rigidity, mooring type) and climate (water depths at installation h, wave obliquity β) key design parameters. These aspects were mainly analysed under ordinary North Sea wave climate.

The numerical study, instead, was performed with two commercial codes: MIKE 21 BW, developed by DHI Water & Environment & Health and ANSYS-AQWA developed by ANSYS. In particular, the hydrodynamic of the wave farm was reproduced in MIKE 21 BW, where the devices were represented as porous bodies (i.e. fixed porous piles with rectangular cross section), whereas dynamic aspects (such as motion, joint connection and moorings) were simulated through ANSYS using the ANSYS AQWA Hydrodynamic Diffraction and ANSYS AQWA Hydrodynamic Time response modules.

The most relevant results are summarized in the following sub-sections in terms of device performance and guidelines for a future wave farm installation.

11.1. SUMMARY OF THE RESULTS

To facilitate the report of the outcomes of the PhD research activity, the results have been split in the experimental and numerical field.

11.1.1. EXPERIMENTAL OUTCOMES

The overall experimental activities lead to several important outcomes, which can be divided in the following topics.

1. Device design parameter: it was found that the key parameter is l/L_P: where l is the device length and L_P is the peak wave length. This parameter affects the overall device behaviour, in terms of hydrodynamics, power production, moorings and motions. It is however worthy to remark that tests were performed under ordinary North Sea wave state (WS) condition with $0.4 < l/L_P < 1.2$.

2. Hydrodynamics: this aspect was investigated in the time and frequency domain, in terms of significant wave heights H_S and transmission coefficient K_T respectively. The values of K_T are particularly important, since they represent a measure of the residual wave energy to be re-converted by the rear devices. Results show that wave transmission is high, being K_T always greater than 0.75, and also decreasing for an increase of l/L_P. Under oblique waves, the devices make larger movements and tend to re-orient, leading to higher values of H_S and K_T. This phenomenon is enhanced for long waves, i.e. for low values of l/Lp, and for CALM mooring system. It is therefore suggested to limit the angle between the main device axis at the installation and the incoming wave direction (up to 30°). Furthermore, the water depth at installation does not significantly affect the results, leading to the conclusion that the device would not be particularly sensitive to sea level rise induced by climate changes.

3. Power production data were achieved only under ordinary WSs, because for extreme WSs, the PTO system was presented on the device but it was not instrumented due to high frequency of breaking waves and therefore to protect the measuring systems from splashes. An initial stage was focused on the optimisation of the PTO rigidity (investigated by increasing the vertical distance between the PTO and the device buoyancy plane; the lower the distance the lower the rigidity) and of the mooring pre-tension (investigated by reducing the length of the chain lying on the seabed L_C, from a slack, medium and taut level, L_C=80-65-50% respectively) both based on the power production. The optimal PTO rigidity is mooring dependent, and comparing the power production for the optimal PTO rigidities –for the corresponding pretension levels– the slack pre-tension level results to be the best configuration.

The power production of a single device is always lower than 167kW, in full scale. If the same probability of occurrence for each WS is assumed, the variation of the mooring pre-tension level –from a slack to a taut configuration– leads to a decrease of the 16% of the power production.

The device efficiency η has been derived by comparing the power production with the available wave power for each WS. Sets of η show pretty marked peaks around l/L_P =0.80 and 1.21. The effects of the wave obliquity is limited, however the efficiency tends to decrease for wave obliquity greater than 10°.

A CALM mooring system leads to lower wave transmission and also larger power production than a spread mooring.

Results of hydrodynamics and power production are in agreement with previous tests on a similar device (Zanuttigh et al., 2010).

4. forces acting on the mooring lines are always well below the failure conditions (one hundred times lower than the breaking limit, which is around 1000 N) for all the WSs. For the ordinary WSs, the forces are lower for perpendicular wave attacks, whereas for the extreme WSs the trend is the opposite. Comparing the ordinary WSs, an increasing of the mooring pre-tension level (i.e. from L_C=80% to L_C=50%) leads to an increase of the forces acting on each mooring line. For the front chains the dependence of the force trend on the WS (i.e. on the available wave power) is more pronounced.

5. device motions. All the 6 canonical motions tend, obviously, to increase with increasing H_S, whereas they tend to decrease with increasing l/L_P. For the ordinary WSs, the surge and sway motions are indeed limited compared to the heave motion, proving that the moorings are effective in keeping the device position. In particular the smallest motion is the sway. For higher WSs, all the translations tend to increase by increasing the wave obliquity especially the sway motion. When analysing the rotations, pitch and yaw are much greater than roll.

For most WSs, the heave, the pitch and yaw decrease with decreasing the mooring pre-tension level, whereas the surge increases. The sway and the roll seem always independent from it.

The device behaviour is affected by its natural periods, in particular the mooring dynamics are affected by surge and yaw, whereas geometry and PTO are connected to pitch and heave. From the free oscillating tests, in fact, two main ranges of natural period were found: around 50s for surge and yaw, and around 3.9s for pitch and heave (values in full scale).

11.1.2. NUMERICAL OUTCOMES

The two numerical codes have different potentiality. The hydrodynamics around single and multiple devices is obtained with MIKE 21 BW, while wave loads and motions for a single moored device are derived from ANSYS-AQWA.

The numerical parameters of the MIKE 21 BW were calibrated based on the experimental results mainly related to the first investigation phase. Results of the calibration process leaded to the conclusion that the porous factor is the key modelling parameter and that an accurate representation of the dissipation at the beach is essential.

The calibrated model well reproduces the incident wave energy, the H_S at the wave-maker and the K_T induced by the devices. The stability of the software with respect to the laboratory tests (i.e. the ability to reproduce the same incident H_S with a change of the wave period) is considered a positive aspect for the validity of the simulation and its repeatability. However the model is not able to accurately reproduce the wave field around the wave farm, especially in the space among the devices due to the impossibility of including the motion of the floating bodies.

Despite the model limitations, i.e. the representation of the devices as fixed porous piles, the numerical model allows to derive a complete map of the hydrodynamics around the devices, and therefore it may be used for a parametric analysis of different farm layouts.

Since MIKE 21 BW was not able to reproduce the device motion, the numerical analysis was integrated with ANSYS-AQWA. This software does not include a great amount of numerical parameters to be varied, and their variation does not lead significant result changes.

For non-breaking waves, the numerical modelling gives a reasonable qualitative and quantitative response (max of 20% discrepancy). Forces acting on the mooring lines were examined assuming that measurements did not include the load at rest, therefore only deviation from the mean measured and computed loads was compared. The discrepancy between simulations and experiments may be explained by several reasons, among which: the impossibility of the numerical representation of short-crested waves (i.e. wave spreading is not allowed in ANSYS), inaccuracy of the modelling of the connection stiffness (the body acceleration did not vary due to its variation), incorrect modelling of the long drift (the full second order transfer function matrix is not evaluated) and absence of the wave overtopping.

As predicted, the numerical loads increase by increasing the H_S or the mooring pre-tension level; however the model over-predicts the measurements. Some outcomes are very useful to understand the device behaviour and also to improve its mooring design giving information/validation on the relation force/displacements. Furthermore ANSYS could be an optimal tool to be used to analyse several mooring layouts, which are not easily reproducible in laboratory and which optimise multi-use platforms from a marine spatial planning point of view.

11.2. GUIDELINES

This section would like to highlight the main design parameters of a wave farm installation derived from the overall research activity. These results can be considered reliable for this analysed device but also for a similar device, i.e. a device based on a similar concept (Wave Activated Bodies) and similar characteristics (inertia, movements, etc.).

1. device optimization

The device should be design based on the parameter l/L_P, i.e. the device length l should be "tuned" based on the local climate conditions, to be l/L_P greater than 0.8 or around 1.0. If it is possible it should be avoided or reduced the time of operation where l/L_P is around or lower than 0.7, i.e. when higher values of wave transmission and greater changes in the transmitted wave direction occur.

To optimise the power production, the device –as tested– should operate in a wave climate characterised by a wave period around 3.9s. This wave period is indeed very short and therefore design optimization would be requested prior to design installation. However even if the device performance are maximised, the low device efficiency leads to the non-economic feasibility of a single installation, therefore a wave farm is required. The layout of the farm is essential in order to optimise the occupied marine space, the overall power production and the coastal defence.

2. optimal inter-distances

The cross-shore distance between the two subsequent wave farm lines needs to be sufficiently long to allow wave energy increasing again after the obstacle represented by the devices. Regardless from the incoming wave direction, a minimum distance of at least 2l is suggested.

The long-shore distance between near devices of a same farm line is dependent on the intensity of the radiated wave field generated by device heaving motion. From the tests, it can be affirmed that –regardless the spread mooring pre-tension level– the wake zone extends for a distance of around 2.9b, where b is the device width, from the device cross-shore axis (for WGs measurements performed at a cross-shore distance of 1.30l from the back cylinder of the back pontoon), leading to a minimum long-shore gap between near devices of 5b. When increasing the gap width, there are no differences in the wave field, i.e. the two devices do not significantly interact. For oblique waves instead, the wake zone could increase up to 3.5b, leading to some wave interactions among the devices for the same gap width of 5b.

3. wave farm layout

With the code MIKE 21 BW, two additional configurations were simulated and compared with the one tested in the laboratory. These configurations consisted of a staggered layout with a reduced gap width between the devices of the first farm line and an aligned configuration with four devices and constant gap width.

In case of the staggered configuration, the decrease of the gap width leads to an overall lower incident wave height behind the second line.

When an aligned configuration is selected by keeping constant the gap width and the cross shore distance among the devices, the second line falls inside the wake of the first line and therefore the available residual wave energy is lower.

Therefore it is suggested –for both coastal protection and energy production– to adopt a staggered layout, which will maximise the devices density and minimize the marine space required for the installation. To benefit from wake effects for hydrodynamic purposes the long-shore distance among the devices should be kept the minimum that allows the moored devices to freely move without crashing.

4. mooring layout

If a “spread” mooring system is chosen, in order to optimise the combination of power performance and hydrodynamics induced by the device, the mooring lines should be slack (i.e. 80% of the total chain length should lying on the seabed). Furthermore to ensure the device survivability the mooring should be designed based under extreme and resonance conditions, the last being linked to the natural period of the surge motion (around 40s).

To allow the device to freely re-orient with respect to the incoming wave direction (with angle difference between the device axis and the prevalent wave direction greater than 10°) a CALM mooring system is suggested. Furthermore it has been proved that a CALM mooring system leads to lower wave transmission and also larger power production than a “spread” mooring.

12. BIBLIOGRAPHY

Aalborg University, (2007). WaveLab3.3 homepage. http://www.hydrosoft.civil.auc.dk/wavelab.

Aalborg University, (2007). AwaSys homepage. http:// http://hydrosoft.civil.aau.dk/AwaSys

Agamloh E., Wallace A. and Von Jouanne A. (2008): Application of fluid-structure interaction simulation of an ocean wave energy extraction device. Renewable Energy, Vol. 33, No. 4, pp. 748-757.

Babarit A., 2010. Impact of long separating distances on the energy production of two interacting wave energy converters. Ocean Engineering, Vol. 37, pp. 718-729

Bahaj, A.S. (2011): Generating electricity from the oceans. Renewable and Sustainable Energy Reviews, 15, 2011, 3399-3416.

Beels C., Troch P., De Backer G., Vantorre M., and De Rouck J. 2010. "Numerical implementation and sensitivity analysis of a wave energy converter in a time-dependent mild-slope equation model", Coastal Engineering, Vol. 57(5), pp. 471-492.

Beels C., Troch P., De Visch K., Kofoed J.P., De Backer G., (2010), Application of the time-dependent mild-slope equations for the simulation of wake effects in the lee of a farm of Wave Dragon wave energy converters, Renewable Energy, Vol. 35, Issue 8, 1644-1661

Borgarino B., Babarit A., Ferrant P., 2011. Impact of the separating distance between interacting wave energy converters on the overall energy extraction of an array. In Proc; Of the 9th European Wave and Tidal Energy Conference, Southampton (UK)

Brooke, J. (2003): Wave energy conversion. Elsevier Publications.

Budal K., "Theory of absorption of wave power by a system of interacting bodies". Journal of Ship Research, Vol. 21, pp 248-253, 1977

Chakrabarti S. (2004): Numerical models in fluid-structure interaction. Southampton: WIT Press.

Charlier, R.H.; Justus, J.R. (1993): Ocean energies: Environmental, economic and technological aspects of alternative power sources". Amsterdam: Elsevier, 534 p

Clément, A.;McCullen, P.; Falcão, A.; Fiorentino, A.; Gardner, F.; Hammarlund, K.; Lemonisa, G.; Lewish, T.; Nielsen, K.; Petroncini, S.; Pontes, M.T.; Schild, P.; Sjöströmm, B.; Sørensenn, H.C.; Thorpe, T. (2002): Wave energy in Europe: current status and perspectives. 6, 5, 405-431.

Count, B. (1980): Power from sea waves. Edinburgh, UK, 449 p.

Cruz, J. (2008): Ocean Wave Energy Conversion – Current Status and Future Prospects. Heidelberg, Germany: Springer-Verlag, 431 p.

Cruz, J., Sykes, R., Siddorn P. and Eatock Taylor, R. "Wave Farm Design: Preliminary Studies on the Influences of Wave Climate, Array Layout and Farm Control." European Wave and Tidal Energy Conference 2009, Sweden

Csiro (2012): Ocean renewable energy: 2015-2050 - An analysis of ocean energy in Australia. CSIRO, Australia, 167 p.

Czech, B.; Bauer, P. (2012): Wave energy converter concepts: Design challenges and classification. IEEE Industrial Electronics Magazine, June-2012

DHI (2008): MIKE21 Boussinesq waves module - scientific documentation

DHI (2008): MIKE21 Boussinesq waves module - User guide.

Drew, B., Plummer, A.R.; Sahinkaya, M.N. (2009): A review of wave energy converter technology. Proceedings of the Institution of Mechanical Engineers 2009, Part A: J. Power and Energy, 223, 887-902.

EquiMar (2011a): Deliverable D4.3 test sites catalogue available at https://www.wiki.ed.ac.uk/download/attachments/9142387/Equimar+Test+Sites.pdf?version=1. Project web page, http://www.equimar.org/

Evans D.V., 1979. Some theoretical aspects of three dimensional wave energy absorbers. In Proc. Of the 1st Symposium on Wave Energy Utilization, Gothenburg, Sweden

Falcão A. and R. Rodrigues (2002). Stochastic modelling of OWC wave power plant performance, Applied Ocean Research, 24 (2), 59-71.

Falcão, A. (2006): The history and progress in wave energy conversion devices. Proceedings of the 9th World Renewable Energy Conference, Florence, Italy.

Falcão, A.F.O. (2010). Wave energy utilization: A review of the technologies. Renewable and Sustainable Energy Reviews, 14, 899–918.

Falnes J., “Radiation impedance matrix and optimum power absorption for interacting oscillators in surface waves”. Applied Ocean Research, Vol. 2, pp 75-80, 1980

Frigaard P. and K. Nielsen (2008): Assessment of Wave Energy Devices. Best Practice as used in Denmark., World Renewable Energy Congress (WREC X), Glasgow, UK. July.

Frigaard, P. and T. Lykke Andersen (2009). Effektmålinger på Wave Star i Nissum Bredning. Afsluttende rapport under PSO-F&U 2008-1-10023. DCE Technical Report No. 61, Dept. of Civil Eng., Aalborg University.

Harris R.E., Johanning L., Wolfram J., (2004), Mooring systems for wave energy converters: A review of design issues and choices, Heriot-Watt University, Edinburgh, UK.

Hashimoto N., Kobune,K., (1988), Estimation of directional spectrum from a Bayesian approach. Proc.21st ICCE Vol 1. ASCE pp.62-72

Heller, V. (2012): Development of Wave Devices from Initial Conception to Commercial Demonstration. Oxford Elsevier, 79 – 110

Hudson, J.A., Phillips, D.C., Wilkins N.J.M., (1980) “Materials aspects of wave energy converter”, Journal of Material Science, 15, 1337-1353.

IEA (2011): Annual Report 2011 - Implementing Agreement on Ocean Energy Systems.

Ingram D., Smith G., Bittencourt-Ferreira C., Smith H.: Protocols for the Equitable Assessment of Marine Energy Converters, European Ocean Energy Association, 2011

Journée J.M.J. and Massie W.W. (2001): Offshore hydromechanics. Delft University of Technology, 570 pp.

Kirby J.T. and Dalrymple R.A. (1994) Combined refraction/diffraction model REF/DIF, Report CACR-94-22 Centre for Applied Coastal Research, Universilty of Delaware

Kofoed, J. P (2009): Hydraulic evaluation of the DEXA wave energy converter. DCE Contract Report No. 57. Dep. of Civil Eng., Aalborg University, Apr. 2009.

Kofoed, J.P. and P. Frigaard (2008). Hydraulic evaluation of the LEANCON wave energy converter. DCE Technical Report No. 45. ISSN1901-726X. Dep. of Civil Eng., Aalborg University, Oct. 2008.

Koftis T. and Prinos P. (2005): 2D-V Hydrodynamics of Double Floating Breakwaters. Coastal Dynamics

Koutandos, E., Prinos, P. and Gironella, X., 2005, Floating Breakwaters Under Regular and Irregular Wave Forcing-Reflection and Transmission Characteristics, J. Hydraul. Res. IAHR 43(2), 174–188.

Mendes L., Palha A., Fortes C.J., Brito e Melo A., Sarmento A., 2008 Analysis of the impact of a pilot zone for wave energy conversion offshore Portugal, International Society of Offshore and Polar Engineers

Madsen, P A, Sørensen, O R and Schäffer, H A (1997a) Surf zone dynamics simulated by a Boussinesq type model. Part I: Model description and cross-shore motion of regular waves. Coastal Eng., 32, 255-288.

Madsen, P.A. and Sørensen, O.R. (1992) A new form of the Boussinesq equations with improved linear dispersion characteristics. Part 2: A slowly-varying Bathymetry. Coastal Eng. 18, 183-204.

Mansard E.P.D, Funke E.R. (1980), The measurement of incident and reflected spectra using a least squares method. Proc. of the 17th International Conference Coastal Engineering (ICCE). ASCE, 28.01.1998, Sydney, Australia.

McCormick, M.E. (2007): Ocean Wave Energy Conversion. Dover Publications.

Millar D.L., Smith H.C.M., and Reeve D.E.. 2006. “Modelling analysis of the sensitivity of shoreline change to a wave farm”. Ocean Engineering, 34, 884-901.

Newman J. N. (1985). Algorithms for the Free-Surface Green Function. Journal of Engineering Mathematics, 19:57–67.

Nielsen, F.G.; Andersen, M.; Argtriadis, K.; Butterfield, S.; Fonseca, N.; Kuroiwa, T.; Waegter, J. (2006): Ocean wind and wave energy utilization. in Proc. 17th Int. Ship and Offshore Structures Congr., , 2, Southampton, UK, 165-211

Nielsen, K. (2012): Ocean energy technology study. DanWEC, Denmark.

Nørgaard J. H., Poulsen M. (2010), Wave height reduction by means of wave energy converters, MSc in Civil Engineering, 4th. Semester, Aalborg University

Palha A., Mendes L., Conceiç J. F., Brito-Melo A. and Sarmento A. (2010): The impact of wave energy farms in the shoreline wave climate: Portuguese pilot zone case study using Pelamis energy wave devices. Renewable Energy 35 (2010) 62–77

Previsic, M.;Bedard, R.; Hagerman, G. (2004): E2I EPRI Assessment - Offshore wave energy conversion devices. USA.

Ricci P., Saulnier J.B., Falcao A.F., “Point-absorber arrays: a configuration study off the Portuguese West-Coast”.7th European Wave and Tidal Energy Conference, Porto, Portugal, 2007

Ross, D. (1995): Power from sea waves. United Kindom: Oxford University Press, 212 p.

Shaw, R. (1982): Wave energy: a design challenge. Chichester: Ellis Horwood, 202 p.

Sørensen, O R, Schäffer, H A and Madsen P A (1998) Surf zone dynamics simulated by a Boussinesq type model. Part III: Wave-induced horizontal nearshore circulations. Coastal Eng., 33, 155-176.

Sørensen, O R, Schäffer, H A and Sørensen. L S (2004) Boussinesq-type modelling using an unstructured finite element technique". Coastal Eng., 50, 181-198.

Troch P., Stratigaki V., Stallard T., Forehand D., Folley M., Kofoed J.P., Benoit M., Babarit A., Gallach Sánchez D., De Bosscher L., Rauwoens P., Elsässer B., Lamont-Kane P., McCallum P., McNatt C., Angelelli E., Percher A., Carpentero Moreno E., Bellew S., Dombre E., Charrayre F., Vantorre M., Kirkegaard J. and Carstensen S. 2013. Physical Modelling of an Array of 25 Heaving Wave Energy Converters to Quantify Variation of Response and Wave Conditions In Proc; Of the 10th European Wave and Tidal Energy Conference, Aalborg (DK)

Vennetti, D. (2012): Technology survey for renewable energy integrated to bridge constructions. SP Technical Research Institute of Sweden, Traffic Safety, Environment and Technology Department, Sweden.

Venugopal, V. and G.H. Smith. 2007. Wave climate investigation for an array of wave power devices. Proceedings of the 7th European Wave and Tidal Energy Conference, Porto, Portugal.

Vicente, P., Falcão, A., Gato, L., Justino, P. 2009. Dynamics of arrays of floating point-absorber wave energy converters with inter-body and bottom slack-mooring connections. Applied Ocean Research, Vol. 31 (4), 267-281.

WAVEPLAM (2009): Deliverables D 2.1 State of the Art Analysis - A Cautiously Optimistic Review of the Technical Status of Wave Energy Technology available at http://www.waveplam.eu/files/downloads/SoA.pdf

Weber, J. (2011): Integrated WEC system optimisation - Achieving balanced technology development and economical lifecycle performance. . Presentation at NUI Maynooth Ocean Energy Workshop, Maynooth, Ireland.

Weber, J. (2012): WEC technology readiness and performance matrix - finding the best research technology development trajectory. 4th International Conference on Ocean Energy, ICOE 2012, Dublin, Ireland.

Wheeler, R.L. 2001. Sir Christopher Sydney Cockerell, C.B.E., R.D.I. 4 June 1910 -- 1 June 1999: Elected F.R.S. 1986. Biographical Memoirs of Fellows of the Royal Society 47: 67.

Zanuttigh, B. 2011. Coastal flood protection: what perspective in a changing climate? The THESEUS approach, Environmental Science and Policy, 14, 845 – 863.

Zanuttigh B., Martinelli L., Castagnetti M, Ruol P., Kofoed J.P., Frigaard P, (2010) Integration of wave energy converters into coastal protection schemes, 3rd International Conference on Ocean Energy (ICOE), 6 October, Bilbao.

PART C – PUBLICATIONS

13. LIST OF PUBBLICATIONS

Some of the results of this PhD research activity was published in international journal and was a contribute to several international Conferences. The complete list of publications (with their abstracts) is included in this chapter and then selected papers are presented in a full version.

13.1. INTERNATIONAL/NATIONAL JOURNALS

Zanuttigh B. & Angelelli E. “Conversione di energia ondosa e protezione della costa mediante dispositivi galleggianti di tipo Wave Activated Bodies” ENEA “Energia Ambiente e Innovazione” (2011) n. 4-5/2011 pp 42-44, http://www.enea.it/it/produzione-scientifica/EAI/anno-2011/n.%204-5%202011%20Luglio-ottobre2011/conversione-di-energia-ondosa-e-protezione-della-costa-mediante-dispositivi-galleggianti-di-tipo-wave-activated-bodies
ISSN code: 11240016

Zanuttigh B. & Angelelli E. “Experimental investigation of floating wave energy converters for coastal protection purpose” Coastal Engineering 80 (2013) pp148–159 http://ac.els-cdn.com/S0378383912001809/1-s2.0-S0378383912001809-main.pdf?_tid=9b6c2e98-d8e2-11e2-bfa8-00000aab0f26&acdnat=1371648035_59d412830aebb750de8e38d8392ffef4
Scopus code: 2-s2.0-84871511705
ISSN code: 03783839

Zanuttigh B., Angelelli E. & Kofoed J.P. “Effects of mooring systems on the performance of a Wave Activated Body Energy Converter” Renewable Energy 57 (2013) 422-431 http://www.sciencedirect.com/science/article/pii/S0960148113001031
ISSN code: 09601481

Angelelli E. “Valutazione energetica del convertitore di energia da onda WavePiston” Studi costieri (2013) n. 21 pp69 – 70
ISSN code: 1129-8588

Mendoza E., Silva R., Zanuttigh B., Angelelli E., Lykke Andersend T., Martinelli L., Nørgaard J.Q.H. & Ruol P. “Beach response to wave energy converter farms acting as coastal defence” Coastal Engineering (2013)

http://www.sciencedirect.com/science/article/pii/S0378383913001749
Scopus code: 03783839
ISSN code: 03783839

13.2. PROJECT REPORTS

13.2.1. OFFICIAL DELIVERABLE

Burchart H.F., Zanuttigh B., Lykke Andersen T., Nørgaard J.H., Angelelli E., Ruol P., Martinelli L., Mendoza-Baldwin E., Silva-Casarín R., Enriquez-Ortiz C., Koftis T., Prinos P., Galiatsatou P., Chávez-Cárdenas X., Hoil-Baeza J., Bustos-Lira A., Pinedo-González J., Kuznetsov S., Saprykina Y., Lara J.L., Steendam G.J., Pezzutto P., Raosa A.N., Sergent P., Prevot G., Ostrowski R., Biegowski J., Kaczmarek L., Piotrowska D., Skaja M., Zoppi C., Leontev I., Akivis T., Kappenberg J., Sothmann J., Ohle N., Schuster D., Trifonova E., Keremedchiev S., Eftimova P., Smaoui H., Nguyen D.K., Toorman E., Bi O., (2013) OD 2.7 "Integrated report on design of innovative coastal structures and best practices for coastal defence. Results from numerical, experimental and prototype testing." http://www.theseusproject.eu/resources/documents/func-startdown/438/

13.2.2. INTERNAL DELIVERABLE

Part A: Burcharth H.F., Zanuttigh B.; Part B: Lykke Andersen T., Nørgaard J.H., Ruol P., Martinelli L., Zanuttigh B., Angelelli E., Castagnetti M., Mendoza-Baldwin E., Silva-Casarín R., Enriquez-Ortiz C.; Part C-E: Ruol P., Martinelli L., Zanuttigh B., Koftis T., Prinos P., Galiatsatou P., Mendoza-Baldwin E., Silva-Casarín R., Enriquez-Ortiz C., Chávez-Cárdenas X., Hoil-Baeza J., Bustos-Lira A., Pinedo-González J., Kuznetsov S., SaprykinaY., Lara J. L., Part F: Nørgaard J.H., Lykke Andersen T., Burcharth H. F.; Steendam J.G.; Part G: Ruol P., Martinelli L, Pezzutto P., Zanuttigh B., Kuznetsov S., Saprykina Y., Koftis T., Prinos P., Part H: Nørgaard J.H., Lykke Andersen T., Burcharth H. F., Sergent P., Prevot G. (2011) Internal Deliverable 2.2 "Report on physical tests on innovative coastal structures, preliminary version" THESEUS Project, Available on request

Part A: Burcharth H.F., Zanuttigh B.; Part B: Lykke Andersen T., Nørgaard J.H., Ruol P., Martinelli L., Zanuttigh B., Angelelli E., Mendoza-Baldwin E., Silva-Casarín R., Enriquez-Ortiz C.; Part C: Ruol P., Martinelli L., Zanuttigh B., Koftis T., Prinos P., Galiatsatou P., Mendoza-Baldwin E., Silva-Casarín R., Enriquez-Ortiz C., Chávez-Cárdenas X., Hoil-Baeza J., Bustos-Lira A., Pinedo-González J., Kuznetsov S., Saprykina Y., Lara J.L.; Part D: Nørgaard J.H., Lykke Andersen T., Hans Burcharth H.F., Steendam G.J; Part E: Ruol P., Martinelli L, Pezzutto P., Zanuttigh B., Kuznetsov S., Saprykina Y., Koftis T., Prinos P.;

Part F: Nørgaard J.H., Lykke Andersen T., Hans Burcharth H.F., Sergent P., Prevot G. (2012) Internal Deliverable 2.5 “Report on physical tests on innovative coastal structures, final version” THESEUS Project, Available on request

Zanuttigh B., Angelelli E., Koca K., Kortenhaus A., Kirca O., Bas B., Elginöz N., Bagci T., (2013) Internal Deliverable 3.3 “Wave energy converters” MERMAID Project, Available on request

13.3. CONFERENCES

Angelelli E., Zanuttigh B., Kofoed J.P. & K. Glejbøl “Experiments on the WavePiston, Wave Energy Converter” (2011) Proceeding of the European Wave and Tidal Energy Conference http://vbn.aau.dk/files/55763102/Experiments_on_the_WavePiston_Wave_Energy_Converter.pdf

Zanuttigh B., Angelelli E., Castagnetti M., Kofoed J.P. & Clausen L. “The wave field around DEXA devices and implications for coastal protection” (2011) Proceeding of the European Wave and Tidal Energy Conference

Angelelli E. & Zanuttigh B. “A farm of Wave Activated Bodies for coastal protection purposes” (2012) Proceeding of the International Conference on Coastal Engineering in Coastal Engineering Journal http://journals.tdl.org/icce/index.php/icce/article/view/6895/pdf
ISBN code: 9780989661119
ISSN code: 2156-1028

Angelelli E., Zanuttigh B. & Kofoed J.P. “Numerical modelling of the hydrodynamics around the farm of Wave Activated Bodies (WAB)” (2012) Proceeding of the International Conference on Ocean Energy

Angelelli E. & Zanuttigh B. “Protezione della costa mediante parchi di convertitori di energia da onda di tipo Wave Activated Bobies” (2012) Proceeding of the “Convegno Nazionale di Idraulica e Costruzioni Idrauliche”
ISBN code: 9788897181187

Angelelli E. & Zanuttigh B. “Wave disturbance induced by a one-line array of floating Wave Energy Converters” (2013) Proceeding of the European Wave and Tidal Energy Conference

Angelelli E., Zanuttigh B., Ferri F. & Kofoed J.P. “Experimental assessment of the mooring influence on the power output of floating Wave Activated Body WECs” (2013) Proceeding of the European Wave and Tidal Energy Conference

Koca K., Kortenhaus A., Oumeraci H., Zanuttigh B., Angelelli E., Cantu M., Suffredini R. & Franceschi G. “Recent Advances in the Development of Wave Energy Converters” (2013) Proceeding of the European Wave and Tidal Energy Conference

Troch P., Stratigaki V., Stallard T., Forehand D., Folley M., Kofoed J.P., Benoit M., Babarit A., Gallach Sánchez D., De Bosscher L., Rauwoens P., Elsässer B., Lamont-Kane P., McCallum P., McNatt C., Angelelli E., Percher A., Carpentero Moreno E., Bellew S., Dombre E., Charrayre F., Vantorre M., Kirkegaard J. & Carstensen S. “Physical Modelling of an Array of 25 Heaving Wave Energy Converters to Quantify Variation of Response and Wave Conditions” (2013) Proceeding of the European Wave and Tidal Energy Conference

Angelelli E., Zanuttigh B., Martinelli L. & Ferri F. “Physical and numerical modelling of mooring forces and displacements of a Wave Activated Body Energy Converter” (2014) To be presented at the International Conference on Ocean, Offshore and Arctic Engineering

13.4. BOOK

Burcharth H.F., Zanuttigh B., Lykke Andersen T., Lara J.L., Steendam G.J., Ruol P., Sergent P., Ostrowski R., Silva R., Martinelli L., Nørgaard J.H., Mendoza E., Simmonds D., Ohle N., Kappenberg J., Pan S., Nguyen D.K., Toorman E.A., Prinos P., Hoggart S., Chen Z., Piotrowska D., Pruszak Z., Schönhofer J., Skaja M., Szmytkiewicz P., Szmytkiewicz M., Leont’yev I., Angelelli E., Raosa A.N., Formentin S.M., Smaoui H., Bi Q., Sothmann J., Schuster D., Li M., Ge J., Lendzion J., Koftis T., Kuznetsov S., Puente A., Echavarri B., Medina R., Díaz-Simal P., Losada I.J., Maza M., Higuera P. “Coastal risk management in a changing climate” Elsevier (to be published)

14. ACKNOWLEDGMENT

At the beginning of my Ph.D. period, I was not sure to be able to reach this final target, i.e. the Ph.D. dissertation. Now it seems I could get this goal, and this is not only due to my determination, therefore I think it is appropriate to thank those who deserve it.

First of all, an acknowledgment goes to my parents and all my family, who supported me during my successes and in the hardest moments too. They have incited me into being focused on my goal and they gave me the strength to continue, showing me their pride for my achievements every day on.

Another fundamental acknowledgment is for my boyfriend, Tony Justin, who tried always to let me look at the bright side of the difficult situations, despite his working problems and "forced" distance periods. Thanks for the patience he showed me every day and for the many gestures of affection, e.g. listening to my presentations in the days before big events, put up with my panic and/or nervous fits, etc. I’ve always known I could rely on him, he is always ready to support and encourage me.

From the personal point of view, another thanks goes to various friends, who over the years reinforced our trust and relationship, despite being dropped in number!

Thanks also goes to my supervisors, who believed in me from the beginning, and that – although in varying quantities– have allowed me to live particular work experiences, such as participation in various international Conferences and in many European Projects working meetings.

Finally the author gratefully acknowledged the financial support of the European Commission through:

- FP7 ENV2009-1,Contract 244104 THESEUS project (“Innovative technologies for safer European coasts in a changing climate”), www.theseusproject.eu;
- FP7 OCEAN2011-1, Contract 288710 - MERMAID project (“Innovative Multi-purpose offshore platforms: planning, design and operation”), www.mermaidproject.eu;
- MARINET, a research infrastructure initiative under the 7th Framework Programme (FP7), which funded a part of the experimental activity described here;

and of the Danish Council for Strategic Research through SDWED project (Structural Design of Wave Energy Devices), www.sdwed.civil.aau.dk.

A last, but not least acknowledgment is for the reader of this thesis that, despite the various grammatical errors, was able to follow the logical thread and has enjoyed the content and results.

15. RINGRAZIAMENTI

All’inizio del periodo di Dottorato non ero affatto sicura di riuscire ad arrivare al traguardo finale di questa discussione, invece ora sembra il contrario, e ciò non è dovuto solo alla mia determinazione e quindi penso sia appropriato ringraziare chi di dovere.

Un primo ringraziamento è per i miei genitori e tutta la mia famiglia, che mi ha supportato sia durante i miei successi sia nei momenti più duri. Loro mi hanno spronata nell’essere concentrata nel mio obiettivo e mi hanno dato la forza di continuare, mostrandomi ogni giorno il loro orgoglio per i miei traguardi.

Un altro ringraziamento fondamentale va al mio ragazzo, Tony Justin, che ha cercato di farmi vedere sempre il bicchiere mezzo pieno, nonostante i suoi problemi lavorativi e i periodi di distanza “forzata”. Un grazie per la pazienza che ogni giorno mi ha mostrato e per i tanti gesti di affetto: dall’ascoltare le mie presentazioni i giorni precedenti a grandi eventi, al sopportarsi le mie scenate di panico e/o nervoso, etc. Ho sempre saputo di poter contare su di lui, che è sempre pronto a sostenermi ed incoraggiarmi.

Dal mio personale punto di vista, un altro ringraziamento va alle varie amicizie, che negli anni si sono rinforzate, nonostante siano calate in numero!

Un ringraziamento va anche ai miei relatori, che hanno creduto in me sin dall’inizio, e che seppur in quantità diversa, mi hanno permesso di vivere particolari esperienze lavorative, come la partecipazione a diverse Conferenze internazionali e a molti meeting di progetti Europei.

Infine, la dottoranda ringrazia il sostegno finanziario della Commissione Europea attraverso:

- FP7 ENV2009-1, Contratto 244.104 Progetto THESEUS ("Tecnologie innovative per sicure le coste europee in un clima che cambia"), www.theseusproject.eu;
- FP7 OCEAN2011-1, Contratto 288.710 - Progetto MERMAID ("Innovative piattaforme multi-uso in ambiente offshore: pianificazione, progettazione e funzionamento"), www.mermaidproject.eu;
- MARINET, un'iniziativa di infrastrutture di ricerca nell'ambito del 7° programma quadro (7° PQ), che ha finanziato una parte delle attività sperimentali descritte in questa tesi;

e del Consiglio danese per la ricerca strategica attraverso il progetto SDWED (Progettazione strutturale dei Convertitori di energia ondosa), www.sdwed.civil.aau.dk.

Un ultimo, ma non per questo meno importante, ringraziamento va al lettore di questa tesi che, nonostante i vari errori grammaticali, è riuscito a seguirne il filo logico ed ha apprezzato i contenuti e i risultati ottenuti.